Julius-Maximilians-Universität Würzburg
Graduate School of Science and Technology
Sektion Molecular & Material Sciences

Dissertation zur Erlangung des naturwissenschaftlichen Doktorgrades
der Graduate School of Science and Technology,
Julius-Maximilians-Universität Würzburg

Coherent Multidimensional Spectroscopy in Molecular Beams and Liquids Using Incoherent Observables

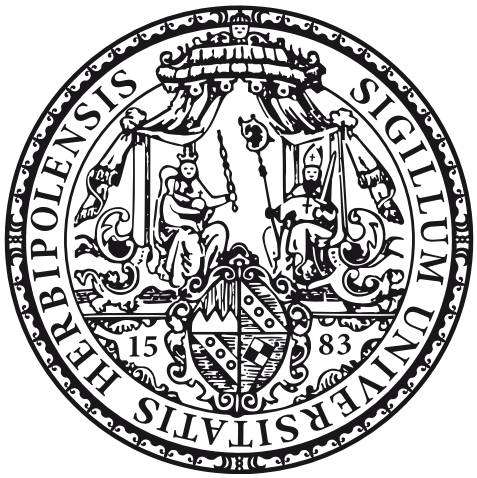

Kohärente Multidimensionale Spektroskopie in Molekularstrahlen und Flüssigkeiten durch inkohärente Observablen

vorgelegt von
Sebastian Röding

aus
Würzburg

Würzburg, 2017

CC BY NC ND

Eingereicht am: .....
Stempel des GSST Büros

Mitglieder des Promotionskomitees:

Vorsitzende/r: .....

1. Betreuer: Prof. Dr. Tobias Brixner

2. Betreuer: Prof. Dr. Ingo Fischer

3. Betreuer: Prof. Dr. Jens Pflaum

Tag des Promotionskolloquiums: .....

Doktorurkunden ausgehändigt am: .....

Kurzfassung

Das Ziel der vorliegenden Arbeit war die Umsetzung einer experimentellen Herangehensweise, welche die kohärente zweidimensionale (2D) Spektroskopie an Proben in unterschiedlichen Aggregatzuständen ermöglicht. Hierzu wurde zunächst ein Aufbau für flüssige Proben realisiert, in welchem die emittierte Fluoreszenz als Messsignal zur Aufnahme der 2D Spektren genutzt wird. Im Gegensatz zu dieser bereits etablierten Methode in der flüssigen Phase stellt die in dieser Arbeit außerdem vorgestellte 2D Spektroskopie an gasförmigen Proben in einem Molekularstrahl einen neuen Ansatz dar. Hierbei werden zum ersten Mal Kationen mittels eines Flugzeitmassenspektrometers als Signal verwendet und somit ionen-spezifische 2D Spektren isolierter Moleküle erhalten. Zusätzlich zu den experimentellen Entwicklungen wurde in dieser Arbeit ein neues Konzept zur Datenerfassung in der 2D Spektroskopie entworfen, welches mit Hilfe einer optimierten Signalabtastung und eines Compressed-Sensing Rekonstruktionsalgorithmus die Aufnahmezeit der Daten deutlich reduziert.

Charakteristisch für die in dieser Arbeit eingesetzte Variante der 2D Spektroskopie ist die Verwendung einer phasenkohärenten Sequenz bestehend aus vier Laserimpulsen in einer kollinearen Laserstrahlgeometrie zur Anregung der Probe. Diese Impulssequenz wurde durch einen Laserimpulsformer erzeugt, der durch Änderung der relevanten Laserimpulsparameter mit der Wiederholrate des Lasers eine schnelle Datenerfassung ermöglicht. Die Antwort der Probe auf diese Anregung wurde durch inkohärente Observablen gemessen, welche proportional zur Population des angeregten Zustandes sind, wie zum Beispiel Fluoreszenz oder Ionen. Um aus diesem Signal während der Datenanalyse die gewünschten nichtlinearen Beiträge zu extrahieren, wurde die Messung mit verschiedenen Kombinationen der relativen Phase zwischen den Laserimpulsen wiederholt ("Phase Cycling").

Der Aufbau zur 2D Spektroskopie in flüssiger Phase mit Fluoreszenz-Detektion wurde an Hand von 2D Spektren des Laserfarbstoffes Cresyl Violett charakteri-

siert. Hierbei wurden Oszillationen in verschiedenen Bereichen des 2D Spektrums beobachtet, welche durch vibronische Kohärenzen hervorgerufen werden und mit früheren Beobachtungen in der Literatur übereinstimmen.

Mit dem gleichen Datensatz wurde im nächsten Schritt das neue Konzept zur optimierten Datenerfassung demonstriert. Um ein optimiertes Schema für die Signalabtastung zu finden, wurde ein genetischer Algorithmus implementiert, wobei nur ein Viertel der eigentlichen Datenpunkte zur Messwerterfassung verwendet werden sollte. Dies reduziert die Zeitdauer der Datenerfassung auf ein Viertel der ursprünglichen Messzeit. Die Rekonstruktion des vollständigen Signales erfolgte mit Hilfe einer neuartigen, kompakten Darstellung von 2D Spektren basierend auf der von Neumann Basis. Diese Herangehensweise benötigte im Vergleich zur üblicherweise verwendeten Fourier Basis nur ein Sechstel der Koeffizienten um das Signal vollständig darzustellen und ermöglichte so die erfolgreiche Rekonstruktion der Oszillationen in Cresyl Violett aus einem reduzierten Datensatz.

Mit Hilfe der neuartigen kohärenten 2D Spektroskopie an Molekularstrahlen wurden Übergänge von hoch angeregten Rydberg-Zuständen ins ionische Kontinuum in Stickstoffdioxid untersucht. Als dominierender Beitrag stellte sich hierbei der Übergang in auto-ionisierende Zustände heraus. Ein wesentlicher Vorteil der Datenerfassung über ein Flugzeitmassenspektrometer ist die Möglichkeit der gleichzeitigen Aufnahme von 2D Spektren der Edukte und Produkte einer chemischen Reaktion. Dies wurde in Experimenten zur Mehrphotonenionisation gezeigt, in denen deutliche Unterschiede in den 2D Spektren des Stickstoffdioxid-Kations und des Stickstoffmonoxid-Fragmentes sichtbar wurden, welche auf unterschiedliche Antwortfunktionen zurückzuführen sind.

Die in dieser Arbeit entwickelten experimentellen Techniken ermöglichen die schnelle Aufnahme von 2D Spektren für Proben in unterschiedlichen Aggregatzuständen und erlauben einen zuverlässigen, direkten Vergleich der Ergebnisse. Sie sind deshalb ein Wegbereiter für zukünftige Untersuchungen der Eigenschaften quantenmechanischer Kohärenzen in photophysikalischen Prozessen oder während photochemischer Reaktionen in unterschiedlichen Aggregatzuständen.

Abstract

The aim of the present work was to implement an experimental approach that enables coherent two-dimensional (2D) electronic spectroscopy of samples in various states of matter. For samples in the liquid phase, a setup was realized that utilizes the sample fluorescence for the acquisition of 2D spectra. Whereas the liquid-phase approach has been established before, coherent 2D spectroscopy on gaseous samples in a molecular beam as developed in this work is in fact a new method. It employs for the first time cations in a time-of-flight mass spectrometer for signal detection and was used to obtain the first ion-selective 2D spectra of a molecular-beam sample. Additionally, a new acquisition concept was developed in this thesis that significantly decreases measurement times in 2D spectroscopy using optimized sparse sampling and a compressed-sensing reconstruction algorithm.

Characteristic for the variant of 2D spectroscopy presented in this work is the usage of a phase-coherent sequence of four laser pulses in a fully collinear geometry for sample excitation. The pulse sequence was generated by a custom-designed pulse shaper that is capable of rapid scanning by changing the pulse parameters such as time delays and phases with the repetition rate of the laser. The sample's response was detected by monitoring incoherent observables that arise from the final-state population, for instance fluorescence or cations. Phase cycling, i.e., signal acquisition with different combinations of the relative phases of the excitation pulses, was applied to extract nonlinear signal contributions from the full signal during data analysis.

Liquid-phase 2D fluorescence spectroscopy was established with the laser dye cresyl violet as a sample molecule, confirming coherent oscillations previously observed in literature that are originating from vibronic coherences in specific regions of the 2D spectrum.

The data set of this experiment was used subsequently to introduce optimized sparse sampling in 2D spectroscopy. An optimization algorithm was implemented

in order to find the best sampling pattern while taking only one quarter of the regular time-domain sampling points, thereby reducing the acquisition time by a factor of four. Signal recovery was based on a new and compact representation of 2D spectra using the von Neumann basis, which required about six times less coefficients than the Fourier basis to retain the relevant information. Successful reconstruction was shown by recovering the coherent oscillations in cresyl violet from a reduced data set.

Finally, molecular-beam coherent 2D spectroscopy was introduced with an investigation of ionization pathways in highly-excited nitrogen dioxide, revealing transitions to discrete auto-ionizing states as the dominant contribution to the ion signal. Furthermore, the advantage of the time-of-flight approach to obtain reactant and product 2D spectra simultaneously enabled the observation of distinct differences in the multiphoton-ionization response functions of the nitrogen dioxide cation and the nitrogen oxide ionic fragment.

The developed experimental techniques of this work will facilitate fast acquisition of 2D spectra for samples in various states of matter and permit reliable direct comparison of results. Therefore, they pave the way to study the properties of quantum coherences during photophysical processes or photochemical reactions in different environments.

Contents

List of Publications

Parts of this thesis have been published in the following references:

Reference [1]:

S. Draeger, S. Roeding, and T. Brixner,
Rapid-scan coherent 2D fluorescence spectroscopy,
Opt. Express **25**(4),3259–3267 (2017).

Reference [2]:

S. Roeding, N. Klimovich, and T. Brixner,
Optimizing sparse sampling for 2D electronic spectroscopy,
J. Chem. Phys. **146**, 084201 (2017).

Reference [3]:

S. Roeding and T. Brixner,
Multidimensional electronic spectroscopy in molecular beams with mass-resolved ion detection,
In *International Conference on Ultrafast Phenomena, OSA* Technical Digest (online) Optical Society of America, 2015, paper UM3A.2.

Reference [4]:

S. Roeding and T. Brixner,
Molecular-beam coherent 2D electronic spectroscopy reveals photoionization pathways,
submitted for publication (2017).

The publications listed above have partly been used in this dissertation. The following table itemizes where and to what extent the different sections of the publications have been reused. The sources of reproduced figures are additionally indicated at the end of the corresponding figure captions.

Publication	Usage	Dissertation
Ref. [1]		
pp. 5–9	text adapted, modified and extended	pp. 48–49, pp. 55–59
pp. 9	text modified and extended	pp. 62
Ref. [2]		
pp. 1–2	text reproduced and extended, figure reproduced	pp. 63–65
pp. 3	text reproduced, modified and extended	pp. 69–72
pp. 4–6	text reproduced, modified and extended; figures reproduced	pp. 72–82
Ref. [4]		
(submitted)	text reproduced and extended	p. 85
	text reproduced and extended	pp. 87–89
	text and figures reproduced, minor modifications	pp.89–103

Further publications not related to this thesis:
Reference [5]:

A. Steinbacher, S. Roeding, T. Brixner, and P. Nuernberger,
Ultrafast photofragment ion spectroscopy of the Wolff rearrangement in 5-diazo Meldrum's acid,
Phys. Chem. Chem. Phys. **16**, 7290–7298 (2014).

Reference [6]:

A. Steinbacher, S. Roeding, T. Brixner, and P. Nuernberger,
The role of excess energy in the ultrafast Wolff rearrangement,
In *Ultrafast Phenomena XIX* (K. Yamanouchi, S. Cundiff, R. de Vivie-Riedle, M. Kuwata-Gonokami, and L. DiMauro, Eds.) Springer Proceedings in Physics **162**, 180–183 (2015).

1 | Introduction

In the course of evolution, life on Earth has adopted optimally to its environment. For instance, some microorganisms are able to withstand environmental extremes regarding temperature, pressure, or radiation [7]. Photosynthetic organisms have developed successful strategies to efficiently harness the available sunlight in their natural habitat [8], but also human vision has adapted to the conditions on the Earth's surface and developed its greatest sensitivity in what is by definition the visible part of the solar spectrum that passes the Earth's atmosphere. Photosynthesis and vision are processes that are triggered by electronic transitions in pigments and proceed by subsequent photochemical reactions such as light-induced conformation changes and charge-transfer processes.

In a natural environment, the primary source of energy and therefore the main driver of those reactions is the Sun, which has naturally been of great interest not only to scientists in all ages. William Hyde Wollaston was the first to observe black absorption lines in the solar spectrum [9], which were later studied by Joseph von Fraunhofer utilizing his invention of the spectrograph [10]. This technical breakthrough and further innovations paved the way for the investigations of chemical elements, for example by Gustav Kirchhoff and Robert Bunsen [11]. In our days, turn-key absorption spectrometers have become part of the standard equipment for steady-state analytical purposes in laboratories around the world.

Methods that disturb the chemical equilibrium and monitor its relaxation were pioneered by Eigen [12], and Norrish and Porter [13] and revealed for the first time information about the ultrafast dynamics of chemical reactions. Subsequently, optical pump–probe techniques developed rapidly with the advent of the laser. Ever since, the aim of researchers was to observe even faster processes and to develop the corresponding techniques, peaking in the *femtosecond age* [14] coined by Ahmed Zewail and coworkers that finally allowed to investigate the fundamental photochemistry of light-harvesting [15, 16] and vision [17] with ultrashort laser pulses. Ongoing research has established pump–probe spectroscopy using X-ray

pulses to directly probe dynamic structural changes [18] and succeeded to push the boundaries to even shorter timescales, reaching attosecond time resolution [19].

Using femtosecond spectroscopy in the visible and near infrared spectral region, coherent phenomena such as coherent superpositions of vibrational wavefunctions (wave packets) could be detected [20–22]. Observations of coherent oscillations in photosynthetic light-harvesting raised questions about the role of coherence for the efficiency of energy and charge transfer in nature [23, 24], but also in artificial light-harvesters such as organic photovoltaics [25–27]. They can be addressed using coherent 2D spectroscopy, which unravels quantum-mechanical couplings and thereby energy transfer pathways by correlating excitation and emission frequencies. Technical advances have established the method in recent years as an extension to transient-absorption spectroscopy in many laboratories for the investigation of photo-induced dynamics in solid-state physics, surface science and (bio-)chemical research [28].

The aim of this thesis is to realize an experimental approach that enables coherent 2D electronic spectroscopy of samples in various states of matter. This grants maximum comparability within experiments using the same substance in different environments, and thereby renders it possible to study the influence of the surrounding bath on coherence properties such as dephasing times. The influence of the bath degrees of freedom can further be elucidated by removing solvent-solute interactions using an isolated sample in a molecular beam, which additionally facilitates comparison with theoretical calculations. The work presented in this thesis employs incoherent observables that arise from the final-state populations and introduces for the first time cations in combination with time-of-flight detection as a new observable in 2D spectroscopy. This paves the way to investigate the evolution of coherences during photochemical reactions, enabled by the simultaneous acquisition of 2D spectra of reactants and reaction products in the mass spectrum. Additionally, a setup is presented that permits to investigate liquid-phase samples via fluorescence detection.

The outline of this thesis is as follows. Basic theoretical and experimental concepts that are fundamental to coherent 2D spectroscopy are reviewed in Chap. 2 with the aim to classify the experimental approach of this work by comparing different acquisition strategies. Furthermore, it is described how nonlinear response functions can be separated via control over the spectral phase of the excitation laser pulses.

The experimental methods of this work are specified in more detail in Chap. 3, explaining the optical setups to generate and control femtosecond laser pulses. It has a particular emphasis on femtosecond pulse shaping and its application in

spectroscopy, as a custom-designed pulse shaper that allows rapid scanning by updating the output pulse shape with the repetition rate of the laser is the key element of the setup. Furthermore, the acquisition methods for 2D spectroscopy on liquid samples via fluorescence detection and for 2D spectroscopy on gaseous samples in molecular beams using cation detection are presented.

Subsequently, rapid-scan coherent 2D fluorescence spectroscopy is demonstrated in Chap. 4 with a study of the laser dye cresyl violet, monitoring coherent oscillations originating from vibronic coherences in localized regions of the 2D spectrum. Furthermore, the unusual fluorescence of azulene from the second excited state is employed to select specific pathways for detection. This is used in order to emphasize the special capability of the phase-cycling method to acquire and extract rephasing, nonrephasing and also double-quantum coherence contributions with the same measurement.

The need to improve acquisition speed is addressed in Chap. 5. A new acquisition concept is presented that decreases acquisition times in 2D spectroscopy using optimized sampling of a subset of the regular parameter space. Successful signal recovery with a compressed-sensing reconstruction algorithm is demonstrated with cresyl violet data obtained from the experiments presented in Chap. 4. Additionally, a new representation of 2D spectra based on the von Neumann basis is introduced that facilitates signal reconstruction and may further be exploited in future experiments to speed up acquisition.

Finally, in Chap. 6, molecular-beam coherent 2D electronic spectroscopy is established as a new method that employs cations for the acquisition of 2D spectra in isolated samples. The method is applied to investigate the ionization mechanism of NO_2 excited into high-lying Rydberg states. Furthermore, 2D spectra of multiphoton ionization are acquired that reveal distinct differences between the parent ion 2D spectrum and the fragment 2D spectrum.

The findings of this thesis are summarized in Chap. 7.

2 | Ultrafast Laser Spectroscopy

Methods of ultrafast laser spectroscopy are applied in many research areas to investigate dynamical processes with up to attosecond time resolution. In particular, coherent multidimensional spectroscopy has evolved into a highly appreciated technique for the investigation of (bio-) chemical kinetics and ultrafast processes in solid-state physics. This chapter summarizes the most important theoretical and experimental aspects of coherent multidimensional electronic spectroscopy and reviews the different experimental approaches to acquire the spectroscopic information. A detailed description of the fundamental concepts can be found in various textbooks [29–31] and review articles [28, 32–37] and references therein.

Section 2.1 generally treats important aspects of nonlinear spectroscopy from a theoretical perspective and introduces the response-function formalism. This is done by considering first basic principles of light-matter interaction and electronic transitions in molecules, intending to highlight fundamental approximations underlying the calculation of response functions. Afterwards, the nonlinear response of a quantum system to the excitation by ultrashort laser pulses is derived and macroscopic observables are calculated using time-dependent perturbation theory. Furthermore, properties of the most common signal contributions in multidimensional spectroscopy, the rephasing and nonrephasing signals, are discussed. Finally, a phenomenological approach to describe 2D lineshapes arising from system-bath interaction is outlined.

Section 2.2 deals with various experimental facets of coherent multidimensional spectroscopy. It is focused on experimental approaches to measure nonlinear response functions and highlights the information provided by resolving excitation and emission frequency into two-dimensional spectra. In particular, coherence-based and population-based methods are distinguished and compared with respect to signal acquisition strategies and possible observables, aiming to classify the developed techniques of this work into already existing approaches. As this work relies on population-based 2D spectroscopy with incoherent observables, the pos-

sibility to distinguish different nonlinear signals via *phase cycling* is emphasized and treated in detail.

2.1 Nonlinear Spectroscopy

In this section the perturbative approach to calculate nonlinear response functions is outlined, aiming to introduce the reader into the different types of nonlinear signals that can be acquired by the experimental setups developed in this work. In particular, the rephasing and nonrephasing signal contributions and their characteristics in the time domain and frequency domain are discussed.

2.1.1 Light-Matter Interaction

The interaction of an electromagnetic field with a quantum system is at the heart of every spectroscopy experiment. The external radiation acts as a perturbation to the system Hamiltonian $\hat{\mathcal{H}}_0$, generating new eigenstates that lead to level splittings, energy shifts, or transitions [38, 39]. In the semi-classical approximation, the radiation field is treated classically, whereas the time evolution of the sample is governed by quantum mechanics.

The following paragraph shortly reviews the derivation of the transition matrix element for a hydrogen-like quantum system in a weak monochromatic external field, aiming to illustrate the basic assumptions that are necessary to describe molecular transitions in the dipole approximation as typically done in literature on coherent multidimensional spectroscopy. A thorough treatment of light-matter interaction, also for an ensemble of charges, can be found in various textbooks [38–40].

The non-relativistic Hamilton operator $\hat{\mathcal{H}}$ for a spinless particle of charge q and mass m in a Coulomb potential $V_0(\hat{\mathbf{r}})$ can be written as [40]

$$\hat{\mathcal{H}} = \frac{1}{2m}\left[\hat{\mathbf{p}} - q\mathbf{A}(\hat{\mathbf{r}},t)\right]^2 + V_0(\hat{\mathbf{r}}) + q\Phi(\hat{\mathbf{r}},t)\,, \tag{2.1.1}$$

with the position operator $\hat{\mathbf{r}}$ and the momentum operator $\hat{\mathbf{p}} = -\mathrm{i}\hbar\nabla$ [39]. Here, bold letters stand for vector quantities. $\Phi(\hat{\mathbf{r}},t)$ denotes the scalar potential and $\mathbf{A}(\hat{\mathbf{r}},t)$ the vector potential of the electromagnetic field. The electric and magnetic fields are calculated from these potentials via [41]

$$\mathbf{E}(\hat{\mathbf{r}},t) = -\nabla\Phi(\hat{\mathbf{r}},t) - \frac{\partial}{\partial t}\mathbf{A}(\hat{\mathbf{r}},t)\,; \qquad \mathbf{B}(\hat{\mathbf{r}},t) = \nabla\times\mathbf{A}(\hat{\mathbf{r}},t)\,. \tag{2.1.2}$$

Assuming a transverse radiation field (Coulomb gauge, $\nabla\mathbf{A}(\hat{\mathbf{r}},t)=0$) and charge-free space ($\Phi(\hat{\mathbf{r}},t)=0$), the Hamiltonian $\hat{\mathcal{H}}$ of Eq. (2.1.1) simplifies to a stationary system Hamiltonian $\hat{\mathcal{H}}_0$ and a time-dependent interaction Hamiltonian $\hat{\mathcal{V}}(t)$ [40]

$$\hat{\mathcal{H}}_0 = \frac{1}{2m}\hat{\mathbf{p}}^2 + V_0(\hat{\mathbf{r}})\,, \qquad \hat{\mathcal{V}}(t) = \frac{q}{m}\mathbf{A}(\hat{\mathbf{r}},t)\hat{\mathbf{p}}\,. \tag{2.1.3}$$

Terms with $\mathbf{A}^2$ are neglected in Eq. (2.1.3) as the vector potential is assumed to be weak compared to the internal binding potentials. The interaction Hamiltonian $\hat{\mathcal{V}}(t)$ couples, e.g., the ground state $|g\rangle$ and the excited state $|e\rangle$ of the quantum system. In time-dependent first-order perturbation theory the transition rate $w_{e\leftarrow g}$ between the two states is generally proportional to the transition matrix element $\langle e|\,\hat{\mathcal{V}}(t)\,|g\rangle$ and the density of final states $\rho(E_e)$,

$$w_{e\leftarrow g} = \frac{2\pi}{\hbar}|\langle e|\,\hat{\mathcal{V}}(t)\,|g\rangle|^2\,\rho(E_e)\,, \tag{2.1.4}$$

which is known as *Fermi's golden rule* [39].

For a monochromatic electromagnetic field with the polarization state given by $\boldsymbol{\epsilon}$ and oscillating at the frequency ω_0, the vector potential $\mathbf{A}(\hat{\mathbf{r}},t)$ can be expressed as a plane wave of amplitude A_0

$$\mathbf{A}(\hat{\mathbf{r}},t) = A_0\boldsymbol{\epsilon}\left(\mathrm{e}^{\mathrm{i}\mathbf{k}\hat{\mathbf{r}}-\mathrm{i}\omega_0 t} + \mathrm{e}^{-\mathrm{i}\mathbf{k}\hat{\mathbf{r}}+\mathrm{i}\omega_0 t}\right)\,. \tag{2.1.5}$$

Thus, the two terms of the transition matrix element $\langle e|\,\hat{\mathcal{V}}(t)\,|g\rangle$ of Eq. (2.1.3) become

$$\langle e|\,\hat{\mathcal{V}}(t)\,|g\rangle = A_0\frac{q}{m}\boldsymbol{\epsilon}\,\langle e|\,\mathrm{e}^{\mp\mathrm{i}\omega_0 t\pm\mathrm{i}\mathbf{k}\hat{\mathbf{r}}}\hat{\mathbf{p}}\,|g\rangle\,, \tag{2.1.6}$$

distinguishing absorption and emission processes by opposite signs [38–40].

For radiation wavelengths much larger than the spatial dimensions of the quantum system ($\mathbf{k}\hat{\mathbf{r}} \ll 1$), the Taylor series $\mathrm{e}^{\pm\mathrm{i}\mathbf{k}\hat{\mathbf{r}}} = 1\pm\mathrm{i}\mathbf{k}\hat{\mathbf{r}}\pm\frac{1}{2!}(\mathrm{i}\mathbf{k}\hat{\mathbf{r}})^2\pm\ldots$ can be approximated with unity. Furthermore, the Heisenberg equation of motion $\hat{\mathbf{p}} = \frac{\mathrm{i}m}{\hbar}\left[\hat{\mathcal{H}}_0,\hat{\mathbf{r}}\right]$ can be employed. This leads to

$$\langle e|\,\hat{\mathcal{V}}(t))\,|g\rangle = \mathrm{i}A_0\omega_{eg}\mathrm{e}^{\mp\mathrm{i}\omega_0 t}\boldsymbol{\epsilon}\,\langle e|\,\hat{\boldsymbol{\mu}}\,|g\rangle\,, \tag{2.1.7}$$

with the transition frequency ω_{eg}, the dipole operator $\hat{\boldsymbol{\mu}} = q\hat{\mathbf{r}}$ and the dipole matrix element $\langle e|\,\hat{\boldsymbol{\mu}}\,|g\rangle$ [40]. The transition matrix element can finally be expressed as a

function of the electric field with the help of Eqs. (2.1.2) and (2.1.5),

$$\langle e|\,\hat{\mathcal{V}}(t)\,|g\rangle = \frac{\omega_{eg}}{\omega_0}\,\langle e|\,-\boldsymbol{E}(t)\cdot\hat{\boldsymbol{\mu}}\,|g\rangle\ . \tag{2.1.8}$$

Assuming resonant excitation $\omega_0 = \omega_{eg}$ in the following, the interaction Hamiltonian in the *electric dipole approximation* of the transition matrix element is $\hat{\mathcal{V}}(t) = -\hat{\boldsymbol{\mu}}\cdot\boldsymbol{E}(t)$. It is justified for experiments using small molecules composed of a few atoms and laser pulses in the visible spectral region, as done in this work.

As the operator $\hat{\boldsymbol{\mu}}$ is odd under spatial inversion, the states $|g\rangle$ and $|e\rangle$ need to have different parity for a non-zero transition rate. Further symmetry considerations in the evaluation of the transition dipole matrix lead to the well-known dipole selection rules for electromagnetic transitions [38]. In the case of molecules, the structure of spectral absorption bands emerges from Eq. (2.1.8) and can be estimated from the wavefunctions of the states $|g\rangle$ and $|e\rangle$ involved in the transition via the Born-Oppenheimer approximation and the Franck-Condon principle [40, 42, 43].

It is worth to stress the vectorial character of the product $-\hat{\boldsymbol{\mu}}\cdot\boldsymbol{E}(t)$. In order to obtain a non-zero transition probability, the polarization of the incident electromagnetic field needs to have a component in the direction of the transition dipole moment. That can be exploited experimentally in interesting applications, e.g., for the selective excitation of states with a given symmetry in pre-aligned molecules [44, 45] or for control of the ion yield in multiphoton ionization by using optimally polarization-shaped laser pulses [46].

2.1.2 The Response-Function Formalism

As shown in the previous section, the electromagnetic field couples two quantum-mechanical states via the transition-matrix element $\mathcal{V}_{eg}(t) = \langle e|\,\hat{\mathcal{V}}(t)\,|g\rangle$ that leads to linear absorption or emission processes in first-order perturbation theory. In this section, the weak time-dependent perturbation is expanded into higher orders using the *Dyson series*, aiming to calculate macroscopic observables of the *nonlinear* response to an external electromagnetic field, such as the sample polarization or the excited-state population. Since experiments are performed on a statistical mixture of quantum systems, this expansion is treated in terms of the *density matrix* $\rho(t)$ [39],

$$\rho(t) = \sum_k p_k\,|\Psi_k(t)\rangle\,\langle\Psi_k(t)|\,, \tag{2.1.9}$$

where p_k denotes the statistical probability of finding the system in a state $|\Psi_k(t)\rangle$, and therefore $\sum_k p_k = 1$. Diagonal elements of the density matrix are known as *populations*, whereas off-diagonal elements are *coherences* [31, 35].

The time evolution of the density matrix is governed by the time-dependent Hamiltonian $\hat{\mathcal{H}}(t) = \hat{\mathcal{H}}_0 + \hat{\mathcal{V}}(t)$ and described by the density matrix' time derivative in the *Liouville-von Neumann equation*

$$\dot{\rho}(t) = -\frac{\mathrm{i}}{\hbar}[\hat{\mathcal{H}}(t), \rho(t)] = -\frac{\mathrm{i}}{\hbar}[\hat{\mathcal{H}}_0, \rho(t)] - \frac{\mathrm{i}}{\hbar}[\hat{\mathcal{V}}(t), \rho(t)]\,. \tag{2.1.10}$$

Perturbative Expansion of the Density Matrix

In order to calculate the nonlinear response to the time-dependent perturbation $\hat{\mathcal{V}}(t)$, the density matrix is expanded in a power series

$$\rho(t) \equiv \rho^{(0)}(t) + \sum_{n=1}^{\infty} \rho^{(n)}(t)\,, \tag{2.1.11}$$

with $\rho^{(0)}(t)$ being the time-evolution of the density matrix subject to the stationary system Hamiltonian $\hat{\mathcal{H}}_0$ and $\rho^{(n)}(t)$ the n-th order perturbation term

$$\begin{aligned}\rho^{(n)}(t) = \left(\frac{\mathrm{i}}{\hbar}\right)^n \int_{t_0}^{t} \mathrm{d}t_n \int_{t_0}^{t_n} \mathrm{d}t_{n-1} \ldots \int_{t_0}^{t_2} \mathrm{d}t_1 \\ \times\, \mathrm{e}^{-\frac{\mathrm{i}}{\hbar}\hat{\mathcal{H}}_0(t-t_0)}[\hat{\mathcal{V}}_I(t_n), [\hat{\mathcal{V}}_I(t_{n-1}), \ldots, [\hat{\mathcal{V}}_I(t_1), \rho(t_0)]\ldots]]\mathrm{e}^{+\frac{\mathrm{i}}{\hbar}\hat{\mathcal{H}}_0(t-t_0)}\,,\end{aligned} \tag{2.1.12}$$

where $t_n, t_{n-1}, \ldots, t_1$ represent the times of interaction with $\hat{\mathcal{V}}_I(t)$. The density matrix in Eq. (2.1.12) is written in the Schrödinger picture, whereas the operators are represented in the interaction picture indicated by the subscript "I" and calculated from the Schrödinger representation $\hat{\mathcal{V}}(t)$ via [39]

$$\hat{\mathcal{V}}_I(t) = \mathrm{e}^{+\frac{\mathrm{i}}{\hbar}\hat{\mathcal{H}}_0(t-t_0)}\hat{\mathcal{V}}(t)\mathrm{e}^{-\frac{\mathrm{i}}{\hbar}\hat{\mathcal{H}}_0(t-t_0)}\,. \tag{2.1.13}$$

Third-Order Polarization

A macroscopic observable of the n-th order perturbation term $\rho^{(n)}(t)$ is the nonlinear polarization $\mathrm{P}^{(n)}(t)$, given by the expectation value of the dipole operator $\hat{\mu}$ and thus originating after the last perturbation from the off-diagonal elements $\rho_{kl}^{(n)}(t)$, $k \neq l$ (coherences) of the density matrix in the eigenbasis of $\hat{\mathcal{H}}_0$,

$$\mathrm{P}^{(n)}(t) = \mathbf{Tr}(\hat{\mu}\rho^{(n)}(t)) \equiv \langle \hat{\mu}\rho^{(n)}(t)\rangle\,. \tag{2.1.14}$$

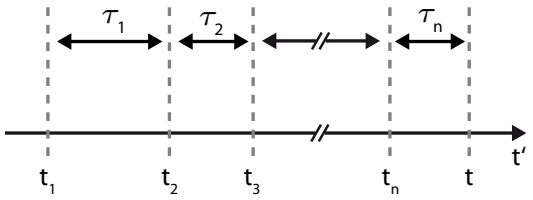

Figure 2.1: Definition of time variables. Absolute interaction times of the dipole operator $\hat{\mu}_I$ with the density matrix ρ are denoted with Latin characters t_n. Greek characters τ_n are used for the time intervals between the interactions.

Here, $\mathbf{Tr}(\cdot)$ indicates the trace of a square matrix. Using Eq. (2.1.12) and $\hat{\mathcal{V}}_I(t_n) = -E(t_n)\hat{\mu}_I(t_n)$, where vector notation has been omitted for simplicity, the n-th order polarization can be expressed as

$$\mathrm{P}^{(n)}(t) = \left(\frac{\mathrm{i}}{\hbar}\right)^n \int_{-\infty}^{t} \mathrm{d}t_n \int_{-\infty}^{t_n} \mathrm{d}t_{n-1} ... \int_{-\infty}^{t_2} \mathrm{d}t_1 E(t_n)E(t_{n-1})...E(t_1) \times \langle \mu_I(t)[\mu_I(t_n), [\mu_I(t_{n-1}), ..., [\mu_I(t_1), \rho(-\infty)]...]]\rangle \,. \tag{2.1.15}$$

The time-evolution operators in Eq. (2.1.12) can be neglected here by making use of the invariance of the trace under cyclic permutation. Additionally, under the assumption that the system is in thermal equilibrium before the first interaction, t_0 is set to $-\infty$. Redefining positive time intervals $\tau_n \equiv t - t_n$, $\tau_{n-1} \equiv t_n - t_{n-1}$, etc., instead of absolute interaction times t_n (Fig. 2.1) and setting $t_1 = 0$, Eq. (2.1.15) can be generally written as a convolution of the incident field with the nonlinear response function $S^{(n)}(\tau_n, \tau_{n-1}, ..., \tau_1)$,

$$\mathrm{P}^{(n)}(t) = \int_0^{\infty} \mathrm{d}\tau_n \int_0^{\infty} \mathrm{d}\tau_{n-1} ... \int_0^{\infty} \mathrm{d}\tau_1 \, S^{(n)}(\tau_n, \tau_{n-1}, ..., \tau_1) \times E(t-\tau_n)E(t-\tau_n-\tau_{n-1})...E(t-\tau_n-...-\tau_1) \,, \tag{2.1.16}$$

where the response $S^{(n)}(\tau_n, \tau_{n-1}, ..., \tau_1)$ is given by

$$S^{(n)}(\tau_n, \tau_{n-1}, ..., \tau_1) = \left(\frac{\mathrm{i}}{\hbar}\right)^n \langle \hat{\mu}_I(\tau_n + \tau_{n-1} + ... + \tau_1) \times [\hat{\mu}_I(\tau_{n-1} + ... + \tau_1), ..., [\hat{\mu}_I(\tau_1), [\hat{\mu}_I(0), \rho(-\infty)]]...]\rangle \,. \tag{2.1.17}$$

Coherence-based 2D spectroscopy techniques employ coherently emitted electric fields $E_{\mathrm{sig}}(t)$ for detection that are originating from the third-order polarization

via $E_{\mathrm{sig}}(t) \propto \mathrm{i}P^{(3)}(t)$, with

$$\mathrm{P}^{(3)}(t) = \int_0^\infty \mathrm{d}\tau_3 \int_0^\infty \mathrm{d}\tau_2 \int_0^\infty \mathrm{d}\tau_1 \, S^{(3)}(\tau_3, \tau_2, \tau_1) \times E(t-\tau_3)E(t-\tau_3-\tau_2)E(t-\tau_3-\tau_2-\tau_1)\,, \tag{2.1.18}$$

and

$$S^{(3)}(\tau_3, \tau_2, \tau_1) = \left(\frac{\mathrm{i}}{\hbar}\right)^3 \langle \hat{\mu}_I(\tau_3+\tau_2+\tau_1)[\hat{\mu}_I(\tau_2+\tau_1), [\hat{\mu}_I(\tau_1), [\hat{\mu}_I(0), \rho(-\infty)]]]\rangle\,. \tag{2.1.19}$$

Fourth-Order Population

The experimental techniques of this work rely on the detection of incoherent fourth-order signals that originate from the final diagonal elements $\rho^{(4)}_{kk}$ (populations) of the density matrix after four perturbations. The population is measured indirectly by observing the effect of the excitation on the sample and not by acquiring the amount of absorbed or transmitted light. Hence, the population-based approaches belong to the class of *action-spectroscopy* techniques. Various indicators for the fourth-order population can be used, such as the sample fluorescence, emitted photoelectrons, or cations. In analogy to Eq. (2.1.14), the fourth-order signal yield $\mathrm{Y}^{(4)}(t)$ can be calculated as the expectation value of a projection operator $\hat{\Pi} = \sum_{n=1}^{\infty} \Pi_n \left|\Phi_n\right\rangle \left\langle\Phi_n\right|$

$$\mathrm{Y}^{(4)}(t) = \mathbf{Tr}(\hat{\Pi}\rho^{(4)}(t)) = \langle \hat{\Pi}\rho^{(4)}(t)\rangle \tag{2.1.20}$$

where the coefficients Π_n depend on the detection method and denote the contribution of the population in an eigenstate $|\Phi_n\rangle$ of the system Hamiltonian $\hat{\mathcal{H}}_0$ to the measured signal [47–49]. The total signal thus reads

$$\mathrm{Y}^{(4)}(t) = \int_0^\infty \mathrm{d}\tau_4 \int_0^\infty \mathrm{d}\tau_3 \int_0^\infty \mathrm{d}\tau_2 \int_0^\infty \mathrm{d}\tau_1 \, Q^{(4)}(\tau_4, \tau_3, \tau_2, \tau_1)E(t-\tau_4) \times E(t-\tau_4-\tau_3)E(t-\tau_4-\tau_3-\tau_2)E(t-\tau_4-\tau_3-\tau_2-\tau_1)\,, \tag{2.1.21}$$

with

$$Q^{(4)}(\tau_4, \tau_3, \tau_2, \tau_1) = \left(\frac{\mathrm{i}}{\hbar}\right)^4 \langle \hat{\Pi}_I(\tau_4+\tau_3+\tau_2+\tau_1) \times [\hat{\mu}_I(\tau_3+\tau_2+\tau_1), [\hat{\mu}_I(\tau_2+\tau_1), [\hat{\mu}_I(\tau_1), [\hat{\mu}_I(0), \rho(0)]]]]\rangle\,. \tag{2.1.22}$$

The projection operator has also been recast into the interaction picture, thereby becoming dependent on the time intervals between the interactions. This response function is very similar to the third-order response of Eq. (2.1.19) and therefore indicates that fourth-order signals originating from incoherent populations also contain information about the coherent evolution of the quantum system. In order to distinguish coherence-based from population-based response functions, the latter is denoted with $Q^{(n)}$. When detecting this population in the experiment, e.g., via fluorescence, the signal is practically integrated over time t by the detector. This yields the time averaged fourth-order signal

$$\overline{\mathrm{Y}}^{(4)} = \int_{-\infty}^{\infty} \mathrm{d}t\, \mathrm{Y}^{(4)}(t)\,. \tag{2.1.23}$$

However, the integration is generally not necessary as the fourth-order population can also be read out at any given time by an additional probe-laser pulse. Proposals for time- and frequency gating have been made to separate contributions of different states to the overall population-based signal [50].

The fourth-order response function $Q^{(4)}(\tau_4, \tau_3, \tau_2, \tau_1)$ contains $2^4 = 16$ different terms

$$Q^{(4)}(\tau_4, \tau_3, \tau_2, \tau_1) = \left(\frac{\mathrm{i}}{\hbar}\right)^4 \sum_{k=1}^{8} \left[Q_k(\tau_4, \tau_3, \tau_2, \tau_1) + Q_k^*(\tau_4, \tau_3, \tau_2, \tau_1)\right]\,. \tag{2.1.24}$$

where $Q_k(\tau_4, \tau_3, \tau_2, \tau_1)$ and its complex conjugate $Q_k^*(\tau_4, \tau_3, \tau_2, \tau_1)$ are called *Liouville pathways* [29]. They can be obtained by explicitly calculating the commutators in Eq. (2.1.22), leading to

$$\begin{aligned}
Q_1(\tau_4, \tau_3, \tau_2, \tau_1) &= +\langle \hat{\Pi}\hat{\mu}_4\hat{\mu}_1\rho(0)\hat{\mu}_2\hat{\mu}_3\rangle\,, & Q_5(\tau_4, \tau_3, \tau_2, \tau_1) &= -\langle \hat{\Pi}\hat{\mu}_1\rho(0)\hat{\mu}_2\hat{\mu}_3\hat{\mu}_4\rangle \\
Q_2(\tau_4, \tau_3, \tau_2, \tau_1) &= +\langle \hat{\Pi}\hat{\mu}_4\hat{\mu}_2\rho(0)\hat{\mu}_1\hat{\mu}_3\rangle\,, & Q_6(\tau_4, \tau_3, \tau_2, \tau_1) &= -\langle \hat{\Pi}\hat{\mu}_2\rho(0)\hat{\mu}_1\hat{\mu}_3\hat{\mu}_4\rangle \\
Q_3(\tau_4, \tau_3, \tau_2, \tau_1) &= +\langle \hat{\Pi}\hat{\mu}_4\hat{\mu}_3\rho(0)\hat{\mu}_1\hat{\mu}_2\rangle\,, & Q_7(\tau_4, \tau_3, \tau_2, \tau_1) &= -\langle \hat{\Pi}\hat{\mu}_3\rho(0)\hat{\mu}_1\hat{\mu}_2\hat{\mu}_4\rangle \\
Q_4(\tau_4, \tau_3, \tau_2, \tau_1) &= +\langle \hat{\Pi}\hat{\mu}_4\hat{\mu}_3\hat{\mu}_2\hat{\mu}_1\rho(0)\rangle\,, & Q_8(\tau_4, \tau_3, \tau_2, \tau_1) &= -\langle \hat{\Pi}\hat{\mu}_3\hat{\mu}_2\hat{\mu}_1\rho(0)\hat{\mu}_4\rangle\,.
\end{aligned} \tag{2.1.25}$$

The complex conjugates have been omitted for brevity. Furthermore, $\hat{\mu}_1 = \hat{\mu}_I(0)$, $\hat{\mu}_2 = \hat{\mu}_I(\tau_1)$, $\hat{\mu}_3 = \hat{\mu}_I(\tau_1 + \tau_2)$, $\hat{\mu}_4 = \hat{\mu}_I(\tau_1 + \tau_2 + \tau_3)$, and $\hat{\Pi} = \hat{\Pi}_I(\tau_4 + \tau_3 + \tau_2 + \tau_1)$ is used.

In Eq. (2.1.25), the Liouville pathways in the left column correspond to the

$2^3 = 8$ (including complex conjugates) response functions $S^{(3)}(t)$ that are measured in coherence-based 2D spectroscopy [Eq. (2.1.19)], with $\hat{\mu}_4$ in this case standing for an emission process and acting on the left-hand side of the density matrix by convention[1]. Contrary to this, in population-based 2D spectroscopy the last interaction with $\hat{\mu}_4$ in the response function [Eq. (2.1.22)] is part of the commutator and thus of the perturbative expansion $\rho^{(4)}$, leading to additional Liouville pathways not present in $S^{(3)}(t)$. The fourth-order response function contains terms with $\hat{\mu}_4$ acting on the left-hand site *and* it also contains terms with $\hat{\mu}_4$ acting on the right-hand site of the density matrix. These additional contributions of opposite sign are given by the Liouville pathways in the right column of Eq. (2.1.25).

Including the projection operator $\hat{\Pi}$ in the response function is of utmost importance for describing the detection of fourth-order signals, since Eq. (2.1.24) identically sums to zero if the projection is neglected (or if all states contribute equally). For instance, using fluorescence detection, Liouville pathways that end in the ground state population after four interactions do not contribute to the detected signal. They would otherwise cancel with corresponding pathways of opposite sign ending in an excited state. The role of the projection operator is further discussed with an example in the following paragraph.

2.1.3 Selected Response Functions and Their Properties

The different Liouville pathways $Q_k(\tau_4, \tau_3, \tau_2, \tau_1)$ and their complex conjugates are of particular interest in time-resolved spectroscopy, as they contain information about molecular coupling, dephasing processes, or population lifetimes. In this section, the most common Liouville pathways of coherent 2D spectroscopy will be introduced and the ordering of the interactions with the electric field visualized using double-sided *Feynman diagrams* [29].

In 2D spectroscopy as performed in this work, the incident electric field consists of a sequence of four laser pulses centered at times t_i,

$$E(\mathbf{r}, t) = \sum_{i=1}^{4} \left[E^{+}(\mathbf{r}, t_i) + E^{-}(\mathbf{r}, t_i) \right] , \tag{2.1.26}$$

with $E^{+}(\mathbf{r}, t_i) = A(t - t_i)\mathrm{e}^{-\mathrm{i}(\omega(t-t_i) - \mathbf{k_i}\mathbf{r} - \phi_i)}$. $E^{-}(\mathbf{r}, t_i)$ denotes the complex conjugate. Since collinear pulses ($\mathbf{k_i} = \mathbf{k}$) are used in the experiments of this work and

[1] The side of the last interaction can be chosen arbitrarily as it is not part of the expansion of $\rho^{(3)}$ and only appears when calculating the trace that is invariant under cyclic permutation, $\langle \hat{\mu}_4 \rho^{(3)}(t) \rangle = \langle \rho^{(3)}(t) \hat{\mu}_4 \rangle$ [29].

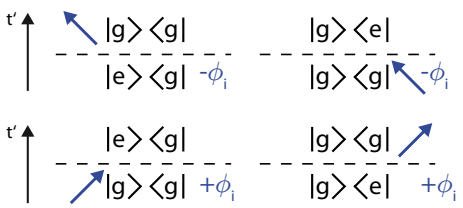

Figure 2.2: Sign convention for interactions with the density matrix. The bra and kets below (above) the dashed line indicate the state of the density matrix before (after) the interaction, i.e., time is evolving from bottom to top. The ground state is denoted by $|g\rangle$ and the excited state by $|e\rangle$. An arrow pointing to the left contributes with $-\phi_i$, an arrow pointing to the right with $+\phi_i$.

no coherently emitted signal is detected, the wavevectors of the electromagnetic field defined in Eq. (2.1.26) can be neglected in the following. The product of electric fields in Eq. (2.1.21) contains $8^4 = 4096$ terms. Thus, Eq. (2.1.21) sums up to $4096 \times 16 = 65536$ different contributions, including the complex conjugates. Imposing strict time ordering of the four laser pulses ($t_1 < t_2 < t_3 < t_4$) and applying the *rotating-wave approximation* (RWA) under the assumption that rapidly oscillating contributions can be neglected significantly reduces the number of terms that need to be considered [29–31].

The remaining contributions differ in the way the laser pulses (and hence the transition dipole operators) interact with the density matrix as shown schematically in Fig. 2.2 for a single interaction. They can either occur from the left- or from the right-hand side as for the Liouville pathways in Eq. (2.1.25) and can contribute with a positive phase resulting from $E^+(\mathbf{r}, t_i)$ or a negative phase originating from $E^-(\mathbf{r}, t_i)$. This leads to an overall signal phase ϕ_S after four interactions

$$\phi_S = \alpha\phi_1 + \beta\phi_2 + \gamma\phi_3 + \delta\phi_4 \,. \tag{2.1.27}$$

The Greek indices $\alpha, \beta, \gamma, \delta \in \mathbb{Z}$ represent the number and type of interaction of each of the four pulses with the density matrix. For example, for $\alpha = -1$, the first pulse interacts once, resulting in a phase factor $\mathrm{e}^{-\mathrm{i}\phi_1}$. In general, if this interaction with $\alpha = -1$ is on the right (left) of the density matrix, this contribution is considered to correspond to absorption (emission). For $\alpha = +1$, the roles are interchanged and interaction from the right (left) corresponds to emission (absorption) [29].

Parameterizing the time-averaged fourth-order signal [Eq. (2.1.23)] with the relative delays between the four laser pulses, $\tau = t_1 - t_2$, $T = t_3 - t_2$, $t = t_4 - t_3$ and their phases $\phi_1, \phi_3, \phi_3, \phi_4$, it can be written as a sum over the different signal

contributions $\tilde{Y}^{(4)}(\tau, T, t, \alpha, \beta, \gamma, \delta)$

$$\overline{Y}^{(4)}(\tau, T, t, \phi_1, \phi_2, \phi_3, \phi_4) = \sum_{\alpha,\beta,\gamma,\delta} \tilde{Y}^{(4)}(\tau, T, t, \alpha, \beta, \gamma, \delta) \mathrm{e}^{\mathrm{i}(\alpha\phi_1+\beta\phi_2+\gamma\phi_3+\delta\phi_4)}\,, \tag{2.1.28}$$

where each contribution has a total phase determined by the values of $(\alpha, \beta, \gamma, \delta)$. The individual term $\tilde{Y}^{(4)}(\tau, T, t, \alpha, \beta, \gamma, \delta)$ in Eq. (2.1.28) itself is a sum over those response functions $Q_k(\tau_4, \tau_3, \tau_2, \tau_1)$ introduced in Eq. (2.1.25) that survive time ordering and the rotating-wave approximation for the given interactions (α, β, γ, δ). That means that each signal contribution with a certain phase ϕ_S contains all Liouville pathways Q_k with the phase dependency ϕ_S.

Rephasing Contribution

One of the most interesting signal contributions in multidimensional spectroscopy is the *rephasing* signal, also known as *photon echo*, the optical analogue to the spin echo of nuclear magnetic resonance [51–53].

The rephasing signal has a total phase $\phi_S = -\phi_1 + \phi_2 + \phi_3 - \phi_4$ that is therefore originating from the interaction pattern with the incident four-pulse sequence according to $\alpha = -1$, $\beta = +1$, $\gamma = +1$, $\delta = -1$. It contains several different Liouville pathways $Q_k(\tau_4, \tau_3, \tau_2, \tau_1)$ out of which those that end in an excited state are shown in the double-sided Feynman diagrams of Fig. 2.3 (a) for a hypothetical three-level system consisting of a ground state $|g\rangle$, a first excited state $|e\rangle$, and a second excited state $|f\rangle$. In analogy to their counterparts in coherence-based 2D spectroscopy, the pathways are often labeled *ground-state bleach* (GSB) for a pump-induced decreased absorbance, *stimulated emission* (SE) for a pump-induced enhanced emission, and *excited-state absorption* (ESA) for a pump-induced increased absorbance into the second excited state $|f\rangle$. In the following, a simplified analytic expression based on solutions of the optical Bloch equations shall be constructed for the stimulated-emission response function, illustrating exemplarily the different steps in the time-evolution of the density matrix for a single Liouville pathway [31, 54].

Starting with only ground state population $|g\rangle\langle g|$, the density matrix is in a coherence $|g\rangle\langle e|$ after the first interaction (blue arrow, SE), contributing with $\mu_{ge}\mathrm{e}^{-\mathrm{i}\phi_1}$ to the response function. This coherence evolves subject to the system Hamiltonian during the first coherence time τ and decays due to system-bath interaction (see below). The free evolution and decay can be described by an additional factor $\mathrm{e}^{-(\mathrm{i}\omega_{ge}+\Gamma_{ge})\tau}$ in the response function, such that the first-order

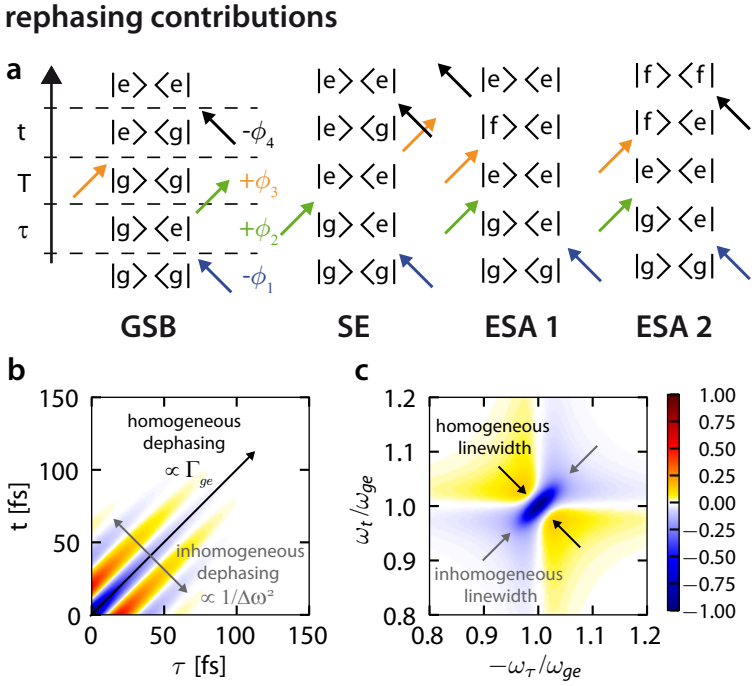

Figure 2.3: Rephasing signal contributions. (a) Double-sided Feynman diagrams of Liouville pathways fulfilling the rephasing phase condition. (b) Stimulated emission (SE) time-domain signal elongated on the diagonal. (c) The corresponding frequency-domain signal has a peak centered at $(-\omega_{ge}, +\omega_{ge})$. In the homogeneous and inhomogeneous limit, the homogeneous linewidth can be obtained from a cut along the cross-diagonal and the inhomogeneous linewidth from the diagonal.

time evolution can be written as

$$\rho_{ge}^{(1)}(\tau) = \mu_{ge} \mathrm{e}^{-\mathrm{i}\phi_1} \mathrm{e}^{-(\mathrm{i}\omega_{ge}+\Gamma_{ge})\tau} \Theta(\tau)\,. \tag{2.1.29}$$

The second interaction (green arrow, SE) with $\mu_{ge}\mathrm{e}^{+\mathrm{i}\phi_2}$ creates the excited-state population $|e\rangle\langle e|$ that can relax during the population time T with a rate Γ_{ee}, leading to

$$\rho_{ee}^{(2)}(\tau, T) = \mu_{ge}^2 \mathrm{e}^{\mathrm{i}(-\phi_1+\phi_2)} \mathrm{e}^{-(\mathrm{i}\omega_{ge}+\Gamma_{ge})\tau} \mathrm{e}^{-\Gamma_{ee}T} \Theta(\tau)\Theta(T)\,. \tag{2.1.30}$$

Subsequently, the third interaction (orange arrow, SE) with $\mu_{ge}\mathrm{e}^{+\mathrm{i}\phi_3}$ prepares the coherence $|e\rangle\langle g|$ that evolves with $\mathrm{e}^{-(\mathrm{i}\omega_{eg}+\Gamma_{eg})t}$ during the second coherence time t. Using $\omega_{eg} = -\omega_{ge}$ and $\Gamma_{eg} = \Gamma_{ge}$, the time evolution of the third-order coherence

is given by

$$\rho_{eg}^{(3)}(\tau,T,t) = \mu_{ge}^3 \mathrm{e}^{\mathrm{i}(-\phi_1+\phi_2+\phi_3)} \mathrm{e}^{-\mathrm{i}\omega_{ge}(\tau-t)-\Gamma_{ge}(\tau+t)} \mathrm{e}^{-\Gamma_{ee}T} \Theta(\tau)\Theta(T)\Theta(t)\,. \quad (2.1.31)$$

The fourth interaction (black arrow, SE) with $\mu_{ge}\mathrm{e}^{-\mathrm{i}\phi_4}$ transforms this coherence into an excited-state population that can finally be detected. Thus, the total population after the four interactions can be written as [31, 54, 55]

$$\rho_{ee}^{(4)}(\tau,T,t) = \mu_{ge}^4 \mathrm{e}^{-\mathrm{i}\phi_S} \mathrm{e}^{-\mathrm{i}\omega_{ge}(\tau-t)-\Gamma_{ge}(\tau+t)} \mathrm{e}^{-\Gamma_{ee}T} \mathrm{e}^{-\frac{\Delta\omega^2}{2}(\tau-t)^2} \Theta(\tau)\Theta(T)\Theta(t)\,, \quad (2.1.32)$$

where inhomogeneous broadening has been taken into account by the additional damping factor $\mathrm{e}^{-\frac{\Delta\omega^2}{2}(\tau-t)^2}$ [31, 54, 55]. It will be discussed at the end of this chapter.

The characteristic feature of the rephasing signal is the fact that the density matrix is in a coherence during the two time intervals τ and t and that the coherences oscillate during τ with a frequency of opposite sign than during t. The opposite sign can originate from conjugate coherences ($|e\rangle\langle g|$ and $|g\rangle\langle e|$) or from coherences involving different states ($|e\rangle\langle g|$ and $|e\rangle\langle f|$). In any case, the phase evolution (and hence the dephasing processes) during the first coherence time τ is reversed during the second coherence time t, such that all oscillators are again in phase at $t = \tau$ and an "echo" appears.

Figure. 2.3 (b) illustrates the signal properties of the time-domain rephasing response function, calculated from Eq. (2.1.32) for a center frequency $\omega_{ge} = 0.15$ rad fs^{-1}, a dephasing time constant of $\Gamma_{ge} = 1/45$ fs^{-1}, and $\Delta\omega^2 = 1.5\,\Gamma_{ge}$. The signal is damped along the diagonal $\tau = t$ with a time constant proportional to the homogeneous dephasing rate [Fig. 2.3 (b)]. It further oscillates in the direction of the cross-diagonal with the frequency of the transition ω_{ge}. This oscillation is determined by the factor $\mathrm{e}^{-\mathrm{i}\omega_{ge}(\tau-t)}$. The decay of this oscillation is governed by the amount of inhomogeneous broadening. For large inhomogeneity, the damping is strong and the signal is concentrated along the time-domain diagonal, which is the manifestation of the photon echo appearing at $t = \tau$. In contrast, for a homogeneous ensemble, the oscillations are not damped and no echo appears. A 2D Fourier transformation of the time-domain signal with respect to the two coherence times τ and t generates the 2D spectrum with a peak centered at ($\omega_\tau = -\omega_{ge}$, $\omega_t = +\omega_{ge}$). In the limit of either a mainly homogeneous or a mainly inhomogeneous sample, the linewidth along the diagonal is determined by inhomogeneous broadening, whereas the narrow cross-diagonal width is mostly governed by homogeneous broadening [Fig. 2.3 (c)]. For arbitrary inhomogeneity,

a mixing between the two broadening mechanisms occurs and the (cross-) diagonal linewidths contains contributions of both broadenings [54].

The total rephasing signal contains the sum of all Liouville pathways [Fig. 2.3 (a)] that contribute depending on the quantum yield Π_n of the final state $|e\rangle$ or $|f\rangle$ and the sign of the Liouville pathway, such that

$$\tilde{Y}^{(4)}_{reph}(\tau, T, t) = \Pi_e(-\mathbf{GSB} - \mathbf{SE} - \mathbf{ESA_1}) + \Pi_f \mathbf{ESA_2}\,. \tag{2.1.33}$$

Due to the different signs of the two excited-state absorption pathways $\mathbf{ESA_1}$ and $\mathbf{ESA_2}$, (partial) cancellation of these two contributions determined by the quantum yield of the final states can occur, which can significantly alter the appearance of the 2D spectrum [47–49].

Nonrephasing Contribution

The nonrephasing contribution is also composed of multiple Liouville pathways that have a similar interaction pattern as their rephasing counterparts, with the density matrix being in a coherence during the two time intervals τ and t. However, in the nonrephasing contribution the dephasing of oscillators during the first coherence time is *not* reversed during the second coherence time, since the density matrix is in a coherence with the same sign during τ and t [Fig. 2.4 (a)]. The analytic expression of the time-domain stimulated-emission contribution can be derived in the same way as for the rephasing signal, leading to

$$\rho^{(4)}_{ee}(\tau, T, t) = \mu^4_{ge} \mathrm{e}^{-\mathrm{i}\phi_S} \mathrm{e}^{\mathrm{i}\omega_{eg}(\tau+t) - \Gamma_{ge}(\tau+t)} \mathrm{e}^{-\Gamma_{ee}T} \mathrm{e}^{-\frac{\Delta\omega^2}{2}(\tau+t)^2} \Theta(\tau)\Theta(T)\Theta(t)\,, \tag{2.1.34}$$

with a total phase of $\phi_S = +\phi_1 - \phi_2 + \phi_3 - \phi_4$.

Since no rephasing takes place during the second coherence time, the signal quickly decays along the time-domain diagonal and does not show an echo signal at $\tau = t$ [Fig. 2.4 (b)]. Instead, the inhomogeneous broadening also affects the signal decay along the diagonal direction and damps the time-domain signal in addition to the homogeneous dephasing, but on a much faster timescale. The 2D spectrum of the nonrephasing signal exhibits a broad peak that does not allow to retrieve the homogeneous linewidth of the transition, since the peak is broadened in the direction of the homogeneous linewidth by the inhomogeneous contribution. As the oscillation frequencies of both coherence times do not have opposite signs, the peak is centered at ($\omega_\tau = +\omega_{ge}$, $\omega_t = +\omega_{ge}$) [Fig. 2.4 (c)].

In combination with the rephasing signal, the nonrephasing contribution allows to remove phase twists present in both contributions that are originating from a

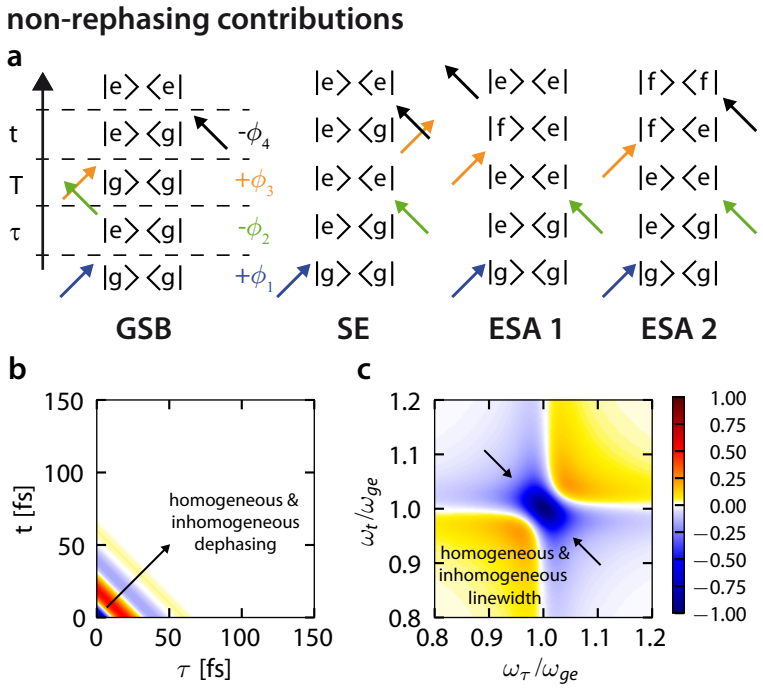

Figure 2.4: Nonrephasing signal contributions. (a) Double-sided Feynman diagrams of Liouville pathways fulfilling the nonrephasing phase condition. (b) Stimulated emission (SE) time-domain signal, rapidly decaying along the diagonal $t = \tau$. (c) The corresponding frequency-domain signal centered at $(+\omega_{ge}, +\omega_{ge})$ shows a broad peak from which the homogeneous linewidth cannot be determined (see text).

mixing of absorptive and dispersive signal parts. For this, the rephasing signal can simply be mirrored at the $\omega_\tau = 0$ axis and added to the nonrephasing signal. This retrieves the purely absorptive (real part) and purely dispersive (imaginary part) 2D spectrum [56, 57].

Lineshape Functions

The response-function formalism and the signal contributions presented so far included open quantum systems that can interact with a surrounding bath by phenomenological damping factors. They will be explained briefly in this paragraph.

The coupling of a quantum system to the local environment and to the bath degrees of freedom causes small energy–level fluctuations and thus a variation $\delta\omega$ of the momentary transition frequency ω_{eg} on a very fast timescale (typically $<$ 100 fs). For a single molecule, this affects the coherence prepared by the excitation

laser pulse and slightly alters the oscillation frequency at various points in time. In an ensemble, the initially phase-coherent prepared oscillations (coherences) of multiple molecules can therefore quickly run out of phase, leading on average to a decay of the macroscopic oscillation. This dephasing gives rise to the *homogeneous* linewidth of the transition.

Additionally, an initial distribution $\Delta\omega_{eg}$ of transition frequencies at the laser excitation step causes *inhomogeneous* broadening. The different initial transition frequencies can evolve on a rather slow (picosecond) timescale after excitation due to changes in the local environment, e.g., re-orientation of the surrounding solvent, leading to spectral diffusion [29, 31]. Generally, the bath influence on the free evolution of the quantum system subject to the system Hamiltonian can be considered in the theoretical description of the response function using Kubo's lineshape theory or the Brownian oscillator model [29], introducing an additional damping factor $\mathrm{e}^{-g(t)}$. The lineshape function $g(t)$ treats fluctuations of the transition frequency and is calculated via [31, 55]

$$g(t) = \int_0^t \mathrm{d}\tau' \int_0^{\tau'} \mathrm{d}\tau'' \langle \delta\omega_{eg}(\tau'')\delta\omega_{eg}(0)\rangle \,. \tag{2.1.35}$$

Here, $\langle \delta\omega_{eg}(\tau'')\delta\omega_{eg}(0)\rangle$ denotes the frequency-frequency correlation function [29, 31] and describes how fast the correlation between the initial transition frequency $\delta\omega_{eg}(0)$ and the frequency at later times $\delta\omega_{eg}(\tau'')$ is lost due to the influence of the surrounding bath. Often, the lineshape function $g(t) = \Gamma_{eg}t + \frac{\Delta\omega_{eg}^2}{2}t^2$ is used, where Γ_{eg} treats the homogeneous dephasing and therefore the decay of the $|e\rangle\langle g|$ coherence due to rapid frequency fluctuations. Likewise, the second term handles the inhomogeneity of the ensemble and assumes an initial Gaussian distribution of transition frequencies ω_{eg}. The homogeneous dephasing leads to a Lorentzian absorption profile with a linewidth proportional to Γ_{eg}^{-1} that is convoluted with a Gaussian frequency distribution of a width proportional to $1/\Delta\omega_{eg}^2$, resulting in a Voigt profile of the absorption line. A detailed treatment of optical (nonlinear) response functions with relaxation due to system-bath interaction can be found in various textbooks [29–31].

2.2 Coherent Two-Dimensional (2D) Electronic Spectroscopy

Having discussed the basic properties of third- or fourth-order nonlinear signals and how they can be described using the response-function formalism, this section is intended to introduce the properties of 2D spectra in general and to review experimental approaches of coherent two-dimensional (2D) electronic spectroscopy (2DES), aiming to classify the method of this work into the meanwhile large amount of experimental realizations. Several textbooks [30, 31, 35] and review articles [28, 32–34, 37] are dedicated to experimental aspects of 2D spectroscopy and treat the information content of 2D spectra and acquisition strategies in detail.

The first paragraph explains basic properties of 2D spectra that is followed by comparing coherence-based third-order 2D spectroscopy methods with population-based fourth-order approaches. Finally, the last paragraph shows a method to distinguish different contributions defined by the parameters (α, β, γ, δ) to the total signal using *phase cycling* [58, 59].

2.2.1 Information Content of a 2D Spectrum

A 2D spectrum visualizes the properties of the nonlinear response functions in frequency space by correlating two frequency axes in readily understandable two-dimensional maps. Typically, a 2D spectrum is considered to display the rephasing, non-rephasing or absorptive response function, connecting the excitation (pump) frequency with the detection (probe) frequency. Compared to standard transient-absorption techniques, the method of coherent 2D spectroscopy gains more insight into the ensemble of molecules by additionally resolving the excitation frequency and therefore enables to discriminate the contribution of different states to the emission/absorption at a given frequency. Thus, the method unravels the otherwise congested spectral response.

As an example, Fig. 2.5 schematically displays a 2D spectrum for a pair of uncoupled (left) and coupled (right) chromophores. Both systems can not be distinguished spectroscopically by their linear excitation spectrum (top) or their transient-absorption signal (right). The inter-chromophoric coupling can only be uncovered by resolving excitation and detection frequencies using 2D spectroscopy. Peaks on the diagonal of both 2D spectra indicate resonances of the two individual chromophores showing emission/absorption at the excitation frequency (red). Off-diagonal crosspeaks (right spectrum, orange peak) reveal a signal at a frequency

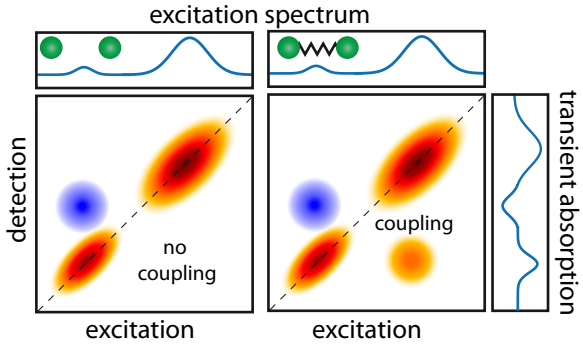

Figure 2.5: Structure and information content of 2D spectra. Diagonal peaks indicate resonances of the single chromophores (green spheres), cross peaks (orange) reveal coupling between the two chromophores. Other off-diagonal peaks (blue) indicate excited-state absorption or photochemical processes, such as product formation. Both species cannot be discriminated by their excitation spectrum (top) or their transient absorption spectrum (right).

other than the excitation and uncover the aforementioned coupling between the quantum states of the two chromophores that can be mediated, e.g., via a common ground state (strong coupling) or via energy transfer. Other off-diagonal peaks contain information on the absorption of excited states or the formation of a reaction product at larger population times (blue peaks in both spectra). The evolution of peak shapes and amplitudes as a function of population time T contains information about the dynamics of energy-transport processes, e.g., in light-harvesting complexes [23, 26, 60–63]. Further applications of coherent 2D spectroscopy include, among others, the investigation of electronic or vibrational dynamics in semiconductors [49, 64–68] or on surfaces [69–71], temperature-dependent conformation changes [72, 73], or reaction pathways in photochemistry [74, 75].

2.2.2 Review: Experimental Approaches in 2D Spectroscopy

Providing simultaneously a large spectral bandwidth and high time resolution, the Fourier-transform version of 2D optical spectroscopy [53] was developed from ideas of multidimensional nuclear magnetic resonance techniques [76]. Phase stability between the incident laser pulses is a crucial experimental requirement, as the method involves at least one Fourier transformation over a coherence-time axis. Consequently, optical 2D spectroscopy has been realized first in the IR [77–80] and NIR spectral region [53, 58, 81], relaxing the stability conditions due to the larger wavelength and enabling to retrieve structural information via the study of molecular vibrations. Later on, sophisticated inherently phase-stable setups have been realized in the visible [82–86] and ultraviolet regime [87–91]. Recently, 2D spectroscopy has been reported using THz pulses [92–94] where the experimental

challenge lies in the detection of the weak emitted electric field via electro-optical sampling. Additionally, first proposals have been made to push the method to shorter wavelength using attosecond X-ray pulses [95–97].

As introduced in Chap. 2.1, two major acquisition approaches may be distinguished, whereas the first relies on the detection of coherently emitted third-order signals generated by $P^{(3)}(t)$, and the second on incoherent, population-based fourth-order signals originating from $Y^{(4)}(t)$.

Coherence-Based 2D Spectroscopy

In coherence-based 2D spectroscopy the sample's third-order polarization $P^{(3)}(t)$, generated by the interaction with three laser pulses, leads to the emission of an electromagnetic signal field $E_{\mathrm{sig}}(t) \propto \mathrm{i}P^{(3)}(t)$. A macroscopic signal only builds up in a direction where the emission of all microscopic emitters interferes constructively, which is known as *phase matching* [98, 99]. The wavevector of the emitted signal depends on the wavevectors of the excitation pulses according to

$$\mathbf{k_S} = \alpha\mathbf{k_1} + \beta\mathbf{k_2} + \gamma\mathbf{k_3}\,, \tag{2.2.1}$$

with the Greek indices (α, β, γ) indicating the type of signal as introduced in Chap. 2.1.3. For example, the photon echo ($\alpha = -1$, $\beta = +1$, $\gamma = +1$) is emitted into $\mathbf{k_S} = -\mathbf{k_1} + \mathbf{k_2} + \mathbf{k_3}$.

Arranging the beams in the so-called box geometry [Fig. 2.6 (a)] exploits this directional dependence of the signal. The coherently emitted signal field (at $t = \tau$ in case of the photon echo) is detected via spectral interference with an additional reference pulse co-propagating with the signal (heterodyne detection) by placing a spectrometer in the phase-matching direction [100]. Fourier transformation of this spectrally dispersed signal with respect to the first coherence time τ generates the 2D spectrum. Since the exact temporal overlap of the pulses ($\tau = 0$) cannot be determined with sufficient precision in the experiment, a *phasing* step is necessary during data analysis that removes this uncertainty [82].

The beam geometry in general allows to acquire only one type of signal at once and needs to be altered if other signals, e.g. two-quantum coherences ($\alpha = +1$, $\beta = +1$, $\gamma = -1$), should be measured. Depending on the experimental setup, this can be done by exchanging the time ordering of the incident pulses while keeping the geometry unchanged. The spatial separation of the three incident beams grants access to control their polarization by inserting waveplates into the beam path. This can be used to enhance or suppress transitions and thus, peaks

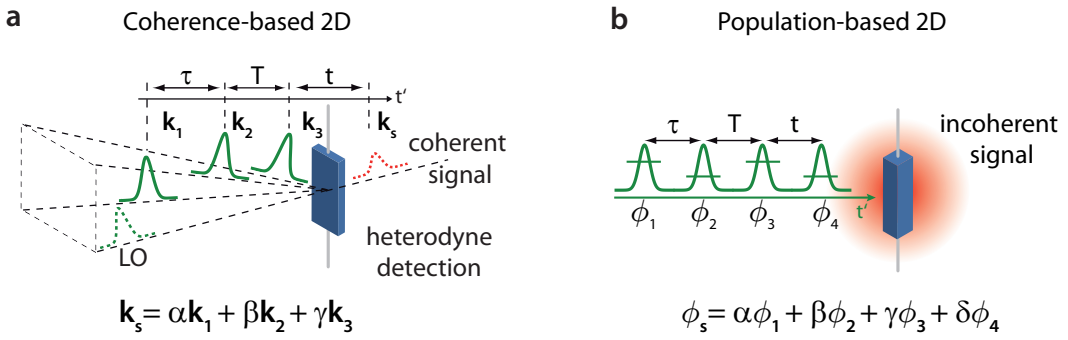

Figure 2.6: Acquisition approaches in 2D spectroscopy. (a) In coherence-based 2D spectroscopy the incident pulses are frequently arranged in box geometry. Heterodyned detection of coherently emitted signals into the phase-matching direction given by $\mathbf{k_S}$ is used. (b) In population-based 2D spectroscopy the incident pulses are often arranged in a collinear geometry and detection of incoherent signals, like fluorescence, is used. Instead of the directional dependence, the phase dependence of the different signal contributions is employed for signal selection in this case.

in the 2D spectrum [101, 102] or to implement chiral 2D spectroscopy [61].

A second coherence-based approach uses the transient-absorption geometry comprising a pump and a broadband probe pulse and generates the excitation axis of the 2D spectrum by splitting the single pump pulse into a phase-coherent double pulse separated by the coherence time τ. A double pulse is generated either with a pulse shaper [103–105] or by opto-mechanical means [106, 107]. The probe pulse typically consists of a broadband white-light continuum and enables the direct acquisition of the absorptive 2D spectrum with an emission axis spanning an octave in the visible spectral range. In this experimental configuration, oscillations of coherences during τ are overlaid by additional, typically non-oscillating pump–probe contributions and can be extracted either via Fourier filtering [106, 107] or phase cycling (see below).

Population-Based 2D Spectroscopy

This work focuses on population-based 2D spectroscopy and the detection of fourth-order populations via incoherent signals. Detecting populations paves the way for new samples and corresponding observables in 2D electronic spectroscopy, as they can be converted into fluorescence [48, 72, 108, 109], a current of external [69] or internal [49, 65, 67] photoelectrons, or cations as introduced in this work. If necessary, an additional read-out pulse can be used to transfer the final-

state population into a measurable signal. Since no macroscopic phase-matching condition needs to be fulfilled, a simplified collinear geometry [Fig. 2.6 (b)] can be used. Incoherent signals can be detected with superior sensitivity even down to the single-emitter limit. This sensitivity gain can be used, e.g., to visualize and control vibrational wave packets in single molecules [110, 111]. The flexibility on the choice of observables grants access to various types of samples from condensed matter to the gas phase.

When detecting incoherent observables, the measured signal contains all Liouville pathways [Eq. (2.1.28)] simultaneously and different means of extracting the desired contribution parameterized by (α, β, γ, δ) need to be used. Similar to the directional dependence in box geometry, the phase dependence

$$\phi_S = \alpha\phi_1 + \beta\phi_2 + \gamma\phi_3 + \delta\phi_4 \tag{2.2.2}$$

can be exploited in the collinear case by repeating the measurement with different combinations of the laser-pulse phases and analyzing the signals accordingly. Generally, two methods should be distinguished that rely on phase control and are explained in the following.

Phase modulation, as pioneered by Marcus et al. [108], is a technique that uses three nested interferometers to split a single input pulse into four collinear output pulses [Fig. 2.7 (a)]. Each interferometer arm contains an acousto-optic modulator (AOM) [112] that continuously changes the carrier-envelope phase (CEP) of the transmitted laser pulse by the interaction of the optical pulse with an acoustic wave (Chap. 3.2.1). Since the four AOMs in the setup are each driven with a unique radio frequency, the carrier-envelope phases of the four output pulses are modulated with an individual rate between 0 and 2π, leading to a different phase combination for every laser shot. This results in a modulation of the detected signal over consecutive laser shots. As the distinct signal contributions yield a different total phase ϕ_S, their amplitudes oscillate at different frequencies due to this phase modulation.

On-the-fly demodulation and hence, extraction of the signal of interest, is achieved using lock-in detection where the reference frequency of the lock-in detector is set to the modulation frequency of the desired contribution.

This frequency can be derived by electronically mixing three reference signals resulting from interfering beams at different positions in the interferometer [Ref 1, Ref 2, and Ref 3 in Fig. 2.7 (a)]. The monochromatic reference can either be obtained from a cw laser running through the same interferometer [65, 113] or from a split portion of the original pulse guided through a monochromator [108].

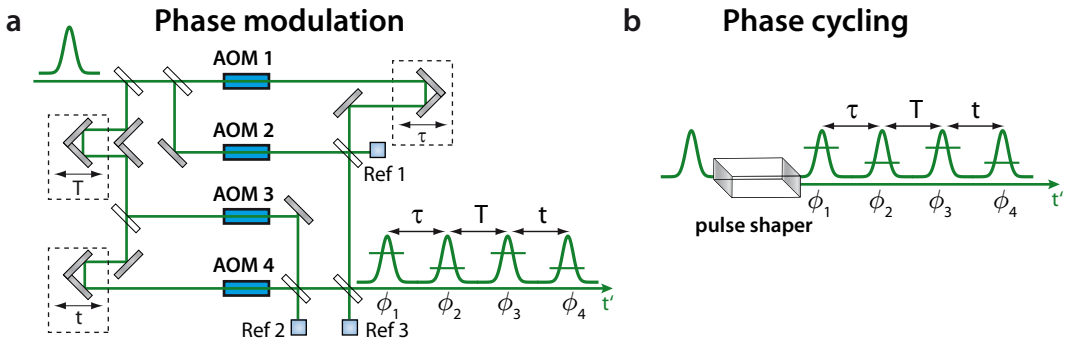

Figure 2.7: Acquisition concepts via phase control. (a) Phase modulation uses three nested interferometers to generate four collinear pulses. The interpulse phases are shifted shot-to-shot by continuously operated AOMs, leading to a modulated signal. Demodulation is achieved on-the-fly via lock-in detection (not shown). (b) Phase cycling uses a pulse shaper to step through the interpulse phases. Signals are extracted via data analysis.

Phase modulation provides means for efficient undersampling as the signal phase ϕ_S evolves with the difference between signal frequency and reference frequency when the coherence times are scanned. When both frequencies are equal, the demodulated signal does not oscillate while scanning the coherence times such that larger step sizes are possible (see also Chap. 3.2.3). Furthermore, excellent signal-to-noise ratios due to lock-in detection and inherent phase stability are achieved, since the reference beam also passes the interferometer arms and is therefore equally affected by mechanical vibrations than the excitation pulses. However, several lock-in detectors are required if more than one signal contribution should be acquired simultaneously.

A second possibility to extract the signal of interest and the method applied in this work is ***phase cycling*** as introduced by Warren et al. [52, 58]. Here, a pulse shaper is used to generate a train of four phase-stable laser pulses and to step through various combinations of the phases while detecting the signal for each phase combination [Fig. 2.7 (b)]. This avoids spatial separation of the pulses and complicated alignment procedures of four separate beams, but also limits the available scanning range to the shaping window given by the pulse shaper. Modern pulse shapers [114–119] allow to design the full vector field, which not only enables new multidimensional-spectroscopy experiments using a colored pulse sequence with each pulse covering a different spectral region, but also provides the advantages of full polarization control of the four pulses. Furthermore, all signal contributions are acquired simultaneously and thus under the same experimental conditions without the need of additional equipment. The signal of interest is

extracted during data analysis, as shown in detail in the next paragraph.

Comparing both methods, phase modulation can be regarded as shot-to-shot phase cycling with on-the-fly demodulation for selected signal contributions.

2.2.3 Phase Cycling

Since the density matrix of the investigated quantum system is required to be in a population state after the last interaction, the number of absorption and emission processes, i.e., the interactions with positive and negative phase contributions must sum up to zero [59], i.e.,

$$\alpha + \beta + \gamma + \delta = 0\,. \tag{2.2.3}$$

Furthermore, considering only up to four interactions with the incident pulse sequence leads to the additional condition

$$|\alpha| + |\beta| + |\gamma| + |\delta| \leq 4\,. \tag{2.2.4}$$

Equations (2.2.3) and (2.2.4) imply that $Y^{(4)}$-signals as considered here can not have more than two interactions with a single pulse, i.e., $|\alpha|, |\beta|, |\gamma|, |\delta| < 2$. That is fulfilled by 55 different contributions out of which the signal of interest is retrieved [59].

Due to the requirement of ending in a population state after four interactions [Eq. (2.2.3)], only three out of the four indices (α, β, γ, δ) are independent of each other, permitting to consider relative phases $\phi_{21} \equiv \phi_2 - \phi_1$, $\phi_{31} \equiv \phi_3 - \phi_1$, and $\phi_{41} \equiv \phi_4 - \phi_1$ referenced to the phase of the first pulse. Therefore, Eq. (2.1.28) can be reduced to

$$Y^{(4)}(\tau, T, t, \phi_{21}, \phi_{31}, \phi_{41}) = \sum_{\beta,\gamma,\delta} \tilde{Y}^{(4)}(\tau, T, t, \alpha, \beta, \gamma, \delta) \mathrm{e}^{\mathrm{i}(\beta\phi_{21} + \gamma\phi_{31} + \delta\phi_{41})}\,. \tag{2.2.5}$$

which can be identified as a Fourier series with basis functions $\mathrm{e}^{\mathrm{i}(\beta\phi_{21} + \gamma\phi_{31} + \delta\phi_{41})}$ that are parameterized by (β, γ, δ) and are continuous functions of the relative phases ϕ_{21}, ϕ_{31}, and ϕ_{41}. The Fourier coefficient $Y^{(4)}(\tau, T, t, \alpha', \beta', \gamma', \delta')$, i.e., signal contribution, of interest can be obtained by projecting the total signal on the corresponding basis function. This can generally be done by multiplying both sides of Eq. (2.2.5) with the complex conjugate of the desired basis function $\mathrm{e}^{-\mathrm{i}(\beta'\phi_{21} + \gamma'\phi_{31} + \delta'\phi_{41})}$ and integrating over the relative phases, yielding a result other than zero only for the non-oscillating term on the right-hand side of Eq. (2.2.5), where $\beta = \beta'$, $\gamma = \gamma'$, and $\delta = \delta'$. Therefore, the coefficient can be calculated

using this inverse Fourier transformation via

$$\tilde{Y}^{(4)}(\tau,T,t,\alpha',\beta',\gamma',\delta') = \frac{1}{(2\pi)^3}\int_0^{2\pi}\mathrm{d}\phi_{41}\int_0^{2\pi}\mathrm{d}\phi_{31}\int_0^{2\pi}\mathrm{d}\phi_{21} \times Y^{(4)}(\tau,T,t,\phi_{21},\phi_{31},\phi_{41})\mathrm{e}^{-\mathrm{i}(\beta'\phi_{21}+\gamma'\phi_{31}+\delta'\phi_{41})}\,. \quad (2.2.6)$$

For simplicity, the primes are omitted in the following. In the experiment, the phases can only be sampled with discrete steps, which is why Eq. (2.2.6) needs to be replaced by the discrete Fourier transformation [59]

$$\begin{aligned}\tilde{Y}^{(4)}(\tau,T,t,\alpha,\beta,\gamma,\delta) &= \frac{1}{LMN}\sum_{l=0}^{L-1}\sum_{m=0}^{M-1}\sum_{n=0}^{N-1} Y^{(4)}(\tau,T,t,l\,\Delta\phi_{21},m\,\Delta\phi_{31},n\,\Delta\phi_{41}) \\ &\quad\times \mathrm{e}^{-\mathrm{i}\beta l\Delta\phi_{21}}\mathrm{e}^{-\mathrm{i}\gamma m\Delta\phi_{31}}\mathrm{e}^{-\mathrm{i}\delta n\Delta\phi_{41}} \\ &= \frac{1}{LMN}\sum_{l=0}^{L-1}\sum_{m=0}^{M-1}\sum_{n=0}^{N-1} Y^{(4)}(\tau,T,t,l\Delta\phi_{21},m\Delta\phi_{31},n\Delta\phi_{41}) \\ &\quad\times W_L^{l\beta}W_M^{m\gamma}W_N^{n\delta}\,.\end{aligned} \quad (2.2.7)$$

where L, M, and N are the number of sampled points in phase space and $\Delta\phi_{21} = \frac{2\pi}{L}$, $\Delta\phi_{31} = \frac{2\pi}{M}$, and $\Delta\phi_{41} = \frac{2\pi}{N}$ the phase increments. Therefore, in order to retrieve $\tilde{Y}^{(4)}(\tau,T,t,\alpha,\beta,\gamma,\delta)$, the signal $Y^{(4)}(\tau,T,t,\phi_{21},\phi_{31},\phi_{41})$ needs to be acquired for different phases and summed according to Eq. (2.2.7). Since the signal is periodic with respect to the phases, $\tilde{Y}^{(4)}(\tau,T,t,\beta,\gamma,\delta) = \tilde{Y}^{(4)}(\tau,T,t,\beta+pL,\gamma+qM,\delta+rN)$ with $(p,q,r)\in\mathbb{Z}$, aliased signals are introduced if the phases are not sampled with sufficiently high density. For example, a signal with a phase dependence of $\beta = 1$ cannot be discriminated from a signal with $\beta = -2$ when sampling ϕ_{21} in just three equidistant steps between 0 and 2π (Fig. 2.8).

However, three phase-cycling steps per relative phase can already be sufficient in multipulse experiments to uniquely retrieve a contribution with $\beta = 1$. This can be achieved by taking into account the proposition of having only fourth-order signals [Eq. (2.2.4)] and by performing additional phase cycling for the other pulses related to γ and δ, as shown in the following. Considering the rephasing photon-echo contribution with ($\alpha = -1$, $\beta = +1$, $\gamma = +1$, $\delta = -1$) as an example, it can be extracted with a $1\times L\times M\times N = 1\times 3\times 3\times 3$ phase-cycling scheme, where each of the relative phases ϕ_{21}, ϕ_{31}, and ϕ_{41} is changed in three equidistant steps between 0 and 2π. Here, $L = 3$ cycles the relative phase ϕ_{21} and selects

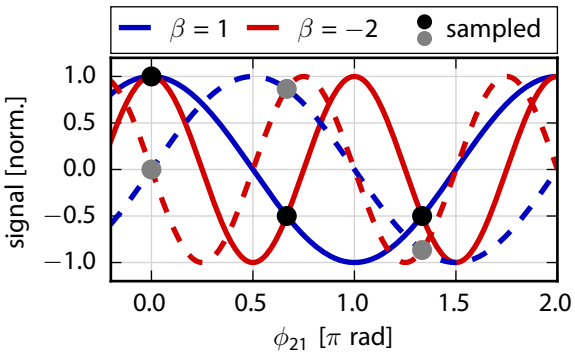

Figure 2.8: Aliased contributions in phase cycling. Real (solid lines) and imaginary part (dashed lines) as a function of the relative phase ϕ_{21} for $\beta = 1$ (blue) and the aliased contribution $\beta = -2$ (red). The relative phase is sampled in three steps (real part: black dots, imaginary part: gray dots). Both signals cannot be discriminated with this sampling scheme.

all contributions with $\beta = 1$ or $\beta = -2$ due to aliasing, reducing the 55 possible contributions that fulfill Eq. (2.2.4) to 17. The second phase-cycling step with $M = 3$ cycles ϕ_{31} and selects 7 remaining contributions from this subset that fulfill $\beta = 1$ or $\beta = -2$ *and* $\gamma = 1$ or $\gamma = -2$. The last phase-cycling step for ϕ_{41} with $N = 3$ reduces this to all contributions with the additional condition that $\delta = -1$ or $\delta = 2$. In combination, that allows to select uniquely the rephasing contribution without aliasing [59].

Using this 27-step phase-cycling scheme, all contributions with $|\beta|, |\gamma|, |\delta| = 1$ can be isolated in a four-pulse experiment, including the rephasing and non-rephasing contribution and double-quantum coherence signals. Other phase-cycling schemes, especially for three- and two-pulse sequences, are discussed in Refs. [59, 120, 121].

3 | Experimental Approach of this Work

Both experimental techniques developed in this work, "Rapid-scan coherent 2D fluorescence spectroscopy" (Chap. 4) and "Molecular-beam coherent 2D electronic spectroscopy" (Chap. 6), only differ in the detection method and share major parts of the optical setup as well as the same software and electronic circuitry. The essential experimental components of both setups are described in detail in this chapter and the full composition of the respective setup will then be explained briefly in later chapters where the results of both experiments are discussed in detail.

Section 3.1 presents the laser sources employed in this work and explains the optical setups to generate broadband tunable excitation pulses at the desired wavelength. This is followed by a detailed treatment of the pulse shaper and the procedures for pulse compression and shaper calibration (Sect. 3.2). Finally, Sect. 3.3 of this chapter introduces the setup to detect fluorescence of liquid-phase samples and presents the details of the time-of-flight mass spectrometer, which is used to investigate gaseous samples in molecular beams.

3.1 Laser Sources

The time-resolved observation of photophysical phenomena, such as quantum coherences, or photochemical reactions like dissociation or isomerization requires specific tools to capture snapshots of the sample with femtosecond time resolution. This implies pulsed lasers with large spectral bandwidths and the ability to tune the center frequency over a wide spectral range, depending on the system under investigation. A large bandwidth not only supports short laser pulses, but also provides a larger spectral window for observation, covering multiple transitions simultaneously and hence helps to unravel, e.g., energy transport over multiple

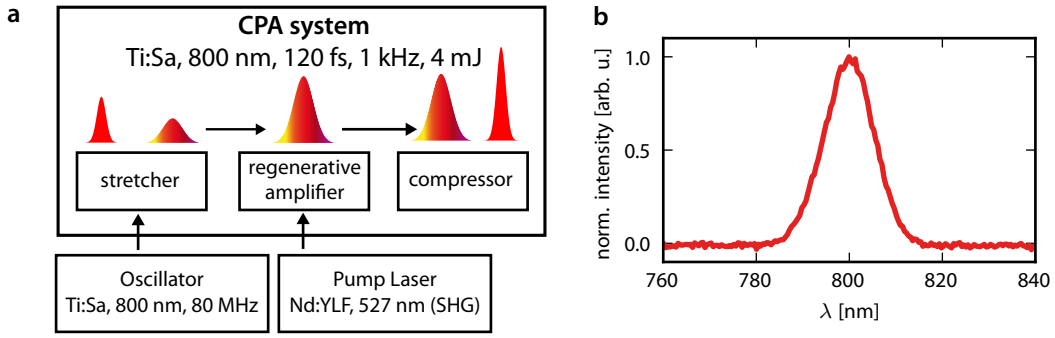

Figure 3.1: Laser system. (a) Schematic layout of the chirped-pulse amplification (CPA) system with a stretcher-compressor combination and a regenerative amplifier delivering pulses at 800 nm center wavelength with 1 kHz repetition rate. (b) Output spectrum of the laser amplifier.

different chromophores.

In this section, the laser system used in this work and devices to cover other spectral regions than provided by the laser output are introduced.

3.1.1 Regenerative Amplifier

The laser system consists of a commercially available Titanium-Sapphire (Ti:Sa) regenerative amplifier (Spitfire Pro, Spectra Physics) using *chirped-pulse amplification* (CPA) [98] and operating at a center wavelength of 800 nm and a repetition rate of 1 kHz [Fig. 3.1 (a)].

The seed pulses for amplification are provided by a 800 nm mode-locked Ti:Sa oscillator with a repetition rate of 80 MHz (MaiTai, Spectra Physics) that is pumped by a frequency-doubled mode-locked Neodymium-doped Yttrium Vanadate (Nd:YVO_4) solid-state laser at 532 nm.

The seed pulses pass an acousto-optical programmable dispersive filter (AOPDF) (Dazzler, Fastlite, see also Chap. 3.2.1) and a grating stretcher before entering the amplifier cavity via a Pockels cell and a thin-film polarizer.

The task of the AOPDF is to modify the ideally Gaussian seed spectrum prior to amplification by shaping a dip at the center frequency. This compensates for gain narrowing originating from an irregular spectral gain profile and should lead to an unchanged spectral bandwidth of the amplified output pulses [122].

The amplifier Ti:Sa crystal is pumped at 527 nm by the frequency-doubled output of a Neodymium-doped Yttrium Lithium Fluoride (Nd:YLF) Q-switched laser (Empower, Spectra Physics), providing the energy for amplification of the selected seed pulse. After several round trips inside the cavity, a second Pockels

cell is used to exit the amplified pulse that is subsequently compressed by a grating compressor.

In the configuration used in this work the laser delivers pulse energies of 4 mJ at a pulse duration of 120 fs and a spectral bandwidth of 15 nm FWHM [Fig. 3.1 (b)]. Two 50:50 beam splitters are used at the amplifier output to distribute the pulse energy and guide the beams to various experiments in the laboratory.

3.1.2 Non-Collinear Optical Parametric Amplifier

Tunability of the excitation spectrum is achieved by frequency conversion of the fundamental spectrum in a commercial two-stage *non-collinear optical parametric amplifier* (NOPA) (TOPAS White, Light Conversion).

Parametric amplification [98, 99, 123, 124] is achieved by overlapping a weak seed beam spatio-temporally with an intense pump beam in a nonlinear β-barium borate (BBO) crystal (NC, Figure 3.2). The seed is derived from a white-light continuum [98] that is generated in a sapphire plate from about 2% of the 1 mJ, 800 nm input beam, which is transmitted at the input beam splitter (BS1). The seed beam passes a double-pass grating stretcher in order to introduce a negative group-delay dispersion (GDD) [98, 99] and is focussed into the nonlinear crystal. The 400 nm pump beam with an energy of approximately 450 μJ is derived from the fundamental via second-harmonic generation (SHG) [98, 99] in a BBO crystal and separated by a beam splitter (BS 2) into two parts. The first pump beam crosses the seed beam inside the nonlinear crystal in a non-collinear geometry at an angle of 6° [125], ensuring phase-matching and thus amplification over a broad spectral range [123, 124]. Spectral tunability of this first amplification stage is achieved by controlling the angle of the nonlinear crystal and the arrival time of the pump pulse via delay 1.

The amplified signal ($\approx$ 600 nJ pulse energy) passes the nonlinear crystal a second time at a different position and is there overlapped with the second pump beam under the same non-collinearity angle, leading to further amplification. Delay 2 is used to optimize the temporal overlap and thus the output power. After the second stage, pulse energies up to 70 μJ are achieved with center wavelengths from $500 - 750$ nm [Fig. 3.2 (b)] and $850 - 1000$ nm and bandwidths of up to 45 nm FWHM, providing the possibility to compress the output pulses to a pulse duration of $15 - 30$ fs.

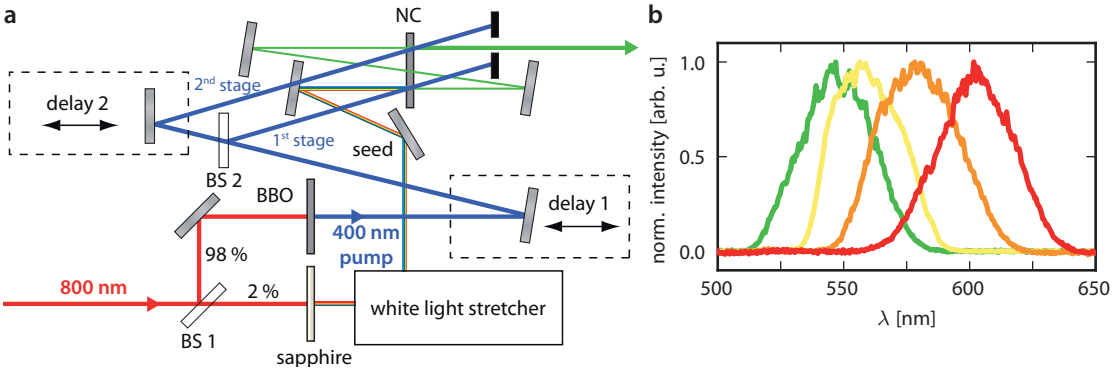

Figure 3.2: TOPAS White. (a) Schematic layout of the TOPAS White beam paths. A stretched white-light seed beam is amplified in a double stage configuration via parametric conversion. The pump energy is delivered by the second harmonic of the 800 nm fundamental. Wavelength tuning is achieved by adjusting the delay between the first pump pulse and the white-light seed (delay 1). Pulse energies of up to 70 μJ can be achieved. (b) Exemplary output spectra in the visible range. The spectral bandwidth enables compressed pulses of $15 - 30$ fs pulse duration.

3.1.3 Third-Harmonic Generation

Laser pulses in the UV spectral region are obtained from a cascaded process comprising second-harmonic generation and sum-frequency mixing in a modified commercial setup (Super Tripler, CSK Optronics, Fig. 3.3). The 1 mJ, 800 nm fundamental beam obtained from the beam splitters at the amplifier output passes a half-wave plate at the input of the third-harmonic generation setup to rotate the polarization parallel ("p") to the optical breadboard. Subsequently, a telescope is used to reduce the beam diameter. The second harmonic of the 800 nm fundamental is generated via a type-I process [98] in a 100 μm BBO crystal, with the optical axis and the crystal surface enclosing an angle of $\theta = 29.3°$. The fundamental and the second harmonic are spatially separated using a dichroic mirror (DM). A half-wave plate in the transmitted 800 nm beam path rotates its polarization perpendicular to the optical table (denoted with "s"). It is thus parallel to the 400 nm polarization and suited for subsequent mixing in a type-I 100 μm BBO crystal ($\theta = 44.3°$) and the generation of the third harmonic via sum-frequency generation (SFG) [98, 99] in a collinear geometry. Several 267 nm high-reflecting mirrors in the following beam path spectrally filter the 267 nm signal from the 800 nm and 400 nm pump beams.

The setup delivers a pulse energy of up to 20 μJ and a pulse duration of 120 fs

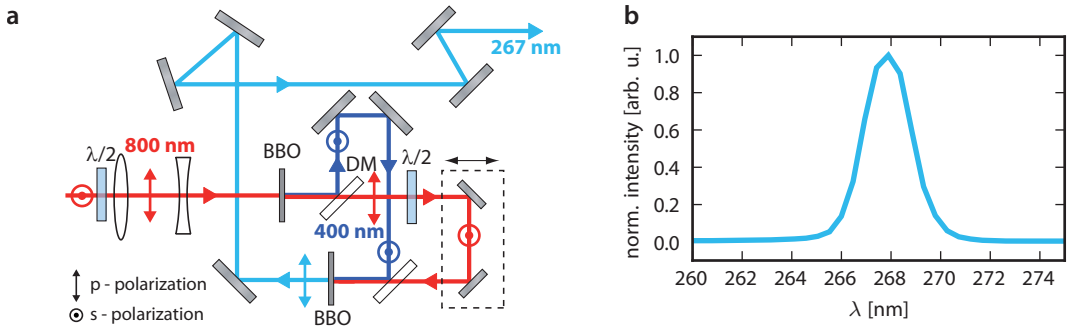

Figure 3.3: Third-harmonic generation (THG). (a) Schematic layout of the THG beam paths. The 800 nm fundamental is frequency-doubled in a BBO crystal. The second harmonic is subsequently mixed with the remaining fundamental in a second BBO crystal, generating the third harmonic at 267 nm via sum-frequency generation. This signal is spectrally filtered by several high-reflecting mirrors in the following beam paths. (b) Output spectrum centered at 267 nm. Pulse energies are controlled by attenuating the 800 nm input beam. Energies of up to 20 μJ are achieved.

with a spectral bandwidth of 2 nm FWHM (Fig. 3.3). Intensities are controlled using a neutral-density filter wheel in the fundamental beam path.

3.2 Femtosecond Pulse Shaping

Femtosecond pulse shaping is performed in general by modifying the spectral phase and amplitude for a given polarization of the electromagnetic field via a programmable dispersive medium. This can be realized in several ways that have been covered in detail by various review articles [112, 126–129]. The control over the electric field can be used, among others, for pulse characterization and compression [129, 130], quantum control experiments [46, 131–135] or generation of phase-coherent multipulse sequences for spectroscopy as in this work. In order to reduce the influence of experimental noise and realize rapid data acquisition, variation of pulse parameters with the 1 kHz repetition rate of the laser is desired. In contrast to pulse shapers employing liquid-crystal displays (LCDs), this requirement can be fulfilled by devices based on acousto-optical interaction. Hence, a custom-designed acousto-optical dispersive filter is used in this work (Dazzler WR510, Fastlite). In the following, the operation principle of the pulse shaper and necessary calibration steps as well as its limitations are discussed. Furthermore, the acquisition electronics to realize shot-to-shot streaming of pulse shapes

is presented.

3.2.1 Pulse Shaping with an Acousto-Optical Dispersive Filter

Principle of Operation

An acousto-optical dispersive filter (AOPDF) relies on the interaction of an acoustic pulse propagating quasi-collinearly with an input laser pulse in a birefringent crystal [136]. The acoustic pulse generates a spatial variation of the dielectric constant ϵ along the propagation in positive z direction. The variation can be regarded as stationary at the time of acousto-optic interaction due to the difference in propagation speed between acoustic and optical pulse. The acoustic pulse leads to stress-induced off-diagonal elements in the dielectric tensor of the material, which couples the input electric field polarized along the fast crystal axis with the output electric field polarized along the slow crystal axis [122, 137] [Fig. 3.4 (a)]. For efficient energy transfer from the input polarization to the orthogonal output polarization, phase matching must be fulfilled for each frequency component according to [136]

$$\omega_2 = \omega_1 + \Omega \qquad \mathbf{k}_2 = \mathbf{k}_1 + \mathbf{K}\,, \tag{3.2.1}$$

with $\omega_{1,2}$ as the optical frequencies of the input and output laser pulses and $\mathbf{k}_{1,2}$ as their corresponding wavevectors. Furthermore, Ω denotes the radio frequency and $\mathbf{K}$ the wavevector of the acoustic pulse.

Due to the phase-matched acoustic interaction, the shaped output laser pulse is diffracted enclosing a walk-off angle of 1° with the input optical axis [Fig. 3.4 (b)]. This leads to space-time coupling effects and spatial chirp of the shaped beam that can be compensated by choosing an appropriate focusing geometry [138, 139].

It was shown [137] that given small acoustic amplitudes S_{ac}, the output field E_{out} can be directly calculated from the input field E_{in} via a convolution (time domain) or direct multiplication (frequency domain)

$$\begin{aligned} E_{\mathrm{out}}(t) &= E_{\mathrm{in}}(t) \otimes S_{\mathrm{ac}}\left(t/\alpha\right)\,, \\ E_{\mathrm{out}}(\omega) &= E_{\mathrm{in}}(\omega) S_{\mathrm{ac}}(\alpha\omega)\,. \end{aligned} \tag{3.2.2}$$

Accordingly, the properties of the output field can be controlled by shaping the corresponding frequencies of the acoustic field. Here, α denotes the ratio between the optical frequency and the required acoustic frequency. For the device used in this work, $\alpha = \mathcal{O}\left(10^{-7}\right)$, which means that the required acoustic frequencies are

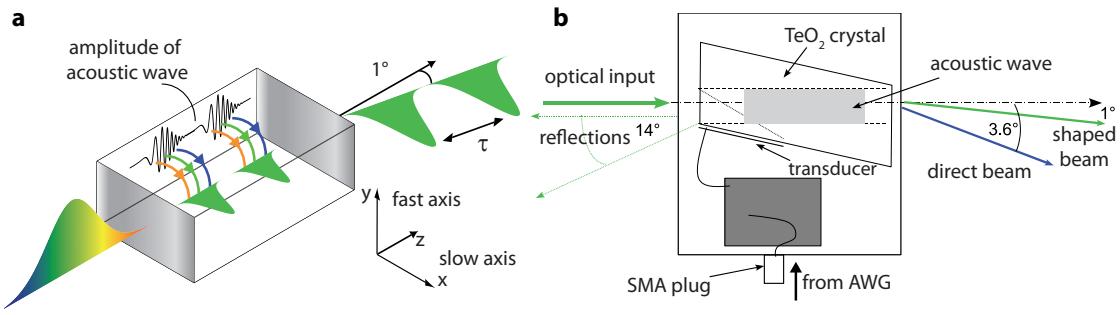

Figure 3.4: Dazzler principle of operation. (a) Schematic view of pulse compression and generation of multiple pulses. A chirped acoustic pulse (black) leads to different phase-matching positions for different frequency components (colored arrows). The different index of refraction for fast and slow axis can be employed to introduce a delay among the frequency components and thus to compensate an initial optical chirp. Multiple pulses (green) can be generated by launching the same acoustic pulse multiple times with variable delay, leading to a delay τ between the output pulses. (b) Top view of TeO_2 crystal. The laser propagates from left to right. An acoustic wave is generated with a transducer attached to the crystal that is supplied by a radio-frequency signal (MHz range) produced by an arbitrary waveform generator (AWG, not shown). The shaped pulse exits the crystal enclosing an angle of 1° with the optical axis. Figure adapted and modified from [140].

in the MHz range and can be readily generated via arbitrary waveform generators and a piezoelectric transducer attached to the crystal [140] [Fig. 3.4 (b)].

If the acoustic pulse has a temporally varying frequency (chirp), the different spectral components of the input laser pulse are diffracted to the orthogonal polarization at different positions $z(\omega)$. Due to the difference in the index of refraction between fast and slow axis (here $\delta n \approx 0.4$ [140]), each optical frequency therefore encounters a different delay inside the crystal, enabling laser pulse compression by introducing negative chirp with the pulse shaper. Additionally, the optical pulse can be delayed in time by controlling the interaction position inside the crystal, as the the acoustic wave can be launched with an adjustable time delay with respect to the input laser pulse. This correlates the optical delay with the interaction position and results in a maximum achievable delay determined by the crystal length (shaping window). The available scanning range is further limited by the amount of chirp that needs to be compensated and therefore by the spatial spreading of the acoustic pulse.

Multiple pulses can be realized by adding several (delayed) acoustic pulses. For example [Fig. 3.4 (a)], two negatively chirped acoustic pulses (black) interacting with a positively chirped input pulse inside the nonlinear crystal lead to a com-

pressed pulse pair (green) at the output with orthogonal polarization relative to the input.

The "Dazzler" used in this work comprises a 25 mm TeO_2 crystal that provides a shaping window of up to 8 ps [140]. As the propagation of the sonic wave over the full crystal length takes about 30 μs, this Dazzler has a maximum update rate of the acoustic pulse shape of a few kHz, typically limiting its usage to kHz repetition-rate laser systems. However, other applications have been realized where the Dazzler is used in combination with MHz repetition-rate laser systems, realizing a rapid-scan delay line by shaping consecutive optical pulses with the same propagating acoustic pulse at slightly different crystal positions [141–143]. Furthermore, polarization shaping with two Dazzlers was demonstrated by splitting two perpendicularly polarized pulses in an interferometer and shaping them individually before recombination [144, 145].

Increasing the Shaping Window

The TeO_2 crystal itself introduces positive group-delay dispersion on the input laser pulse that can either be compensated using the pulse shaper with an appropriate shape of the acoustic pulse or by introducing negative group-delay dispersion with external means like a prism compressor [98].

As the first option significantly reduces the available shaping window to less than 1 ps (depending on the input bandwidth) by increasing the spatial spreading of the acoustic pulse, a single-prism compressor [146] is used in the beam path before the pulse shaper to account in part for the dispersion introduced by the crystal. Thereby, the shaping window can be increased and is typically 3 ps to 4 ps in the experiment. The single-prism compressor [Fig. 3.5 (a)] comprises a SF10 prism that is passed four times by the laser beam in a folded geometry [Fig. 3.5 (b)], which is realized with a retroreflector and a folding mirror. This leads to a compact design and a simple alignment procedure as wavelength tuning is achieved by simply rotating the prism. The retroreflector is positioned at a distance of 200 mm to the prism tip and used for coarse tuning of the group-delay dispersion. Fine tuning is achieved by changing the amount of glass passed by the laser pulse via the position of the prism.

A group-delay dispersion (GDD) of more than $-10 \cdot 10^3$ fs^2 can be introduced, however at the cost of generating large amounts of third-order (TOD) and fourth-order dispersion (FOD) that need to be removed by the pulse shaper. The higher dispersion orders also decrease the available shaping window, but still moderately compared to a large value of (second order) group-delay dispersion. Figure 3.5 (c)

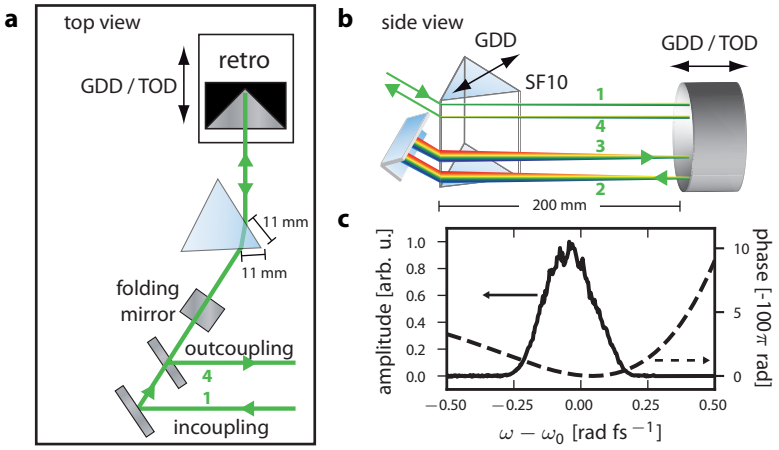

Figure 3.5: Single prism compressor. (a) Top view showing compressor assembly with the positions of folding mirror, prism, and retro reflector. The incoming beam passes the prism about 11 mm inside the prism tip, the reflected and dispersed beam at a distance of about 11 mm. More than $-10 \cdot 10^3$ fs^2 of GDD are introduced in this configuration. (b) Side view of folded beam paths. The distance of the prism tip to the retroreflector is about 200 mm. GDD is controlled by adjusting the position of the prism and the retroreflector, respectively. (c) Spectral phase introduced by the compressor in this configuration for a spectrum with a center wavelength of 540 nm (28 nm FWHM), calculated with "Lab2" [147].

shows the calculated phase (dashed line) that is introduced by the compressor to a laser spectrum centered at 540 nm (solid line) for the given geometry, corresponding to dispersion values of $-13.2 \cdot 10^3$ fs^2 (GDD), $-59.1 \cdot 10^3$ fs^3 (TOD), and $-104.6 \cdot 10^3$ fs^4 (FOD). Calculation was performed using "Lab2" [147], a LabView [148] add-on to simulate ultrafast optics.

Higher-order dispersion increases significantly for large bandwidth laser sources based on spectral broadening in atomic gas-filled hollow core fibers [149, 150], which have become increasingly popular in 2D electronic spectroscopy [151–154]. In this case, the use of a combined grating-prism (grism) compressor [155–157] is advantageous, which has been demonstrated recently in combination with a Dazzler [152].

3.2.2 Dazzler Calibration Procedures

In the experiments performed in this work the pulse shaper is used to generate more than 10^5 different pulse shapes with varying time delays and amplitudes, covering the full dynamic range of acoustic pulse powers and a large temporal shaping

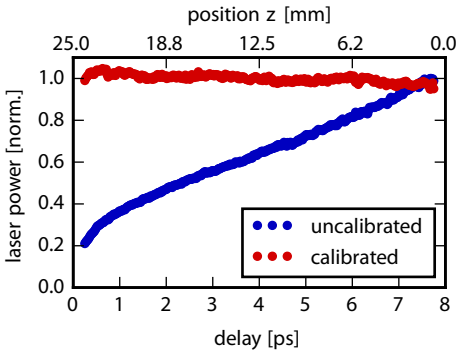

Figure 3.6: Position dependence of shaping efficiency. Local shaping efficiency as a function of acousto-optic interaction position z and pulse delay, respectively, inside the Dazzler crystal measured using a short acoustic pulse. Non-uniform behavior is observed before calibration (blue dots). After calibration, a uniform shaping efficiency is achieved (red dots).

window of the Dazzler crystal. The linear relation between acoustic amplitude and shaped optical power [Eq. (3.2.2)] only holds for small acoustic amplitudes and becomes nonlinear at large amplitudes and hence at large shaping efficiencies. For correct assessment of the acquired data, any artifact or nonlinearity introduced by the pulse shaper needs to be ruled out. Besides the regular alignment procedure and frequency calibration as explained in the Dazzler manual [140], two major calibration steps are mandatory before the pulse shaper is ready for use in a nonlinear experiment. They are explained in the following two paragraphs.

Uniformity of Shaping Efficiency

A constant shaping efficiency $\eta = E_{\text{in}}/E_{\text{out}}$ over the full crystal length needs to be established, ensuring a constant amplitude of the output electric field for all acousto-optic interaction positions and hence delays covered in the experiment.

A position-dependent shaping efficiency $\eta(z)$ arises, e.g., by the divergence of the input laser beam, an inhomogeneous beam profile, or by damping of the acoustic pulse along the direction of propagation. The effect on the local shaping efficiency can be measured using a short acoustic pulse that contains only a small amount of group-delay dispersion (-100 fs^2 GDD). The local diffraction efficiency $\eta(z)$ for this acoustic pulse is recorded by scanning the interaction position z via the optical pulse delay from the rear end of the crystal (0 ps delay) to the front end (8 ps delay) as shown in Fig. 3.6. The measured values without calibration (blue line) can be supplied as a local correction factor to the software accompanying the commercial pulse shaper. The software scales the acoustic amplitude accordingly for different positions, ensuring a constant shaping efficiency $\eta(z) = \eta$ (red line) over the full delay range.

Controlling the Acousto-Optic Nonlinearity

The second calibration step handles the intrinsic nonlinearity of the acousto-optic interaction at large acoustic powers that leads to a sub-linear scaling of the shaped output laser power as a function of the applied acoustic power, denoted by $\mathcal{A}_0$ [Fig. 3.7 (a)]. Deviations of the measured values (red dots) from the expected value (linear extrapolation, blue line) reach up to 40%. Data have been normalized to the maximum of the expected value.

Before discussing the consequences of this nonlinearity for experiments using multiple pulses and how it can be compensated, a short introduction into the basic operation principle of the Dazzler software as supplied by the manufacturer shall be given [140]. In the language of the Dazzler, a laser pulse is defined as a waveform that contains information about the spectral amplitude (amplitude scaling, center wavelength, spectral width, shape) and the spectral phase (absolute delay and nonlinear phase terms). Generally, a waveform can be normalized to a "constant-gain" reference waveform defined by the user. When this reference is supplied to the software, the acoustic power of the applied waveform is referenced to the acoustic power of the constant-gain waveform. That means that the acoustic power (and ideally the optical power of the shaped laser pulse) stays constant when only phase controls are changed, which allows, e.g., to study the influence of the nonlinear phase on the pulse duration by monitoring the second-harmonic signal. In sequences employing multiple pulses the spectral amplitude is shaped as well. In this case, the constant-gain option ensures that the acoustic power for the shaped laser pulses scales with respect to the reference as expected from calculating their acoustic waves.

Operating the Dazzler at small acoustic powers with $\mathcal{A}_0 < 5\%$ [linear regime, Fig. 3.7 (a)]), the constant-gain referencing of the acoustic amplitude linearly translates into an appropriate scaling of the diffraction efficiency and therefore into the scaling of the shaped output laser pulse. However, for large values of $\mathcal{A}_0$, the transfer from the applied acoustic power to the shaped optical power is nonlinear, leading to wrong output powers with respect to the reference. This imposes problems especially in multipulse experiments when high output powers and hence, a high shaping efficiency is desired. Scanning time delays and phases, a large linear dynamic range of the shaping efficiency for the different pulse shapes is needed, ranging from very small required acoustic amplitudes for (partial) destructive interference to high peak amplitudes for constructive interference when all pulses overlap in time with equal phase. In order to ensure a correct operation of the pulse shaper, a calibration procedure was developed that is explained in the

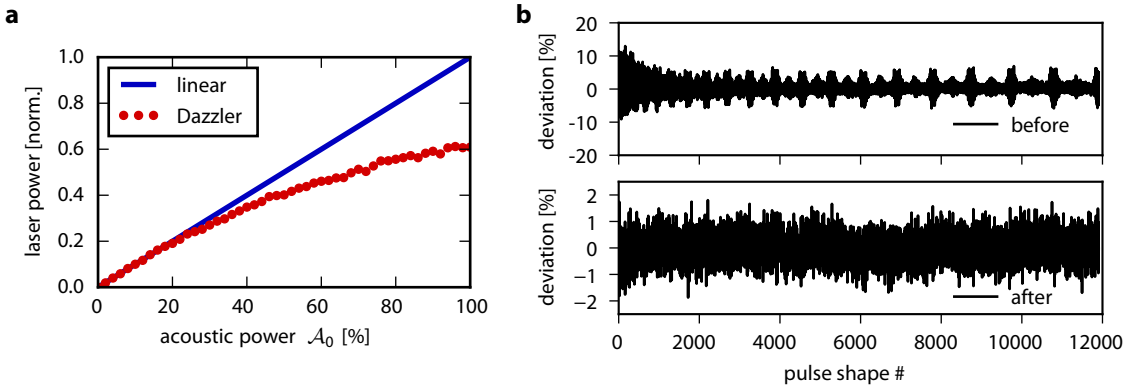

Figure 3.7: Pulse shaper nonlinearity. (a) Measured laser power (red dots) of the shaped beam as a function of applied acoustic power $\mathcal{A}_0$. For large values of $\mathcal{A}_0$, deviations of up to 40% from a linear extrapolation (blue line) are observed. (b) Relative deviation of the shaped laser power for the pulse shaper operating in the nonlinear regime with respect to a reference measurement (linear regime) for 11907 different pulse shapes (see text). The upper panel shows data acquired before and the lower diagram after the correction factors have been applied.

following.

The acousto-optic nonlinearity depends on the exact shape of the acoustic wave[2] (chirp, number of pulses, delays) and the desired maximum amplitude of the acoustic wave determined by the value of $\mathcal{A}_0$. Thus, it needs to be characterized and corrected for each pulse shape employed in the experiment. For this purpose a photodiode is placed at the sample position, measuring the shaped output laser power while stepping the pulse shaper through all pulse configurations of the experiment. This is done first for comparison in the linear regime ($\mathcal{A}_0 < 0.5\%$) yielding P_{linear} and then repeated with the value of $\mathcal{A}_0$ used in the experiment (typically $\mathcal{A}_0 = 100\%$ for maximum shaping efficiency) in order to acquire $P_{\text{nonlinear}}$. For better comparison, the same optical power at the photodiode is retained, compensating the different acoustic amplitudes via different neutral density filters in the beam path. $P_{\text{nonlinear}}(n)$ and $P_{\text{linear}}(n)$ are normalized to the measured power of the reference waveform in the respective measurement. From this measurements a correction factor $\zeta(n)$ is calculated for each individual pulse shape n via

$$\zeta(n) = \frac{P_{\text{nonlinear}}(n)}{P_{\text{linear}}(n)} \,. \tag{3.2.3}$$

Hence, the correction factor for the constant-gain reference waveform is always

[2]Herve Jousselin, Fastlite, private communication

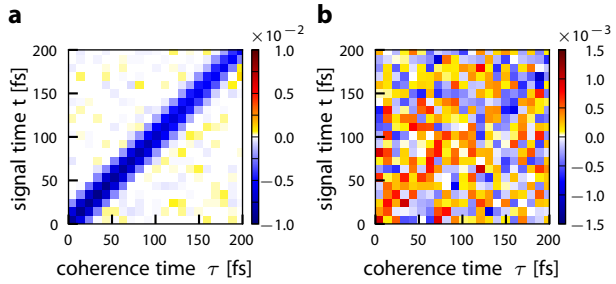

Figure 3.8: Time-domain rephasing signal contribution (real part) arising from the Dazzler nonlinearity. (a) Signal without amplitude correction. (b) Signal after amplitude correction.

unity. The obtained values are used as an individual scaling factor for the acoustic amplitude of each pulse shape in a consecutive measurement such that $\mathcal{A}_0(n) = \zeta(n)\mathcal{A}_0$.

Figure 3.7 (b) shows the distribution of correction factors $\zeta(n)$ as a relative deviation from the mean value, calculated via $\zeta(n)/\overline{\zeta(n)} - 1$, using 11907 different pulse shapes that constitute a four-pulse sequence with 21×21 coherence time delays and 27 phase-cycling steps. In the upper panel, the pulse shaper is operated without correction of the pulse shaper nonlinearity with $\mathcal{A}_0 = 100\%$, leading to deviations of the measured laser power of up to $\pm 13\%$ from the measurement in the linear regime that serves as a reference for comparison. The distribution has a standard deviation of 2.1%, with the largest deviations arising for pulse shapes on the diagonal of the time-domain parameter space ($\tau = t$). After four iterations of the calibration procedure described above, the maximum deviation decreases to $\pm 1.8\%$ with a standard deviation of 0.46% (lower panel).

The effect of the pulse-shaper nonlinearity in a 2D spectroscopy experiment can be inferred by extracting the rephasing time-domain signal from the raw photodiode data using phase cycling. For this, the raw time-domain data have been normalized to their global maximum. The scale in Fig. 3.8 can therefore be used to estimate the relative contribution of the rephasing signal to the overall data. In the case of no amplitude correction [Fig. 3.8 (a)], the signature of the remaining signal closely resembles a time-domain rephasing response function [confer Fig. 2.3 (b)] with large amplitudes on the diagonal, thus leading to an artificial peak in the rephasing 2D spectrum (not shown) that is not related to any nonlinear sample response but originates from the pulse-shaper nonlinearity. Applying amplitude correction removes the diagonal artifact [Fig. 3.8 (b)]. Small variations are still visible, however they do not contribute systematically to the rephasing signal.

3.2.3 Pulse-Shaper Assisted Laser Spectroscopy

Pulse-shaper assisted spectroscopy has the fundamental advantage of inherent phase stability, since no mechanical parts are necessary to generate multipulse sequences with varying time delays. Furthermore, a pulse shaper provides means to almost arbitrarily adjust the spectral phase of the laser pulses. In this section, it is shown how full control over the spectral phase can be used to compress pulses close to the bandwidth limit. Furthermore, efficient undersampling of coherent oscillations can be achieved by controlling the relative phases of a delayed pulse pair. This can be used to perform the measurement in a *rotating frame*.

Pulse Characterization and Compression

Determining the temporal profile of a femtosecond laser pulse requires devices with a sub-femtosecond response. This cannot be provided by conventional detection hardware like photodiodes or CCD chips. As a femtosecond laser pulse is typically the shortest event available in the laboratory, a pulse replica can be used to sample the temporal pulse profile via a nonlinear-optical interaction in frequency-resolved optical gating (FROG) [129, 158–160]. Using second-harmonic generation as the nonlinear optical process, the FROG signal is symmetric with respect to the time delay τ between both pulses and can be expressed as

$$I_{\mathrm{FROG}}^{\mathrm{SHG}}(\omega,\tau) = \left| \int_{-\infty}^{+\infty} E(t)E(t-\tau)\mathrm{e}^{\mathrm{i}\omega t}\mathrm{d}t \right|^2 . \tag{3.2.4}$$

In the experiments of this work the pulse shaper was used to generate the replica pulse and thus both pulses were arranged in collinear geometry (cFROG) [130, 161–163]. In this case, the acquired signal

$$I_{\mathrm{cFROG}}^{\mathrm{SHG}}(\omega,\tau) = \left| \int_{-\infty}^{+\infty} \left[E(t)+E(t-\tau)\right]^2 \mathrm{e}^{\mathrm{i}\omega t}\mathrm{d}t \right|^2 \tag{3.2.5}$$

contains SHG contributions of each individual pulse and the cross-term of Eq. (3.2.4). This cross-term needs to be extracted from all additional contributions of Eq. (3.2.5) via Fourier filtering [161] or phase cycling [163], yielding a SHG-FROG trace [Fig. 3.9 (a)]. The trace is reconstructed [Fig. 3.9 (b)] using the FROG pulse-retrieval algorithm [164, 165]. The reconstructed spectrum [Fig. 3.9 (c)] has a spectral FWHM of 40 nm (black line) and an almost flat spectral phase (red line). This leads to a temporal electric field with a FWHM of 17 fs [Fig. 3.9 (d)].

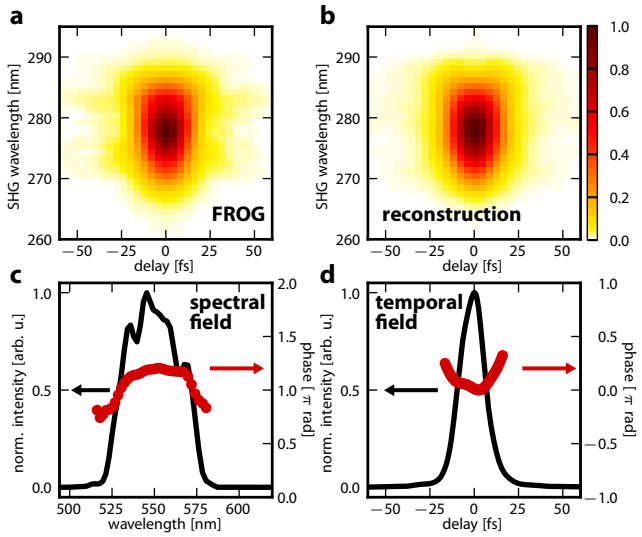

Figure 3.9: Frequency-resolved optical gating (FROG). (a) Acquired SHG-FROG trace as extracted via Fourier-filtering from pulse shaper-assisted cFROG. (b) Reconstructed FROG trace as obtained from the pulse retrieval algorithm. (c) The reconstructed spectrum (black line) has a FWHM of 40 nm and an almost flat spectral phase (red line), leading to (d) an electric field amplitude (black line) with a FWHM of 17 fs.

In the case of an uncompressed pulse the inverse of the retrieved spectral phase can be supplied to the pulse shaper as an additional phase offset for further compression. Since pulse characterization is performed at the sample position, this approach can be used to compensate any higher-order spectral phase introduced by transmissive optics in the beam path.

Rotating-Frame Acquisition

Time-resolved measurements in Fourier-transform spectroscopy sample time-domain interferences oscillating at optical frequencies and are subject to the Shannon-Nyquist criterion [166]. Hence, in order to resolve coherent oscillations and to determine their frequency, the sampling steps in the time domain need to be sufficiently small to acquire at least two samples during one optical cycle. In the visible spectral region this corresponds, e.g., to a step size smaller than 1 fs at 600 nm.

In an ideal interferometer based on a mechanical delay line, the carrier-envelope phase (CEP) of two delayed pulses in a pulse pair is identical and independent of their delay [167]. This implies a delay-dependent phase shift between the carrier waves of both pulses and thus oscillating interferences as a function of time delay [Fig. 3.10]. The same reasoning can be applied for the phase evolution of an oscillating dipole excited by the first pulse and sampled by the delayed second pulse. As the phase of the carrier wave of the second pulse shifts with respect to the phase of the oscillating dipole, destructive or constructive interference as a function of time delay lead to coherent oscillations in the observed signal.

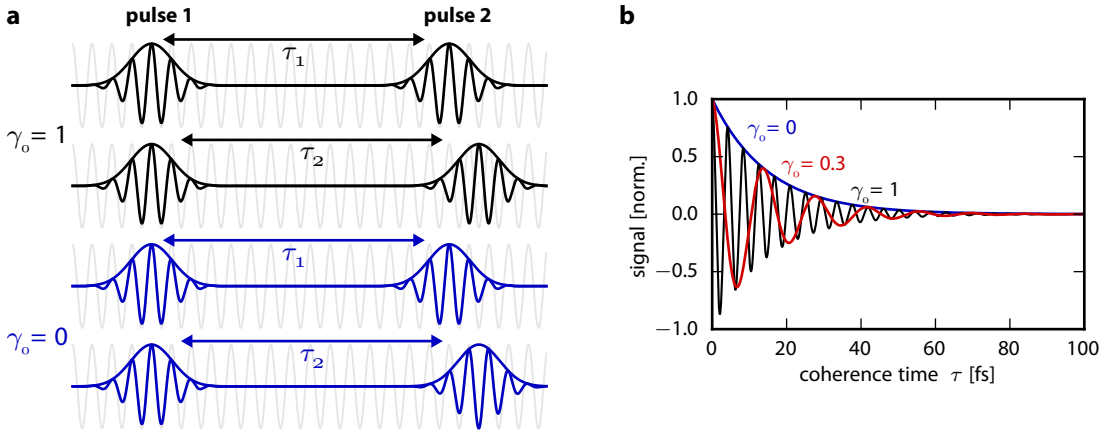

Figure 3.10: Rotating frame acquisition via phase control. (a) For a mechanical delay line or $\gamma_0 = 1$ (black pulses) the carrier-envelope phase of pulse 1 and pulse 2 is constant for all time delays, illustrated by τ_1 and τ_2. Thus, the carrier wave of the second pulse shifts with respect to the carrier wave of the first pulse (gray line). For $\gamma_0 < 1$ (here: $\gamma_0 = 0$, blue pulses) the carrier-envelope phase of the second pulse changes with delay (see text). Thus, the carrier waves of both pulses remain in phase. (b) Phase control can be used to shift coherent oscillations from the laboratory frame ($\gamma_0 = 1$, black line) to the rotating frame ($\gamma_0 = 0$, blue line) or to any value in between (red line), providing means for efficient undersampling.

The interference can be controlled and the oscillations can be shifted to an arbitrary frequency or completely removed when using a pulse shaper to generate the pulse pair. This can be realized by keeping both carrier waves in phase while shifting the time-domain carrier-envelope phase ϕ_{CEP} of the second pulse with respect to the first pulse as a function of the time delay τ between both pulses [130, 167],

$$\phi_{CEP}(\omega_0, \tau) = (1 - \gamma_0)\,\omega_0 \tau\,. \tag{3.2.6}$$

Here, ω_0 denotes the center frequency of the laser spectrum. The factor γ_0 controls the carrier-envelope phase evolution, with $\gamma_0 = 1$ resulting in no CEP shift as for a mechanical delay line [black pulses, Fig. 3.10 (a)] and thus interferences oscillating at the frequency of the transition [black line, Fig. 3.10 (b)]. This is denoted as *laboratory-frame* measurement. In contrast, for $\gamma_0 < 1$ the carrier phase shifts with respect to the envelope [blue pulses, Fig. 3.10 (a)] and the frequency of the oscillation is reduced [red line, Fig. 3.10 (b)]. For $\gamma_0 = 0$ oscillations at optical frequencies are shifted to the origin of frequency space (*rotating frame*) and thus oscillate with $\omega - \omega_0$. They are completely removed from the time-domain signal if ω_0 equals the frequency of the transition [blue line, Fig. 3.10 (b)]. A pulse shaper

can adjust γ_0 and therefore the center frequency of the rotating frame arbitrarily.

Selecting $\gamma_0 = 0$ enables the use of an increased temporal step size and thus efficient undersampling. However, oscillations arising from frequency components at the edges of the spectrum need to be considered for broadband laser spectra and the temporal step size needs to be adjusted accordingly. For example, the red edge (580 nm) of the spectrum in Fig. 3.9 (c) has a difference of 38 THz from the rotating-frame frequency (555 THz or 540 nm), corresponding to a maximum applicable rotating-frame step size of 13 fs for the given spectrum.

3.2.4 Shot-to-Shot Streaming of Pulse Shapes

The customized pulse shaper used in this work permits to change the pulse shape within two consecutive laser shots and to "stream" more than 10^5 different, predefined pulse shapes without interruption. This allows to implement rapid scanning of pulse parameters, utilizing the high degree of correlation between consecutive laser shots to reduce the influence of laboratory noise present in the frequency range up to 1 kHz [168–170]. For correct data analysis, the exact assignment between a measured data point and the applied pulse shape is crucial.

The acoustic-pulse generator module of the Dazzler pulse shaper provides several transistor-transistor logic (TTL) signals that allow synchronization of the laboratory equipment with the pulse shaper. The generator itself is triggered by the laser such that the acoustic pulse is always launched at the same time with respect to the arrival of the laser pulse at the pulse shaper[3]. Firstly, the generator module provides a 30 μs long "high" TTL trigger signal whenever an acoustic pulse is being generated (RF trigger, Fig. 3.11). Second, it also provides a streaming gate that is "high" only while shot-to-shot streaming of pulse sequences is performed. Both signals are combined in a logical "AND" operation (gating box) in order to synchronize the data acquisition with the start of the sequence, such that a subsequent 14 bit, 1 GS/s digitizer card (ADQ 14, Signal Processing Devices Sweden AB) only receives a trigger signal when it is part of a streamed sequence. In this configuration, only a predefined number of triggers corresponding to the number of pulse shapes to be streamed arrive at the digitizer card and thus enable a unique assignment of pulse shapes and acquired data. For normal operation, i.e., when

[3]There is a residual electronic jitter of 12 ns as the clock of the generator module is not synchronized to the laser in the experiments of this work. This translates into an optical jitter of $\delta = 3$ fs, i.e., the optical delay of a shaped pulse varies within 3 fs from shot to shot [140] with respect to a pulse that did not pass the pulse shaper. The delays within a pulse sequence generated by the pulse shaper are not affected.

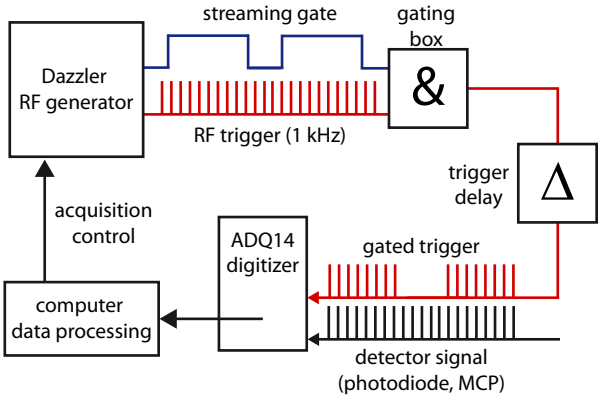

Figure 3.11: Triggering scheme for shot-to-shot streaming. The Dazzler RF generator module produces a "high" TTL signal (derived from the laser trigger, not shown) whenever an acoustic pulse is applied to crystal. This is combined with a streaming gate (see text) in order to only transmit trigger signals to the digitizer card that are part of shot-to-shot streaming sequence. If necessary the triggers can be delayed with ns precision.

the pulse shape is the same over several tens of consecutive laser shots, the gating box can simply be bypassed and the RF trigger directly connected to the digitizer.

The timing between trigger and signal can be adjusted with 1 ns precision via a digital delay generator (Stanford Research DG 535), enabling to precisely set the beginning of the temporal acquisition window for the digitizer card. This is helpful in order to avoid unnecessary occupation of digitizer memory especially with time-of-flight detection (see below), as ions arrive at the detector several microseconds after the regular laser trigger. The digitizer card can be configured such that it integrates the acquired data for every laser shot on-the-fly over multiple predefined temporal windows, decreasing significantly the data rate of the experiment.

3.3 Applied Detection Methods

As reviewed in Chap. 2.2.2, population-based 2D electronic spectroscopy is more versatile in terms of observables compared to coherence-based approaches. In this section, the experimental approach to detect fluorescence emitted from liquid samples and cations from gaseous samples in a time-of-flight mass spectrometer is demonstrated. The detection concept of both setups as well as the required vacuum system for cation detection is explained in detail.

3.3.1 Fluorescence Detection in Liquid Samples

The experimental setup to collect fluorescence emitted from a liquid-phase sample after excitation by four collinear laser pulses comprises a cytometry-type flow cell

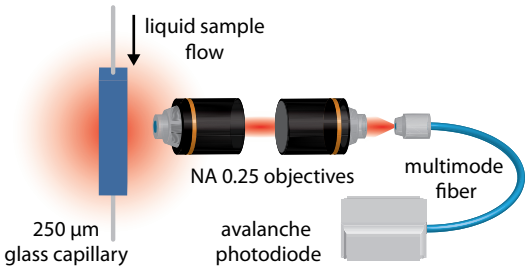

Figure 3.12: Fluorescence Detection in liquid samples. The sample is circulated through a square glass capillary. Fluorescence (red) is collected and collimated using a 0.25 NA microscope objective. A second objective of the same type couples the fluorescence into a multimode fiber that is attached to an avalanche photodiode.

with square cross section (250 μm×250 μm, 131.310-QS, Hellma) and four polished sides as the sample container (Fig. 3.12).

The sample is permanently circulated through the flow cell using a micro annular gear pump (mzr-2942-cy, HNP Mikrosysteme GmbH), ensuring an exchange of the sample for consecutive laser shots. Sample fluorescence is collected and collimated under an angle of 90° with respect to the excitation beam via a 0.25 NA microscope objective (04OAS010, CVI Melles Griot). A second objective of the same type focuses the collimated fluorescence on a 0.22 NA multimode glass fiber with a core diameter of 400 μm (QP400-2-SR, Ocean Optics) in order to guide the signal to the detector. The contribution of scattered light to the signal can be decreased by choosing the polarization of the excitation pulses horizontal with respect to the laser table, such that it points into the direction of detection. Additionally, an emission filter can be inserted between the two microscope objectives in order to block the excitation spectrum.

For shot-to-shot detection and read-out, a high-sensitivity avalanche photodiode (APD, A-Cube S500-3, Laser Components) is used, operating in the wavelength range between 400 nm and 1100 nm. For UV detection, a photomultiplier tube is employed (Hamamatsu R928). Fluorescence exceeding the detector limit can be attenuated using absorptive neutral density filters (FS-3R, Newport) if necessary. The detector output is digitized with the ADQ14 digitizer card.

Alternatively, a spectrometer (SpectraPro-2500i, Acton) equipped with a two-dimensional CCD camera (Pixis2k, Princeton Instruments) can be utilized for detection, providing the possibility to resolve the fluorescence spectrum and to realize a 2D spectrum for each emitted wavelength.

3.3.2 Ion Detection in Molecular Beams

Gas-phase experiments are conducted with a home-built reflectron-type time-of-flight mass spectrometer [171] that is composed of two parts (Fig. 3.13).

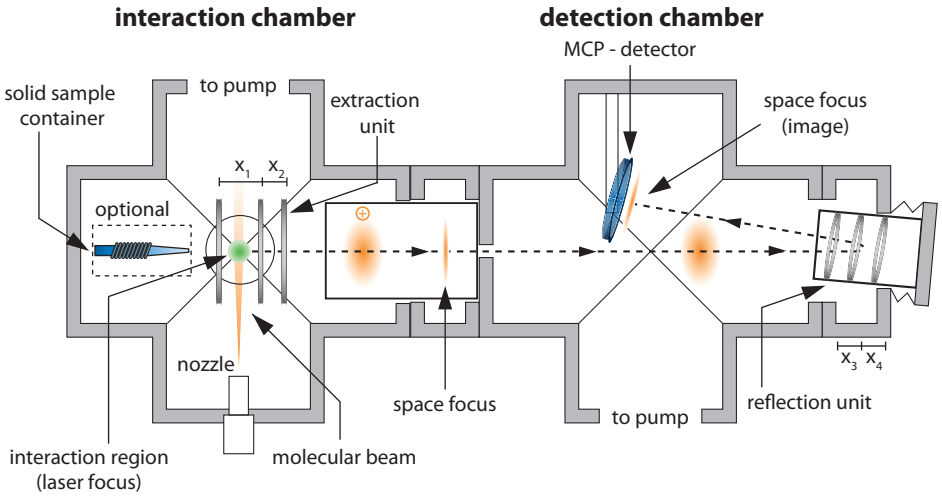

Figure 3.13: Reflectron time-of-flight mass spectrometer. The sample is prepared in the interaction chamber as an effusive molecular beam either by expansion from a gas reservoir or optionally by resistive heating from a solid sample container. The laser intersects the molecular beam under an angle of 90°. Generated ions are accelerated by electrostatic lenses (extraction unit) towards the detection chamber. Due to the difference in kinetic energy, an initial ion distribution (orange ellipse) gets compressed at the space focus and spreads again thereafter. The distribution at the space focus is imaged by an electrostatic mirror (reflection unit) to the detector position, thereby increasing mass resolution by increasing the drift time. Ion detection is achieved with a micro-channel plate detector (MCP). The drawing is not to scale. Figure adapted and modified from Ref. [175].

The interaction chamber contains a heatable nozzle from which the sample is expanded as an effusive beam and an extraction unit comprising three ring electrodes. The electrode configuration realizes a two-stage Wiley-McLaren ion gun [172, 173] that leads to improved mass resolution (here: $\frac{\Delta m}{m} \approx 2000$ at 170 amu [174]) through efficient compensation of an initial distribution of kinetic energies arising from a spatial distribution of ionization positions in the laser focus. Due to the difference in kinetic energy, the initially wide-spread diffuse cloud of ions indicated by an orange ellipse in Fig. 3.13 gets compressed and yields the shortest temporal distribution at the *space focus*, which denotes the position along the drift direction where all ions arrive almost simultaneously. After this position, the ion distribution spreads again due to the difference in kinetic energy.

The second chamber houses the ion reflection unit comprising three additional ring electrodes. They serve to increase the overall drift time and therefore the mass resolution by imaging the space focus onto a micro-channel plate (MCP) detector

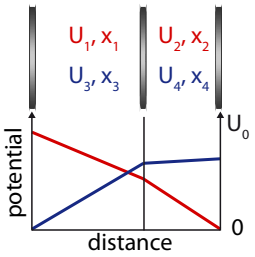

geometry [mm]	x_1	x_2	x_3	x_4
	15	14	23	50
applied potential [V]	U_1	U_2	U_3	U_4
	1099	1031	1430	520

Figure 3.14: Wiley-McLaren electrode geometry and applied potentials. The Figure on the left-hand side shows a schematic illustration of the geometry and the potential gradients. The labels (U_1,x_1) and (U_2, x_2) denote the potential difference and the gap between the extraction electrodes (red), (U_3, x_3) and (U_1, x_4) the corresponding values of the reflection electrodes (blue).

in chevron configuration (MCP MA 34/2, TOPAG Lasertechnik GmbH) [176]. The total length of the ion path is about 1220 mm [175]. The reflection unit as well as the MCP detector can be aligned for an optimized mass resolution by adjusting their tilt with respect to the time-of-flight axis.

The electrodes and the micro-channel plate are set to the required electronic potentials with precision high-voltage power supplies (NHQ 203 M, iseg Spezialelektronik GmbH). The settings as well as the electrode geometry is given in Fig. 3.14. Here, x_1 and x_2 denote the distance between the extraction electrodes, x_3 and x_4 the corresponding distances of the reflection electrodes (confer also Fig. 3.13). The potential differences across these distances are labeled accordingly. Ions arriving at the micro-channel plate detector cause an electronic discharge leading to a nanosecond voltage pulse that is extracted by a high-pass filter, amplified (Ortec 9302 Amplifier Discriminator, gain=20), and digitized using the ADQ14 digitizer card.

Each vacuum chambers is equipped with a turbomolecular pump (interaction chamber: Varian V300-HT, 300 l/s, detection chamber: Pfeiffer Vacuum HiPace 300, 260 l/s) and backed by a dry multi-stage roots pump (Pfeiffer Vacuum ACP-40G, 37 m^3/h). All pumps are capable of pumping corrosive gases when purged with an inert gas (here: N_2), reaching an ultimate pressure of 10^{-8} mbar after pumping several hours, measured with cold cathode gauges (Type 525, Varian).

4 | Rapid-Scan Coherent 2D Fluorescence Spectroscopy

Coherent 2D spectroscopy has evolved to an established method in liquid-phase spectroscopy with ongoing research in technological aspects, aiming to increase the spectral bandwidth covered within one experiment and to reduce acquisition times while simultaneously retaining a large signal-to-noise ratio (S/N).

Generally, the influence of noise on the experiment can be decreased by scanning the required experimental parameters in rapid fashion (shot-to-shot), thus exploiting the larger degree of correlation between consecutive laser shots and eliminating the influence of low-frequency noise sources in the laboratory environment [168–170]. Ideally, the measurement is performed within a single laser shot, which has been demonstrated for 2D electronic spectroscopy by using spatial encoding of one coherence time axis [177–179]. However, this approach requires delicate alignment, calibration, and thorough treatment of artifacts potentially arising from spatial distortions of the laser beam profile, imperfections in the beam geometry, or scattered light. Those effects can significantly influence the acquired 2D spectra, as studied extensively for setups based on four laser pulses that are arranged in box geometry [180–183].

"Conventional" box-geometry setups approach these challenges by employing a (shot-to-shot) chopping sequence [151, 184] in order to identify and process pump–probe contributions or remove scattered light. They further can avoid artifacts arising from phase-mismatch by using diffractive grating arrangements [151]. However, these setups so far do not utilize rapid parameter scanning as they are operated with mechanical delay lines.

Rapid scanning can be realized with pulse shapers based on acousto-optical interaction that provide an update rate of the output pulse shape in the kHz range (Chap. 3.2.1) and grant full control over the relative phases of the pulse sequence. Phase control in combination with the detection of fourth-order population-based

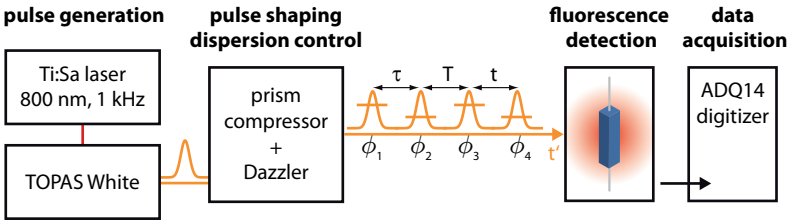

Figure 4.1: Schematic layout of the experimental setup for rapid-scan 2D fluorescence spectroscopy. The Ti:Sa laser (Chap. 3.1.1) is used to pump the NOPA (Chap. 3.1.2) that delivers output pulses with a pulse energy of up to 70 μJ. The output pulses pass a single-prism compressor for dispersion control and are shaped into a collinear four-pulse sequence using the Dazzler pulse shaper (Chap. 3.2.1). The pulse train is focused into the sample capillary. Fluorescence is detected with an avalanche photodiode (Chap. 3.3.1).

signals enables to use the simplified collinear geometry that rules out artifacts arising from an imperfect beam geometry and renders the phasing step (Ref. [82]) obsolete as the timing between all four pulses is precisely set by the pulse shaper. Additionally, scattered-light contributions can be efficiently removed using emission filters and 90° detection in fluorescence experiments and are even not present when other non-optical observables are used.

Employing a pulse shaper instead of a mechanical delay line, the single-beam, rapid-scan coherent 2D fluorescence spectroscopy setup (Fig. 4.1) developed in this work from ideas of Refs. [58, 185] is inherently phase stable, achieves high sensitivity with fluorescence detection and permits to acquire rephasing, nonrephasing and double-quantum coherence signals within one measurement.

The new technique is demonstrated in this chapter with 2D spectra of the laser dye cresyl violet, which has served in recent years as a benchmark molecule for newly developed 2D spectroscopy setups [151, 179, 184, 186]. Coherent dynamics during the population time are identified that are in agreement with literature observations. The study is published in Ref. [1]. Furthermore, preliminary 2D spectra of azulene are discussed with regard to double-quantum coherence pathways that can potentially be observed in this molecule. Due to its anomalous fluorescence behavior from the second excited state, only $\mathbf{ESA}_2$ (Chap. 2.1.3) pathways contribute to the rephasing and nonrephasing signals, leading to an opposite sign of the 2D spectrum compared to the cresyl violet data.

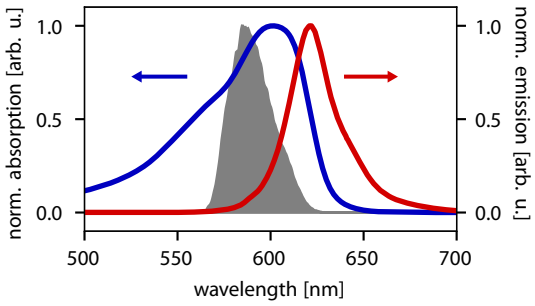

Figure 4.2: Spectral properties of cresyl violet. Absorption (blue line) and emission (red line) spectrum of cresyl violet in ethanol. The excitation spectrum (gray) has a FWHM of 25 nm and is centered at 590 nm. Adapted and modified from Ref. [1].

4.1 Quantum Beating in Cresyl Violet

4.1.1 Experimental Configuration

2D fluorescence spectra of 0.1 mM cresyl violet dissolved in ethanol are acquired by scanning the coherence times τ and t from 0 fs to 86 fs in 6 fs steps and the population time T from 0 fs to 300 fs in 10 fs steps in a rotating frame ($\gamma_0 = 0$, Chap. 3.2.3) with the Dazzler pulse shaper. A $1 \times 3 \times 3 \times 3$ phase-cycling scheme (Chap. 2.2.3) is employed in order to separate nonlinear signal contributions during data analysis. In total, $15 \times 15 \times 27 = 6075$ different pulse shapes are required, taking about 6 s for the acquisition of one 2D spectrum at a given population time. The entire data set containing 31 population time steps requires 188325 different pulse shapes that are acquired in about 3 min. The same measurement is repeated 400 times for averaging.

Cresyl violet has a broad absorption in the visible spectral region with a maximum at 594 nm that is modulated by vibronic progressions, while the emission (fluorescence) is red-shifted and peaks at 621 nm (Fig. 4.2). A pulse energy of 55 nJ when all four pulses overlap is used in the experiment, with the laser spectrum centered at 590 nm and with a FWHM of 25 nm, leading to compressed pulses of 25 fs pulse duration at the sample position.

The collinear pulse train is focused into the flow capillary using a $f = 150$ mm mirror to a focal spot size of 60 μm. Fluorescence is detected using two microscope objectives and an avalanche photodiode as described in Chap. 3.3.1.

4.1.2 Results and Discussion

The rephasing and nonrephasing signal contributions (Fig. 4.3) are extracted from the raw time-domain data (not shown) by summing the time-domain data of the

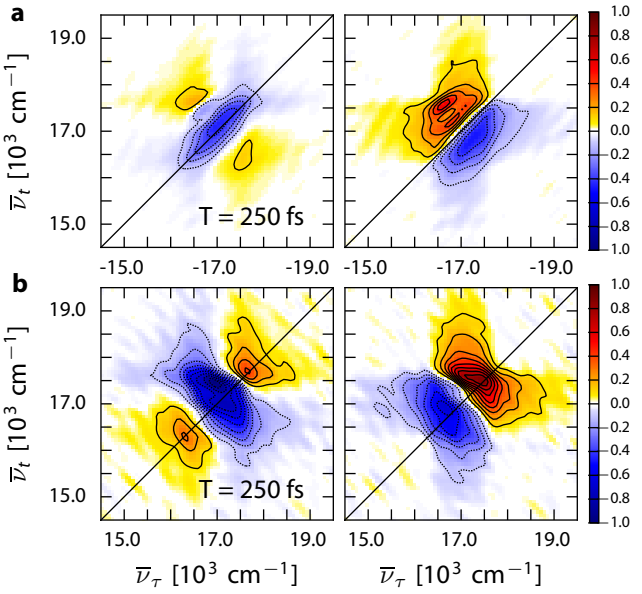

Figure 4.3: Rephasing and nonrephasing 2D spectrum of cresyl violet at $T = 250$ fs. The real part of every spectrum is shown on the left, the imaginary part on the right. The spectra are normalized to their respective maximum. Contour lines are shown at the 10 % level. (a) Rephasing 2D spectrum. (b) Nonrephasing 2D spectrum. Note the negative sign of the $\overline{\nu}_\tau$ frequency axis in the rephasing spectrum. Adapted and modified from Ref. [1].

individual phase-cycling steps with specific weights [Eq. (2.2.7)]. The weights are calculated for the rephasing contribution using $\alpha = -1$, $\beta = +1$, $\gamma = +1$, and $\delta = -1$ and for the nonrephasing contribution using $\alpha = +1$, $\beta = -1$, $\gamma = +1$, and $\delta = -1$. The time axes of the resulting two-dimensional rephasing and nonrephasing time-domain signal are extended to five times of the original length by adding zeros in order to increase the frequency resolution for the following Fourier transformation (zero-padding). Furthermore, all time-domain values where $\tau = 0$ fs or $t = 0$ fs are scaled by 0.5 prior to Fourier transformation in order to decrease their relative weight, which is justified when assuming zero signal and thus causality for $\tau < 0$ fs and $t < 0$ fs. This removes spurious background contributions and leads to a cleaner appearance of the 2D spectrum [31].

For representing the 2D spectra with laboratory frame frequency axes, the rotating-frame center frequency (here $\lambda_0 = 590$ nm, $\overline{\nu}_0 = 16949$ cm^{-1}) is added to the measured rotating-frame frequencies. The rephasing and nonrephasing signals are located in different quadrants of the two-dimensional frequency space, with the excitation frequency axis $\overline{\nu}_\tau$ of the rephasing contribution having opposite sign compared to the nonrephasing contribution and thus indicating the conjugate coherence of the density matrix during the first coherence time (confer Chap. 2.1.3).

Purely absorptive 2D spectra are obtained by taking the real part of the sum of rephasing and nonrephasing contribution, where the rephasing contribution has been mirrored at $\overline{\nu}_\tau = 0$ prior to summation so that it occurs in the positive

quadrant ($\overline{\nu}_\tau > 0$, $\overline{\nu}_t > 0$) and overlaps with the nonrephasing contribution [31]. In order to display transient dynamics of the sample, the 2D spectra at different population times have been normalized to the maximum of the 2D spectrum at $T = 0$ fs (not shown).

The absorptive 2D spectrum of cresyl violet comprises a rather broad, negative-valued feature that evolves from a slightly elongated into a rectangular shape for long waiting times [Fig. 4.4 (a)]. It consists of two diagonal and two cross peaks that overlap and can hardly be resolved [187]. Pronounced quantum beatings [upper panel, Fig. 4.4 (b)] are observed over the population time T at selected positions in the 2D spectrum [green: ($\overline{\nu}_\tau$ = 16650 cm^{-1}, $\overline{\nu}_t$ = 17500 cm^{-1}), blue ($\overline{\nu}_\tau$ = 16800 cm^{-1}, $\overline{\nu}_t$ = 17300 cm^{-1}), black: ($\overline{\nu}_\tau$ = 17050 cm^{-1}, $\overline{\nu}_\tau$ = 17650 cm^{-1})] that are attributed to vibrational coherences in the ground state ($|g_{\nu_1}\rangle \langle g_{\nu_2}|$) or in the excited state ($|e_{\nu_1}\rangle \langle e_{\nu_2}|$), respectively. The subscripts ν_i indicate the vibrational states. A 1D Fourier transformation of the oscillatory traces over the population time T [lower panel, Fig. 4.4 (b)] yields a peak at $\overline{\nu}_t$ = 538 cm^{-1} that matches well within the given frequency resolution ($\approx$ 100 cm^{-1}) to the vibrational frequency of the orthogonal aromatic stretching motion of the central ring ($\overline{\nu}$ = 595 cm^{-1})[187–189].

The spectral regions with oscillatory behavior can be generally identified by a 1D Fourier transformation of every pixel ($\overline{\nu}_\tau$, $\overline{\nu}_t$) in the absorptive 2D spectra over the population time T, yielding a 3D spectrum ($\overline{\nu}_\tau$, $\overline{\nu}_T$, $\overline{\nu}_t$). Such a 3D representation of third-order signals and its fifth-order counterparts [190–194] can be useful to unambiguously identify Liouville pathways [195–197] in order to study the origin of coherences [198, 199] or reactive modes in chemical reactions as demonstrated recently [74]. Here, a slice at $\overline{\nu}_T$ = 538 cm^{-1} unravels oscillatory dynamics for the diagonal peaks and for the crosspeak above the diagonal, which exhibits the largest oscillation amplitudes (Fig. 4.4 (c), left). The spectral slice can further be used to identify the oscillation phase at any given point in the 2D spectrum (Fig. 4.4 (c), right).

Finally, the susceptibility of the new setup to experimental noise is assessed by comparing the signal-to-noise of absorptive 2D spectra for a various number of averaging steps. Comparing the signals for various amounts of averaging reveals that the essential structures of the 2D spectrum are already apparent after averaging over five laser shots per data point [Fig. 4.5 (a)]. Taking 20 measurements, which needs about 2 min of measurement time when the population time is kept constant, the signal characteristics are almost fully established.

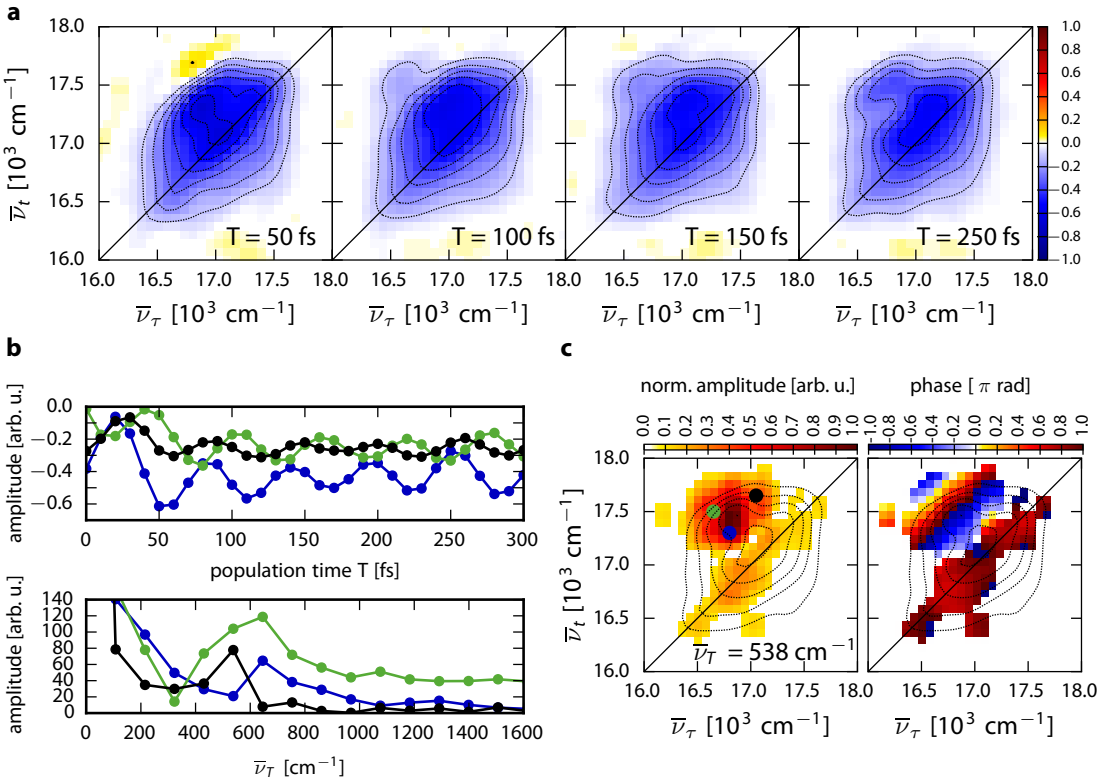

Figure 4.4: Quantum dynamics in 2D spectra of cresyl violet. (a) Absorptive 2D spectra of cresyl violet at various population times. The 2D spectra have been normalized to the maximum amplitude of the absorptive spectrum at $T = 0$ fs (not shown). The rectangular shape originates from two diagonal peaks and two crosspeaks that are not well separated due to rapid dephasing [187]. (b) Spectral amplitude as a function of population time T (upper panel) for selected regions of interest (ROI) in the absorptive 2D spectrum (see text for spectral positions). Fourier transformation (lower panel) shows a peak between 500 cm^{-1} and 600 cm^{-1}. (c) 2D spectrum of oscillation amplitudes at $\overline{\nu}_t = 538$ cm^{-1} (left) identifies a major contribution of the crosspeak to the oscillatory dynamics. The ROIs are indicated by colored dots, the dashed contours represent the absorptive 2D spectrum at $T = 300$ fs. The oscillation phase (right) varies for different positions in the 2D spectrum, as also apparent form the time-domain data. Adapted and modified from Ref. [1].

For quantitative evaluation, the signal-to-noise ratio

$$\mathrm{SNR}(N) = \frac{\left[\frac{1}{n^2}\sum_{ij}^{n}|A_{ij}(N=400)|^2\right]^{1/2}}{\left[\frac{1}{n^2}\sum_{ij}^{n}|A_{ij}(N)-A_{ij}(N=400)|^2\right]^{1/2}}, \tag{4.1.1}$$

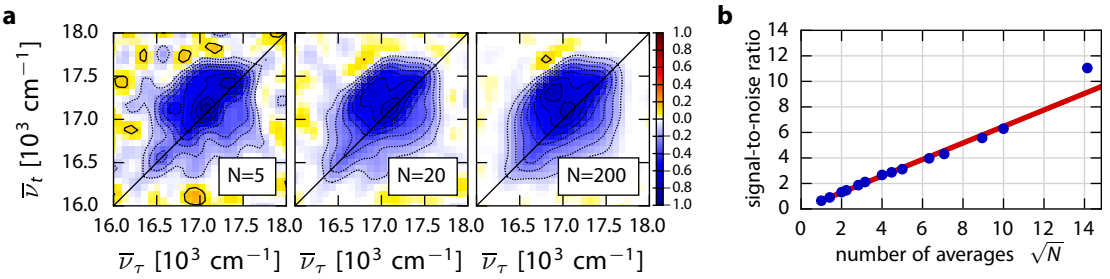

Figure 4.5: Influence of noise on experimental 2D spectra. (a) Absorptive 2D spectrum of cresyl violet at $T = 50$ fs for various amount of averaging N. Adapted and modified from Ref. [1]. (b) Signal-to-noise ratio as a function of the number of averaging steps (blue dots). The data follow closely the expected behavior for Gaussian error statistics (red line).

after N-fold averaging in a 2D spectrum containing $n \times n$ pixels with amplitude A_{ij} at pixel $(\overline{\nu}_i, \overline{\nu}_j)$ is calculated, with $A_{ij}(N = 400)$ denoting the map with most averaging that serves as a reference. Assuming randomly distributed Gaussian noise, the signal-to-noise ratio is expected to increase by $\sqrt{N}$ when increasing the number of averaged measurements N [200]. The signal-to-noise ratio [blue dots, Fig. 4.5 (b)] follows closely the expected behavior for Gaussian random noise as a function of various amount of averaging, which can be conferred from extrapolating the obtained SNR for $N = 1$ by multiplying it with $\sqrt{N}$ (red line).

4.2 Pathway Selection in Azulene via S_2 Fluorescence

Azulene is widely known for its unusual fluorescence from the second excited state S_2 that violates *Kasha's rule* [201]. It has a weak absorption band in the visible spectral region corresponding to the transition from the ground state S_0, to the first excited state S_1 and a strong absorption in the UV from the ground state into the S_2 state (Fig. 4.6). The transitions from S_0, denoted by $|g\rangle$, to S_1 ($|e\rangle$) and from S_1 to S_2 ($|f\rangle$) are approximately equal in energy, comprising a three-level system in a simplified description that permits to populate the second excited state by two-photon absorption of the excitation laser spectrum (gray).

With regard to the setup developed in this work, azulene offers additional possibilities to test the phase-cycling approach and predictions from response function theory as only Liouville pathways that end in the second excited state ($\mathbf{ESA}_2$) contribute to the detected fluorescence. Furthermore, the energy-level structure

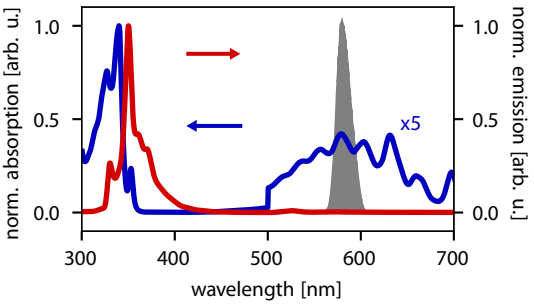

Figure 4.6: Spectral properties of azulene. Absorption (blue line) and emission (red line) spectrum of azulene in cyclohexane. The emission spectrum was recorded with an excitation wavelength of 275 nm. The excitation spectrum (gray) used in the experiment has a FWHM of 17 nm and is centered at 581 nm.

should permit to observe double-quantum coherence signals where the density matrix is in a double coherence (for instance $|f\rangle\langle g|$) during the first coherence time τ and in a single coherence ($|f\rangle\langle e|$) during the second coherence time t.

4.2.1 Experimental Configuration

In order to acquire 2D fluorescence spectra of 1 mM azulene dissolved in cyclohexane, a three pulse sequence is used where the coherence times τ and t are scanned from 0 fs to 100 fs in 2.5 fs steps at a constant population time of $T = 0$ fs. Furthermore, the measurement is conducted in a partially rotating frame ($\gamma_0 = 0.1$, Chap. 3.2.3) with a $1 \times 4 \times 4$ phase-cycling scheme [59] and is repeated 700 times for averaging. The signals of interest are extracted using a weighted sum of the raw time-domain data as discussed in the previous section.

4.2.2 Results and Discussion

Generally, the rephasing signal contains several distinct Liouville pathways (**GSB**, **SE**, **ESA**, Fig. 2.3) that cannot be discriminated with phase cycling. In 2D spectroscopy via S_1 fluorescence detection as performed in the case of cresyl violet, all of these pathways contribute to the total signal [Eq. 2.1.33]. This is different in the case of azulene, where the unusual fluorescence from the second-excited state does not allow to detect other contributions than those ending in the S_2 state. These $\mathbf{ESA}_2$ pathways contribute with opposite sign than ground-state bleach (**GSB**), stimulated emission (**SE**), or other excited-state absorption contributions ending in S_1 ($\mathbf{ESA}_1$). The negative-valued 2D spectrum of cresyl violet presented in the previous paragraph is most likely dominated by ground-state bleach or stimulated emission contributions. Since the azulene 2D spectrum arises from excited-state absorption pathways, it is expected to have the opposite sign. This

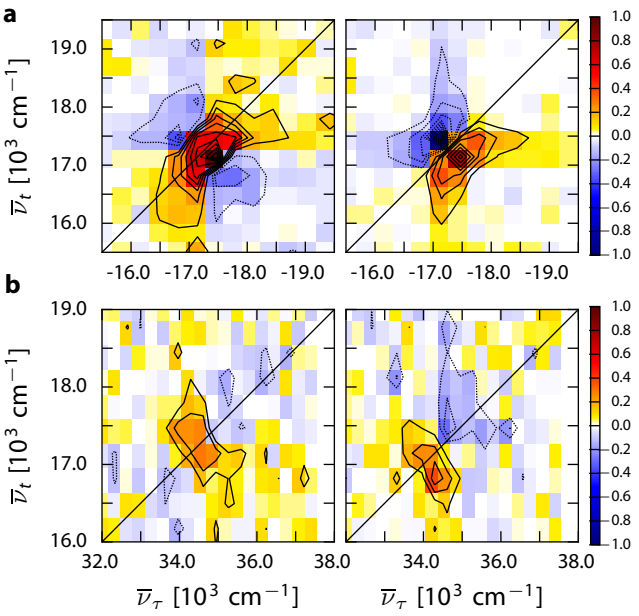

Figure 4.7: Rephasing and double-quantum coherence 2D spectrum of azulene at T = 0 fs. The real part of the 2D spectrum is shown on the left, the imaginary part on the right. Contour lines are shown at the 10 % level. (a) Rephasing 2D spectrum. (b) Double-quantum coherence 2D spectrum. The signal is located at $\overline{\nu}_\tau = 2\overline{\nu}_t$, indicating the double coherence $|f\rangle\langle g|$ during the first coherence time τ.

is the case for the positive-valued rephasing 2D spectrum [Fig. 4.7 (a)] and thus demonstrates good agreement with the prediction from response function theory.

The 16-step phase-cycling scheme used in this measurement further permits to retrieve the double-quantum coherence contribution ($\alpha = +2$, $\beta = -1$, $\gamma = -1$) where the first pulse interacts twice and prepares the $|f\rangle\langle g|$ double coherence that evolves during τ. The second pulse interacts once and prepares the $|f\rangle\langle e|$ single coherence that oscillates during t and is converted into a detectable population by the third interaction. Due to this interaction pattern, the double-quantum coherence signal is located on the $\overline{\nu}_\tau$ axis at roughly twice the frequency of the $\overline{\nu}_t$ axis [Fig. 4.7 (b)]. Signals that are shifted from $\overline{\nu}_\tau = 2\overline{\nu}_t$ reveal electronic interactions in many-electron systems and can be used to determine the electronic correlation energy [202–205], biexciton binding energies [64, 206] or to identify excited states [207]. In the case of azulene, the double-quantum coherence signal just indicates the presence of an excited state at twice the energy of the S_0-S_1 transition. This can already be inferred from the rephasing 2D spectrum and the linear absorption spectrum, but nevertheless demonstrates the capability of the new setup to acquire simultaneously multiple different signal contributions within one experiment.

4.3 Conclusion

A novel setup for rapid-scan 2D fluorescence spectroscopy based on a single-beam collinear geometry and shot-to-shot phase cycling with a pulse shaper was developed and demonstrated with 2D spectra of cresyl violet and azulene. Observations of quantum beatings in the case of cresyl violet are in good agreement with literature data [151, 179, 184, 186, 187]. The anomalous fluorescence of azulene was employed to single-out only Liouville pathways ending in S_2, which provides additional possibilities to test the outcome of the experiment against predictions from response function theory. The rapid-scanning approach enables to acquire a 2D spectrum for a given population time within 6 s, permitting to investigate photochemically unstable samples or to monitor reaction kinetics that proceed on a minute timescale in future experiments. It achieves high sensitivity via fluorescence detection, which can be employed to study dilute samples, approaching the single-molecule limit [110, 111].

5 | Optimizing Sparse Sampling for 2D Electronic Spectroscopy

Multidimensional spectroscopy in general requires multidimensional scanning of parameters such as time delays or phases as shown in the previous chapter with the implementation of rapid-scan coherent 2D fluorescence spectroscopy. While single-shot techniques have been developed as briefly reviewed in Chap. 4, the question remains whether the amount of data to be acquired can be reduced while retaining the essential information content of the resulting 2D spectrum. The acquisition concept presented in this chapter can be applied in particular for population-based approaches of 2D spectroscopy, for which the scanning protocol requires the sampling of two coherence-time axes with step sizes obeying the Shannon-Nyquist sampling theorem [166]. Especially for gaseous samples, coherences can be long-lived [103] and hence require large time delays for the two indirect dimensions. Furthermore, it may also be useful to perform an additional Fourier transform with respect to the population time T, as demonstrated in the case of cresyl violet presented in Chap. 4.1.2 and discussed therein.

Thus, in population-based multidimensional spectroscopy, the time-domain parameter space can become very large, reaching easily hundreds of thousands of different configurations. This can be efficiently reduced and hence the acquisition time can be substantially decreased by performing the measurement in a rotating frame (Chap. 3.2.3). Nevertheless, the parameter space in these experiments remains still large enough[4] to warrant searches for further data acquisition improvements.

The new acquisition concept for 2D electronic spectroscopy presented in this chapter demonstrates a possible solution to this problem and provides 2D spectra from optimally undersampled data. The findings are published in Ref. [2]. The new approach is inspired by a long history of non-uniform (under-)sampling

[4]More than 180000 different configurations in the case of cresyl violet, Chap. 4.1.

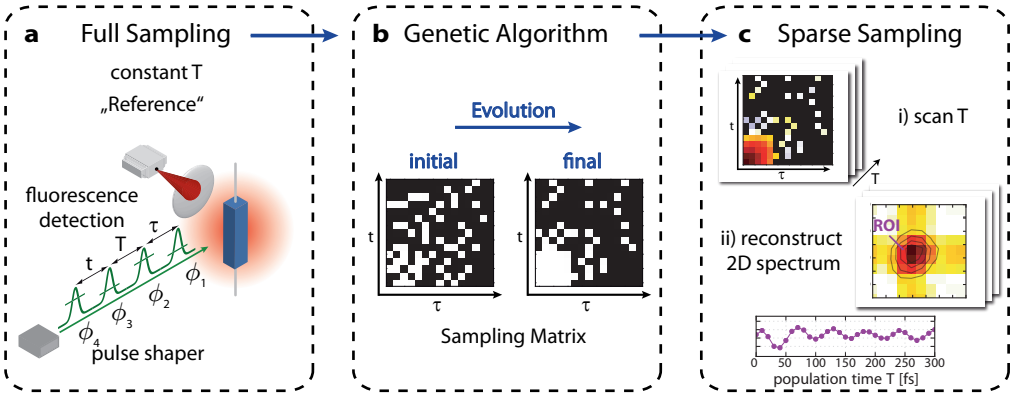

Figure 5.1: Acquisition strategy using optimized sampling. (a) Acquisition of a reference data set at a constant population time T with a full sampling of (τ, t) -parameter space. (b) Optimization of the reduced sampling matrix using the reference data set and a genetic algorithm. (c) Acquisition of 2D spectra at all other population times with the optimized sampling matrix and subsequent data reconstruction. Reproduced from Ref. [2], with the permission of AIP Publishing.

strategies in multidimensional nuclear magnetic resonance (NMR) [208, 209] and combines optimal control concepts with the novel acquisition paradigm of "compressed sensing" (CS) [210, 211]. The experimental realization is made possible using the Dazzler pulse shaper that is able to scan an arbitrary sequence of sampling points in the parameter space on a shot-to-shot basis. In contrast to setups based on mechanical delay stages, this pulse-shaper approach permits to realize solely the desired sampling points while retaining the regular duty cycle.

The general idea of the new acquisition approach is illustrated schematically in Fig. 5.1. As the first step [Fig. 5.1 (a)], a reference data set is measured at a fixed population time T using coherent 2D fluorescence spectroscopy. For this, the full time-domain sampling protocol is applied in a rotating frame and the signal contribution of interest is retrieved after phase cycling (Chap. 2.2.3).

Next, a random sampling matrix with the desired undersampling percentage is generated based on the temporal grid defined by the previous measurement. This is shown in Fig. 5.1 (b), with the sampled data points being indicated by white squares. This matrix is used to undersample the reference data set a-posteriori. A genetic algorithm is employed subsequently to optimize this reduced sampling matrix such that the reconstruction of the undersampled reference 2D spectrum agrees as well as possible with the fully sampled reference 2D spectrum.

Data reconstruction is performed based on ideas of compressed sensing and a

new, joint time-frequency von Neumann representation of 2D spectra. Both will be introduced in detail in the following paragraphs.

Finally, the optimal sampling matrix is used to measure and reconstruct 2D spectra at all other population times [Fig. 5.1 (c)]. The savings in data acquisition time arise from the reduced amount of required data for all population times other than the reference set. The approach presented in this chapter focuses in particular on rephasing and nonrephasing signals, however treatment of others such as double-quantum coherences is also conceivable.

5.1 A Short Introduction to Compressed Sensing

Initially developed in the signal processing community, compressed sensing has evolved as a new paradigm for reducing the amount of sampled data. The growing interest in compressed sensing can be attributed to its successful broad applicability in several areas of research and engineering such as imaging using a single-pixel detector [212, 213], single-shot video recording [214, 215], nuclear-magnetic resonance imaging [216], NMR spectroscopy [217, 218] and more [219].

First applications of compressed sensing to coherent 2D spectroscopy show the suitability of random undersampling to efficiently reduce the amount of time-domain data points without losing spectral information either in experiments [220] or in theoretical calculations [221]. Furthermore, it was shown that compressed-sensing reconstruction can also be used to retrieve the 2D spectrum from a uniformly sampled subset of the full signal [222]. Other non-uniform sampling protocols, such as exponentially biased, radial, or Poisson-gap sampling are successfully applied in multidimensional NMR [209, 223–225]. They benefit from a-priori assumptions on the approximate signal characteristics and use a dense sampling close to the origin of the time domain where the signal amplitudes are still large.

In the following, the sensing process of a time-domain signal will be described as a linear mapping that connects time and frequency space. This is used subsequently to introduce the basic ideas that govern the reconstruction of undersampled data.

5.1.1 Sensing as a Linear Operation

The sensing mechanism can often be described as a linear transformation, expressed by

$$\boldsymbol{y} = \boldsymbol{A} \cdot \boldsymbol{x}\,, \tag{5.1.1}$$

of a signal $\boldsymbol{x}$ via a sensing matrix $\boldsymbol{A}$ to measured values $\boldsymbol{y}$. Each line of the sensing matrix represents a sampling step and is composed of the basis functions of the measurement setup. These are, e.g., Dirac δ-functions centered at the point in time of sampling for a time-discrete measurement [226].

Generally, the sensing matrix can be more complex and map multiple signal coefficients into one measured value within one sampling step, which is denoted as signal multiplexing. This finds application, e.g., in Hadamard spectroscopy [227, 228] where light that is transmitted through a sample is dispersed and frequency selected via a gating mask with N slits, with each of the slits either opened or closed. For a given mask configuration A_i, the total transmitted light is detected with a single-pixel detector, yielding the measured value y_i. Repeating the measurement N times with different gating patterns acquires $\boldsymbol{y}$ and allows to reconstruct the spectrum $\boldsymbol{x}$ by inverting the known gating (Hadamard) matrix $\boldsymbol{A}$. This is superior in terms of signal to noise to conventional approaches using monochromators, as the contribution of a given frequency to the total signal is measured multiple times [229].

The same multiplexing principle is also intrinsic to Fourier transform spectroscopy, where the basis functions of the time-discrete measurement setup are sinusoids. Here, the frequency components of a spectrum $\boldsymbol{\omega}$ containing N coefficients all contribute with different weights determined by their amplitude and phase to the measured value t_i for a given time step. Knowledge of the N Fourier-transform basis functions expressed by the matrix $\boldsymbol{\Psi}$ allows to retrieve the spectrum $\boldsymbol{\omega}$ from N regularly-spaced time-domain measurements $\boldsymbol{t}$.

A time-discrete sensing scheme including the discrete Fourier transformation can be written as

$$\boldsymbol{t} = \boldsymbol{\Phi} \cdot \boldsymbol{\Psi} \cdot \boldsymbol{\omega}, \tag{5.1.2}$$

where the sampling times are given by the sampling matrix $\boldsymbol{\Phi}$, which is essentially the identity matrix for a uniform sampling at N points in time.

If the number of time-domain measurements M is smaller than the number N of spectral coefficients to be resolved, the problem is underdetermined and a unique inversion of Eq. (5.1.2) and thereby a determination of $\boldsymbol{\omega}$ with N components is impossible without further constraints[5]. This case of undersampling is depicted schematically in Fig. 5.2, where the sampling matrix covers only one-third of the required measurements, leading to a measured signal vector $\boldsymbol{\tau}$ that contains at a

[5]In practical applications using a Fourier transformation the perception is different: For uniform sampling, the number M of time-domain measurements yields M spectral coefficients after Fourier transformation.

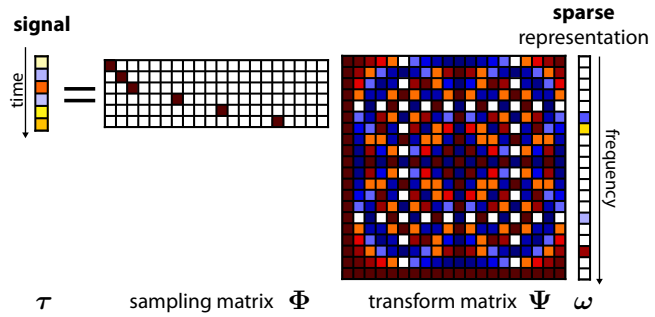

Figure 5.2: Random undersampling of a sparse signal. The spectrum $\boldsymbol{\omega}$ is mapped via the Fourier transform matrix $\boldsymbol{\Psi}$ and the time-discrete sampling matrix $\boldsymbol{\Phi}$ to the measured time-domain signal $\boldsymbol{\tau}$. The spectrum can not be recovered by simple matrix inversion, as the problem is underdetermined.

first glance not enough information to uniquely recover the spectrum $\boldsymbol{\omega}$ with the desired resolution just by matrix inversion.

However, it was shown by Donoho [211] and Candès et al. [210] that the information (here: spectrum) can be recovered with high probability from an undersampled measurement, if sampling is performed at random positions (here: in the time domain). As an additional requirement, there must exist a transform domain in which the signal has a sparse representation, i.e., in which only a small percentage of basis coefficients is non-zero. This sparsity is depicted graphically for the coefficient vector $\boldsymbol{\omega}$ in Fig. 5.2, containing only four frequencies with non-zero amplitude. Generally, sparsity can be "enforced" by mapping the signal on a suitable basis set with an additional linear transformation. For time-domain signals, this can be the Fourier transformation as shown in Eq. (5.1.2) and Fig. 5.2 or the von Neumann representation as detailed below. For imaging applications, the decomposition into wavelet bases[6] is frequently used [226].

5.1.2 Signal Reconstruction Using l_1-Minimization

Several solvers have been developed [232] that employ different strategies to solve $\boldsymbol{y} = \boldsymbol{A} \cdot \boldsymbol{x}$ from an undersampled set and aim to find the vector $\boldsymbol{x}$ with smallest number of non-zero coefficients as a unique solution to Eq. (5.1.1). This problem is often stated as

$$\min \|\boldsymbol{x}\|_0 \qquad \text{subject to} \qquad \boldsymbol{y} = \boldsymbol{A} \cdot \boldsymbol{x}, \tag{5.1.3}$$

where $\|\boldsymbol{x}\|_0$ expresses the sparsity as the l_0 pseudo-norm of a vector $\boldsymbol{x}$ and counts the number of non-zero coefficients. The matrix $\boldsymbol{A}$ is generally composed of a sensing matrix and a sparsifying transform, e.g., as in Eq. (5.1.2). Approaching

[6] The von Neumann basis is in fact composed of Gabor wavelets [230, 231].

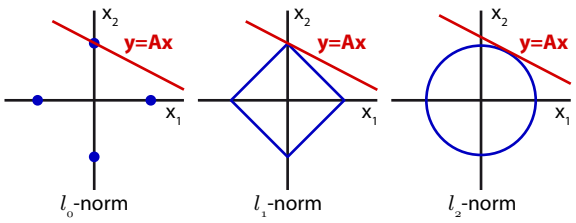

Figure 5.3: Geometry of sparse recovery. The values of the l_p-norm are shown as a function of two coefficients (blue line) together with the set of coefficients that solve Eq. (5.1.1) (red line). In contrast to l_2-minimization, the l_0 pseudo-norm and the l_1-norm permit to retrieve the sparsest solution (adapted from Refs. [219, 235]).

this problem, it turns out that minimizing $\|\boldsymbol{x}\|_0$ is computationally complex and almost intractable [232].

As an alternative, the solution can be approximated by using the l_1-norm instead of the l_0 pseudo-norm [210, 211]. The l_1-norm is defined as the sum over the absolute values of the coefficients, $\|\boldsymbol{x}\|_1 = \sum_i |x_i|$. The validity of this approach can be illustrated in two dimensions by plotting a given value of the l_p-norm ($p = 0, 1, 2$) as a function of two coefficients x_1 and x_2 (blue line, Fig. 5.3) together with hypothetical solutions that solve Eq. (5.1.1) (red line). In order to fulfill Eq. (5.1.3), the algorithm should find a solution where either x_1 or x_2 is equal to zero, i.e. where the red line intersects with either one of the axes. The solution can be found easily using the l_0 pseudo-norm. However, the shape of the l_1-norm also permits to retrieve a solution with only one non-zero coefficient and thus will yield most likely the same solution as the l_0 pseudo-norm with the additional benefit of a fast algorithm. In contrast, minimizing the l_2-norm $\|x\|_2$ does not result in the sparsest solution, as both coefficients will likely return non-zero in this case.

The acquisition approach presented in this chapter employs a Matlab [233] implementation of "two-step iterative shrinkage/thresholding" (TwIST) [234] to recover the coefficients $\boldsymbol{x}$ from an undersampled set $\boldsymbol{y}$. Technically, this is done by minimizing the objective function

$$f(\boldsymbol{x}) = \frac{1}{2}\|\boldsymbol{y} - \boldsymbol{A}\boldsymbol{x}\|_2^2 + \lambda\|\boldsymbol{x}\|_1, \tag{5.1.4}$$

where the regularization parameter λ controls the weight of the sparsity term $\|\boldsymbol{x}\|_1$ with respect to an exact reconstruction of the measured data points.

5.2 The von Neumann Representation as a Sparse Basis

Before presenting the results of compressed-sensing reconstruction in 2D electronic spectroscopy, the von Neumann (vN) basis shall be introduced as a sparsifying transform of time-domain data. The von Neumann basis – also known as the Gabor basis in signal processing [230, 231] – parameterizes a signal by two conjugate variables such as momentum and space as intended initially for quantum mechanics [236] or time and frequency as introduced later by Gabor [230] for representing arbitrary signals.

The vN representation is employed in quantum chemistry for the calculation of wavefunctions [237], energy levels [238], and quantum dynamics [231, 239–243]. Furthermore, it was shown to lead to a compact representation of ultrashort laser pulses [244–246] including their polarization state [247] and a reduced parameter space for quantum-control experiments [248, 249]. A recent paradigm shift [231, 239] makes the vN basis a promising transform domain for signal compression [250] and thus for application in compressed-sensing reconstruction algorithms.

5.2.1 The von Neumann Basis for One-Dimensional Signals

In the vN basis, a time- or frequency-domain signal with a support of N data points is transformed into a joint $\sqrt{N} \times \sqrt{N}$ time-frequency space [Fig. 5.4 (a)].

The vN basis functions $|g_{t_m w_n}\rangle$ are Gaussian pulses located at time t_m with a center frequency w_n. They can be written in the time domain as

$$g(t_m, w_n) = \left(\frac{1}{2\alpha\pi}\right)^{1/4} \exp\left[-\frac{1}{4\alpha}(t - t_m)^2 - \mathrm{i}w_n(t - t_m)\right], \tag{5.2.1}$$

wherein α is chosen as $\alpha = \frac{\sigma_t}{2\sigma_w}$ with σ_t and σ_w being the full width at half maximum in time and frequency, respectively [244]. Any time-domain signal $r(t)$ can be expanded in the vN basis by

$$|r(t)\rangle = \sum_{(m,n)} |g_{t_m w_n}\rangle\, a_{t_m w_n} = \sum_{(m,n)} \sum_{(k,l)} |g_{t_m w_n}\rangle\, S^{-1}_{(m,n),(k,l)}\, \langle g_{t_k w_l}|r(t)\rangle\,, \tag{5.2.2}$$

with the expansion coefficients $a_{t_m w_n}$ and the inverse overlap matrix element $S^{-1}_{(m,n),(k,l)}$. The latter arises due to the non-orthogonality of the vN basis, leading

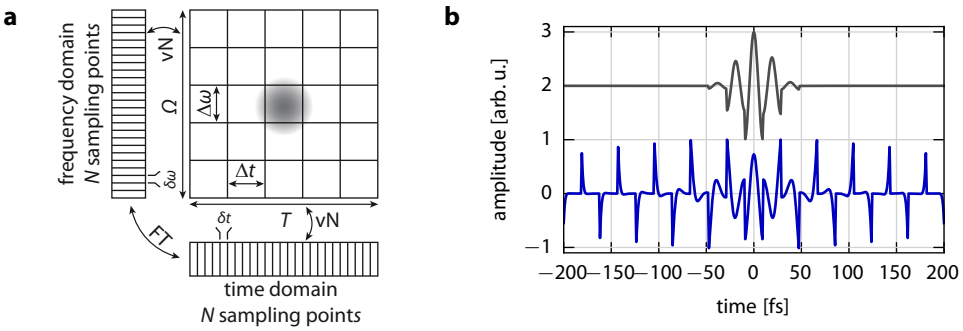

Figure 5.4: von Neumann grid and basis functions. (a) The von Neumann lattice represents a joint time-frequency space with $\sqrt{N} \times \sqrt{N}$ grid points, generated by N time- or frequency-domain points. The basis functions are Gaussian pulses centered in time at t_m and at frequency w_n, indicated schematically by the filled gray circle. They are separated by Δt along the time axis and $\Delta\omega$ along the frequency axis. The figure is adapted and modified from Ref. [251]. (b) Using bi-orthogonal exchange, the basis can be recast from non-orthogonal, local basis functions (gray) to orthogonal, non-local basis functions (blue) with localized coefficients (see text). The basis functions are offset for clarity.

to a basis-function overlap

$$S_{(m,n),(k,l)} = \langle g_{t_m w_n} | g_{t_k w_l} \rangle \tag{5.2.3}$$

for $(m,n) \neq (k,l)$ [244]. Thus, the coefficient $a_{t_m w_n}$ also has a contribution from the overlap of the basis function $|g_{t_k w_l}\rangle$ with the signal. Therefore, when a signal is represented in the vN domain using $|g_{t_m w_n}\rangle$ as the basis, many coefficients are necessary to retain the full information content. That is in contrast to the main prerequisite of the new acquisition concept, which is the existence of a sparse representation.

However, the non-locality can be removed by using a basis that is bi-orthogonal to $|g_{t_m w_n}\rangle$, as shown by Shimshovitz and Tannor [231, 239]. In the bi-orthogonal basis, the inverse overlap element becomes part of a new basis function

$$|b_{t_m w_n}\rangle = \sum_{(k,l)} |g_{t_k w_l}\rangle \, S^{-1}_{(m,n),(k,l)}, \tag{5.2.4}$$

rendering the basis function itself non-local [Fig. 5.4 (b)]. The signal can be expressed in the new basis as

$$|r(t)\rangle = \sum_{(m,n)} |b_{t_m w_n}\rangle \, \langle g_{t_m w_n} | r(t)\rangle = \sum_{(m,n)} |b_{t_m w_n}\rangle \, c_{t_m w_n}, \tag{5.2.5}$$

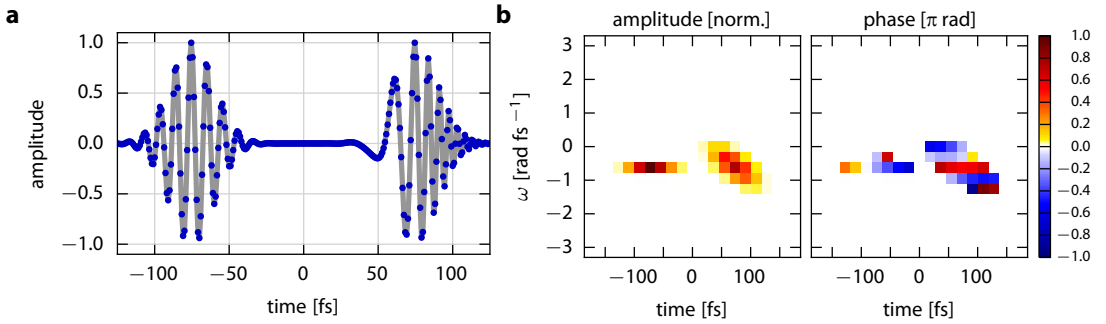

Figure 5.5: Ultrashort pulses in von Neumann representation. (a) Calculated double pulse including one chirped pulse (gray line). The temporal structure obtained from transforming the von Neumann representation back into the time-domain (blue dots) is identical with the initial signal. (b) von Neumann amplitude and phase using the bi-orthogonal basis set leading to localized coefficients (see text). Values of the phase are shown for pixels with an amplitude larger than 1 % of the amplitude maximum.

where the coefficients $c_{t_m w_n}$ are now localized near the times t_m and frequencies w_n.

Figure 5.5 illustrates the transformation of a complex time-domain signal containing two laser pulses [gray line, Fig. 5.5 (a)] centered in time at $\tau_0 = \pm 75$ fs into von Neumann space [Fig. 5.5 (b)], spanned by the bi-orthogonal basis. The two-dimensional joint time-frequency representation preserves the time-domain information and allows to identify the chirp of the second pulse and the time delay between both pulses, while using a significantly smaller number of coefficients. The basis set is complete, as demonstrated by transforming this signal back into the time domain [blue dots, Fig. 5.5 (a)] without artifacts.

5.2.2 Generating the von Neumann Basis for 2D Spectroscopy

Since dealing with 2D spectroscopy based on two coherence time axes, the vN representation will be generalized for a 2D signal $r(\tau, t)$ in the following. As this leads to two time and two frequency axes, the first coherence time τ and its Fourier-associated frequency ω will be denoted with Greek characters and the second coherence time t and its associated frequency w with Latin characters. Thus, a vN basis set expressed in terms of four parameters (τ_i, ω_j, t_m, w_n) is required that will be called the 2DvN representation. It can be obtained by numerically

calculating the tensor product of two 1D vN basis sets[7],

$$G(\tau_i, \omega_j, t_m, w_n) = g(\tau_i, \omega_j) \otimes g(t_m, w_n). \tag{5.2.6}$$

The vN coefficients for a 2D time-domain signal are then calculated in analogy to the one-dimensional case [Eq. (5.2.4)] by projecting $r(\tau, t)$ onto the 2DvN basis,

$$c(\tau_i, \omega_j, t_m, w_n) = \langle G(\tau_i, \omega_j, t_m, w_n) | r(\tau, t) \rangle \,. \tag{5.2.7}$$

Thus, the 2D time-domain signal is represented in a four-dimensional parameter space, which is flattened to two dimensions for purposes of graphic representation. This allows to visualize the spectral as well as the temporal properties of the signal simultaneously.

5.2.3 Properties of the 2D von Neumann Basis

The rephasing signal is of particular interest in coherent 2D spectroscopy since it allows to observe molecular couplings and to extract the homogeneous and inhomogeneous linewidths of the sample under study. For this reason, this signal contribution is used in order to demonstrate the properties of the 2DvN representation. In Fig. 5.6, the real part of the measured rephasing 2D signal of cresyl violet (confer Chap. 4.1) at a population time of $T = 300$ fs is compared in three different representations, the time domain [Fig. 5.6 (a)], the 2DvN domain [Fig. 5.6 (b)], graphically flattened to two dimensions by plotting a 2D grid of 2D spectra, and the frequency domain [Fig. 5.6 (c)].

Whereas the 1D vN transformation maps a 1D time- or frequency-domain signal into a joint 2D time-frequency representation (t_n, w_m), the 2DvN transformation maps 2D time- or 2D frequency-domain signals into a joint 4D space with basis parameters (τ_i, ω_j, t_m, w_n). The 2DvN space (τ_i, ω_j, t_m, w_n) is visualized by plotting a 2D spectrum (ω, w) for each time pixel in Fig. 5.6 (b) with the axis labels denoting the center position (τ, t) of the 2DvN basis functions in the time domain. For the time-domain representation [Fig. 5.6 (a)] a grid size of $N = 25$ for the time axes is used with the same temporal step size of 6 fs as in the experiment discussed in Chap. 4.1.1. This yields a $\sqrt{N} \times \sqrt{N} = 5 \times 5$ time-frequency grid for each of the two temporal dimensions, such that the same total number of data points arises as in the time domain and the corresponding Fourier representations. By choosing an odd number of frequency points, zero frequency and thus non-oscillating contribu-

[7] A. Shimshovitz and D. Tannor, private communication

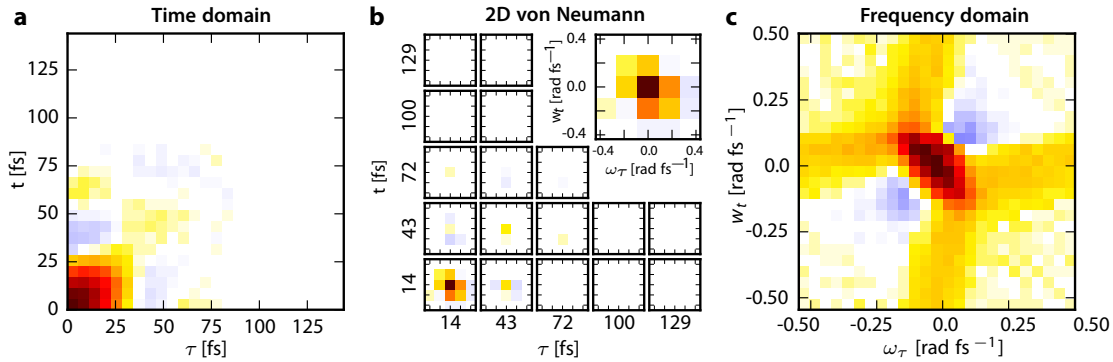

Figure 5.6: Comparison of the measured rephasing signal in three different domains. In each plot the real part is shown. (a) Time-domain data as acquired by the experiment, zero-padded to fill the chosen grid. (b) 2D von Neumann representation. The upper right is a zoom-in of the 2D spectrum at (τ, t)=(14 fs, 14 fs). (c) 2D Spectrum as obtained from the time domain by a conventional 2D Fourier transformation. Reproduced from Ref. [2], with the permission of AIP Publishing.

tions are explicitly included. Since the experimental data consists of 15 time steps, it is zero-padded accordingly prior to transformation. The vN coefficients of the first time pixel (τ, t)=(14 fs, 14 fs) in Fig. 5.6 (b) are calculated from the overlap of the corresponding local 2DvN basis functions (Fig. 5.7) with the time-domain signal in Fig. 5.6 (a). The 2D spectrum at this first time pixel is shown enlarged in the upper right of Fig. 5.6 (b), blocking graphically the underlying eight 2D spectra with amplitudes that are close to zero, see below. It has the same general structure as the 2D spectrum in the regular Fourier domain, as can be deduced by comparison with Fig. 5.6 (c). In addition, the decay of the amplitudes along the 2DvN time grid reflects the evolution of the signal in the time domain. This illustrates that the temporal as well as the spectral structure of the signal is preserved in the 2DvN representation (the preservation of information in the vN representation was proven previously [244]). Thus, the 2DvN representation essentially behaves as a 2D short-time Fourier transformation with a Gaussian window. It is apparent that the 2DvN representation contains the essential information about the signal, but is concentrated on a much smaller number of coefficients as compared to the Fourier representation, i.e., there are many more coefficients with vanishing amplitude in the whole plane of Fig. 5.6 (b) than in Fig. 5.6 (c). Therefore, mapping a 2D spectrum into 2DvN space increases the sparsity of the signal, and this will enable an optimized performance of compressed sensing reconstruction as shown below.

In order to further elucidate how the 2DvN basis compares to Fourier space with

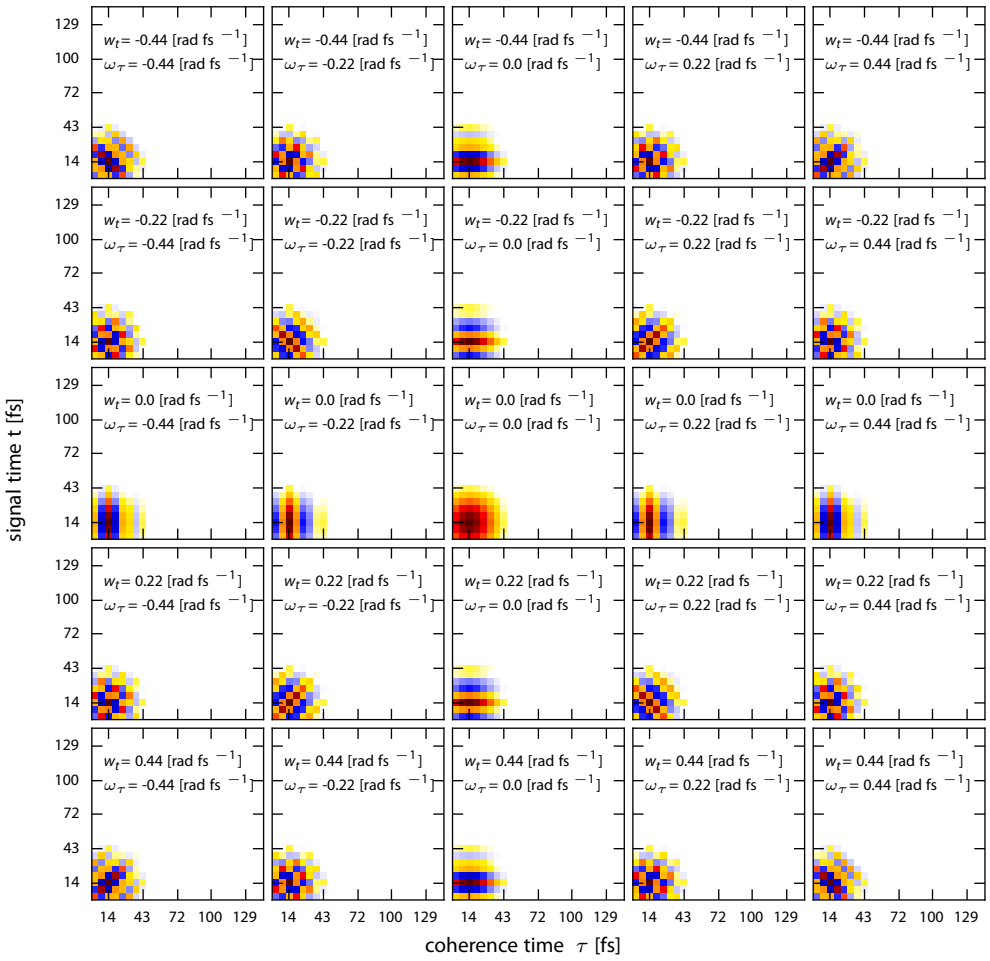

Figure 5.7: 2D von Neumann basis funtions. Real part of all local 2D von Neumann basis functions $G(\tau_i, \omega_j, t_m, w_n)$ centered at time pixel (τ, t)=(14 fs, 14 fs). The corresponding center frequencies for each basis function are annotated in each plot. Reproduced from Ref. [2], with the permission of AIP Publishing.

respect to sparsity and the influence of experimental noise on its performance as a sparsifying transform, a rephasing signal with similar properties as the experimental data is calculated in the time domain [Eq. (2.1.32)] using the same grid size of $N = 25$ for the time axes and a temporal step size of 6 fs as in the experiment. Experimental noise is introduced to each time-domain data point by adding a random number drawn from a Gaussian distribution. The standard deviation of this distribution is chosen as a certain percentage of the signals maximum amplitude. After transforming the signal into the 2DvN and Fourier domain, coefficients are

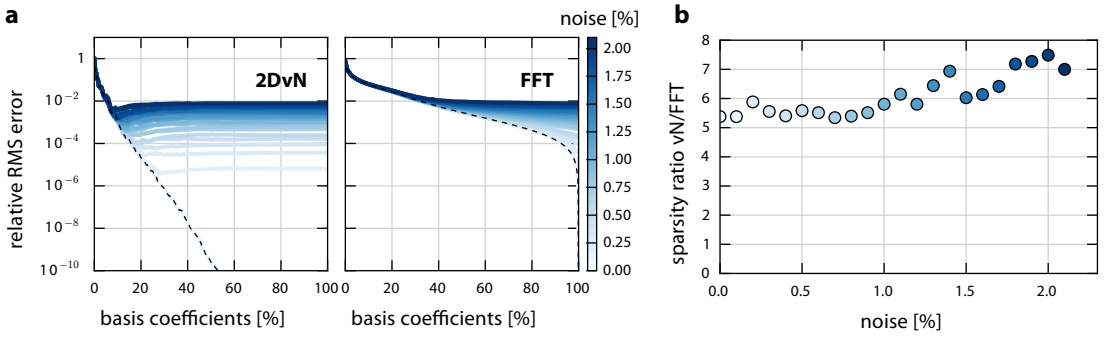

Figure 5.8: Effect of experimental noise on sparsity. (a) Error introduced in the real part of a time-domain signal as a function of retained basis coefficients in the 2DvN (left) and Fourier (right) domain for various amount of noise on the signal. The noise-free case is indicated by the black dashed lines. The 2DvN representation generally requires less coefficients for a reliable reconstruction of the signal. It can further be used to denoise the signal, as the error may even decrease when less coefficients are used. (b) Ratio of retained basis coefficients between 2DvN and Fourier representation at the 1 % error level.

gradually removed, i.e., set to zero, starting with the smallest absolute values. In each step, the inverse transformation is applied for comparison with the original signal and the relative root-mean square error introduced by this procedure is calculated

$$\epsilon = \sqrt{\frac{\frac{1}{n}\sum_i \left[\mu_O(i) - \mu_R(i)\right]^2}{\sum_i \left[\mu_O(i)\right]^2}}, \tag{5.2.8}$$

with μ_O denoting the original noise-free signal and μ_R the reconstructed signal from noisy data.

In the ideal case of noise-free data, the 2DvN representation contains the complete information about the signal in a much smaller number of coefficients than the Fourier representation. This can be inferred by comparing the black dashed lines in Fig. 5.8 (a). While the reconstruction error is well below 10^{-2} using about 5 % of vN coefficients, the Fourier domain requires about 30 % of the coefficients to retain the same reconstruction quality. For increased values of noise (shades of blue), the error using the 2DvN representation is relatively insensitive to the number of retained basis coefficients when keeping more than 40 %. For a given amount of noise, the error even slightly decreases when the number of retained basis coefficients falls below 20 %, leading to a dip in the traces that is most pronounced in the lines for larger amount of noise (dark blue). This indicates a better agreement with the noise-free reference data and means that the reconstruction error with respect to the noise-free data even decreases when using a smaller number

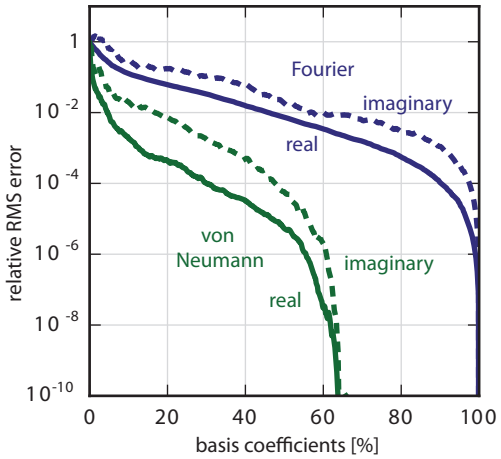

Figure 5.9: Sparsity of 2DvN basis compared to Fourier basis. The error introduced in the real (solid) and imaginary (dashed) parts of the experimental time-domain signal is shown as a function of the basis coefficients used in the 2DvN (green) or Fourier (blue) domain. At any given error level, the 2DvN representation requires a much smaller number of basis coefficients, thus it is more sparse than frequency space. Reproduced from Ref. [2], with the permission of AIP Publishing.

of coefficients. Hence, the 2DvN representation can be used to denoise experimental data by distilling the essential features of the signal, as already suggested for applications in quantum control [245]. In contrast, the error introduced using the Fourier transformation always increases for a decreased number of retained basis coefficients.

The observed behavior could be explained by considering the signal multiplexing property of the Fourier transformation. Removing one coefficient in the frequency domain alters all time-domain points and prohibits to selectively suppress noise at a given point in time. Contrary to this, the 2DvN basis acts as a windowed Fourier transformation with mainly localized basis functions[8]. Thus, removing a 2DvN coefficient mainly affects those points in the time-domain that are in the vicinity of the corresponding 2DvN basis function. As the signal is close to zero anyways in large portions of the time domain [Fig. 5.6 (a)] and mainly consists of noise in those regions, the corresponding noisy 2DvN coefficients can be safely removed (set to zero) without affecting important parts of the signal.

The performance of the 2DvN basis for increasing noise can be quantified by retrieving the sparsity of each domain (defined here by the percentage of retained basis coefficients at a reconstruction error level of 1 %) and calculating their ratio. This reveals that the sparsity of the 2DvN representation is more than five times larger and even increases for larger amount of noise [Fig. 5.8 (b)].

The same comparison can be conducted for measured data of cresyl violet (Fig. 5.9), comparing the error that is introduced in the real and imaginary part of

[8]Compared to the completely de-localized time-domain representation of the Fourier basis functions (sinusoids), the "non-local" bi-orthogonal vN basis functions [Fig. 5.4 (b)] are still localized.

the time-domain data by removing basis coefficients in the 2DvN and the Fourier domain. In this case, the (noisy) experimental data was used as a reference for comparison. Defining an error of one percent as the threshold for a reliable reconstruction, the 2DvN representation requires 4.5 % (16.8 %) of the basis functions for reconstructing the real (imaginary) part. In contrast, using the Fourier representation the threshold is reached with 45.8 % (57.4 %) of the basis coefficients.

5.3 Optimizing Sparse Sampling

Coming back to the problem of optimized sampling with compressed-sensing reconstruction, Eq. (5.1.1) can be re-written by explicitly including the matrix $\boldsymbol{B}$ of bi-orthogonal 2DvN basis functions and the 2DvN coefficients $\boldsymbol{c}$ in the representation of the time-domain signal $\boldsymbol{r}$

$$\boldsymbol{r} = \boldsymbol{\Phi B c}. \tag{5.3.1}$$

In order to find the sampling matrix $\boldsymbol{\Phi}$ with the best reconstruction results from an undersampled data set $\boldsymbol{r}$ of the reference measurement, the TwIST solver is incorporated into the framework of a genetic algorithm. Prior to optimization of the sampling matrix the regularization parameter λ [Eq. (5.1.4)] needs to be determined. For this, the reference data is sampled with a higher density (35 %) and a ternary search algorithm is subsequently applied in order to find λ such that it yields the best reconstruction. Next, the optimization is initiated with a random Poisson-gap sampling matrix [225] with the desired undersampling percentage, which is in this case 25 % of the data points of the full sampling matrix. As depicted in the flowchart of the algorithm (Fig. 5.10) the matrix is mutated, i.e., a small fraction of the sampling points ("mutation rate") is moved to a different, random position. The data is sampled using the new matrix and subsequently used as the input for the TwIST reconstruction algorithm. A fitness value is calculated comparing the reconstruction result and the original coefficients. If the fitness did not increase with the mutation, the sampling matrix is discarded. Otherwise, it is selected as the best matrix and the mutation-and-reconstruction procedure is repeated. If there was no beneficial mutation in a certain number of generations, the mutation rate is lowered in order to explore the vicinity of the best matrix in more detail. The algorithm is stopped when the mutation rate has decreased to zero. The total fitness is calculated as a weighted sum over the individual

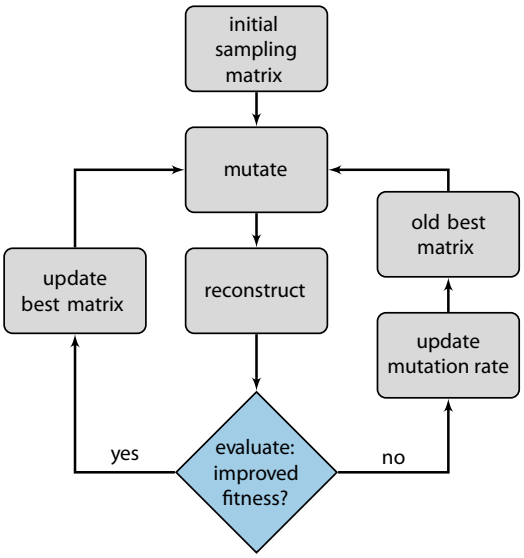

Figure 5.10: Flowchart of the genetic algorithm to optimize the sampling matrix. The initial matrix is mutated, i.e., a small fraction of sampling points (mutation rate) is exchanged. The new sampling matrix is used subsequently to undersample the data and reconstruct the signal using the TwIST algorithm. If the mutation increased the fitness (see text) of the reconstructed signal, the matrix is selected as the new best matrix. Otherwise it is discarded and the mutation rate is adjusted accordingly. The algorithm is stopped if the mutation rate has decreased to zero. Reproduced from Ref. [2], with the permission of AIP Publishing.

coefficients,

$$F_{tot} = \sum_i W(i)F(i), \tag{5.3.2}$$

where the individual coefficient fitness is given by

$$F(i) = 2\frac{\mu_O(i)\mu_R(i)}{\mu_O^2(i) + \mu_R^2(i)}, \tag{5.3.3}$$

comparing the amplitude of the original 2DvN coefficients and the corresponding reconstructed 2DvN coefficients. The weights

$$W(i) = \frac{\mu_O^2(i)}{\|\mu_O^2(i)\|_2^2} \tag{5.3.4}$$

are calculated from the amplitudes of the 2DvN coefficients. This procedure is done for the real as well as the imaginary part of the rephasing and nonrephasing signal. All four fitness values are averaged to yield a single value for the reconstruction quality.

5.4 Results and Discussion

The acquisition concept introduced in this chapter is applied to the data set of cresyl violet (Chap. 4.1), aiming to reproduce the quantum beatings observed pre-

viously [151, 179, 184, 186] from an undersampled data set. Anticipating a decay of the signal for larger waiting times and thus a greater sensitivity to the influence of experimental noise, the 2D spectrum with the smallest signal amplitude at $T = 300$ fs is chosen as a reference data set and therefore used to optimize the sampling matrix. However, other times are also feasible. The new approach was also tested with $T = 90$ fs as a reference data set and obtained similar results as the ones discussed below. Prior to reconstruction, the sampled data are zero-padded to fill the chosen $N = 25$ grid for each temporal dimension. For the calculation of the reconstructed 2D spectra arising from optimal sampling and their comparison with the regularly sampled 2D spectra, the reconstructed time-domain signal is truncated to the size of the original data.

The evolution of the fitness value during the optimization of the sampling matrix as a function of the number of generations is shown in Fig. 5.11 (a). Within 7000 generations, the fitness has increased from an initial value of 0.78 for a Poisson-gap sampling matrix to a final value of 0.99. Accordingly, the sampling matrix has evolved, as shown in Fig. 5.11 (b). The sampling is now mainly concentrated at the origin of the τ-t parameter space, since most of the information about the signal is present in this region. However, sampling in intermediate and more distant regions is also necessary to get the best reconstruction result.

In order to test if sampling in distant regions is really needed the optimization was repeated afterwards with an initial sampling matrix having the sampling points distributed uniformly along t and τ in 6 fs steps from 0 fs to 42 fs, which corresponds to the bottom left quarter of the original time grid and thus also to a 25 % coverage of the full sampling matrix. The genetic algorithm evolved this starting matrix into a similar structure as the optimized matrix shown here, demonstrating the need to sample in the outer regions for a better reconstruction. Applying a specifically designed semi-uniform starting distribution similar to the optimized sampling matrix obtained here might lead to faster convergence of the genetic algorithm and could be used if optimization time is of critical importance.

In Fig. 5.11 (c) the 2DvN coefficients of the original and the recovered data are correlated for both the rephasing (blue dots) and the nonrephasing (green dots) contributions on a double-logarithmic scale. For this the absolute values of the real and imaginary part are shown in a joint scatter plot. The largest coefficients (down to the 5 % level) line up very well along the diagonal (black line, indicating perfect correlation) and therefore prove the excellent reconstruction quality using just 25 % of the original sampling points. The deviations in the smaller coefficients only play a minor role, since they do not contain the main information about the signal structure, as shown in Chap. 5.2.3 and displayed in

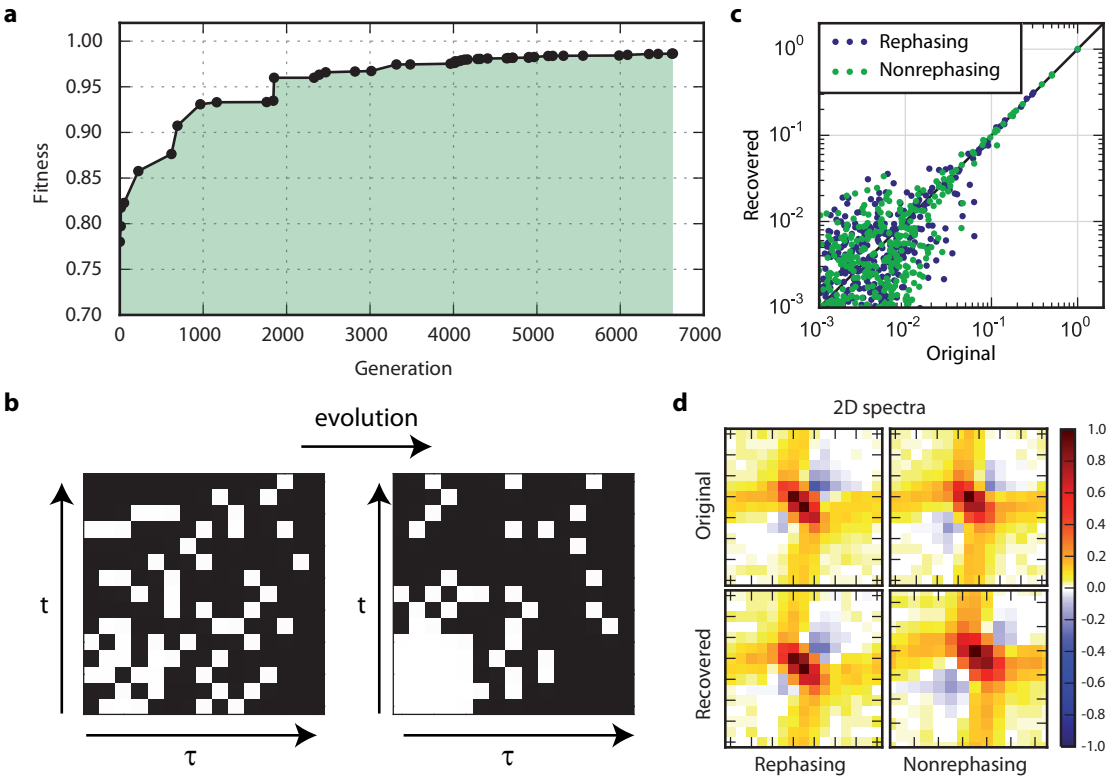

Figure 5.11: Optimization results. (a) Evolution of the fitness value for each generation during optimization. A black circle is shown for every beneficial mutation. These are more frequent immediately after a decrease of the mutation rate and hence a more detailed exploration in the vicinity of the current best matrix. (b) Initial Poisson-gap sampling matrix (left) and optimized best sampling matrix (right). Sampled data points are denoted by white squares. The evolution brings more sampling points closer to the origin of the (τ, t) space, however sampling in more distant regions is also necessary for good reconstruction. (c) Correlation plot comparing the original and recovered 2DvN coefficients for the rephasing (blue dots) and nonrephasing (green dots) contribution. The largest and most important coefficients line up perfectly with the diagonal (note the double-logarithmic scale). (d) Comparison of original and reconstructed (rephasing, nonrephasing) 2D spectra in frequency space using the optimized sampling matrix. Reproduced from Ref. [2], with the permission of AIP Publishing.

Fig. 5.9. This is also demonstrated in Fig. 5.11 (d), comparing the rephasing and nonrephasing 2D spectra that were obtained from transforming the reconstructed 2DvN representation via the time domain into frequency space.

In the next step, the optimized sampling pattern is applied to the data at other population times, which would hypothetically be measured after the optimization using the result of the genetic algorithm (in the present work, the full data set

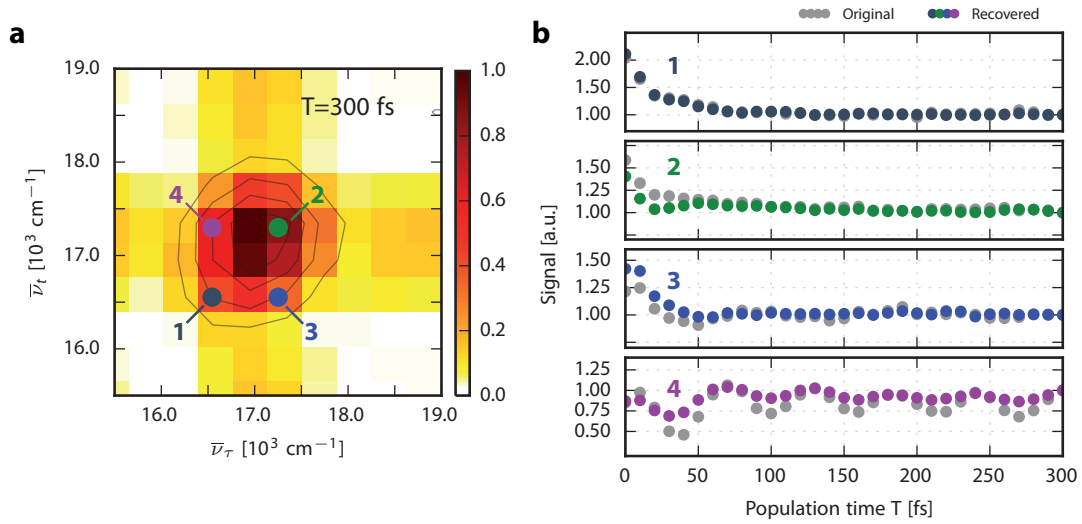

Figure 5.12: Coherent oscillations at different positions in the 2D spectrum of cresyl violet analyzed from optimally sampled data.(a) Absorptive 2D spectrum of cresyl violet at $T = 300$ fs. The filled circles indicate the regions of interest (ROIs). (b) Amplitude of ROIs as a function of population time. The grey circles indicate the measured values from the full data set, the colored circles the recovered amplitudes using compressed-sensing reconstruction. Reproduced from Ref. [2], with the permission of AIP Publishing.

was measured to facilitate a comparison). As the genetic algorithm takes about 20 minutes on a standard workstation, this can be incorporated into the usual lab routine without much loss of measurement time or changes in the experimental conditions. In Fig. 5.12 (a) the absorptive spectrum of cresyl violet at a population time of 300 fs is shown. In contrast to the results presented in Chap. 4.1, the data was Fourier transformed without zero padding, resulting in the coarse frequency grid. The spectrum is presented with laboratory-frame frequency axes by adding the rotating-frame center frequency to the measured frequencies.

In order to extract and analyze the vibrational coherence over the population time T, four regions of interest (ROIs) are selected in the 2D spectrum. They are indicated by colored, filled circles. Their evolution as a function of population time T is plotted in Fig. 5.12 (b) (same colors) in comparison with the full data set (gray circles), normalized to the ROI value of the reference data ($T = 300$ fs). Especially for the crosspeak (ROI 4) the expected oscillation with a frequency of 580 cm^{-1} can be resolved. The compressed-sensing reconstruction closely follows the values from the full set, and the coherent oscillations in ROI 4 can be accurately resolved.

Thus, by using only 25 % of the original sampling points, the almost complete

information about both the peak shape [Fig. 5.11 (d)] and its temporal evolution [Fig. 5.12 (b)] can be recovered.

5.5 Conclusion

The work presented in this chapter introduces a new scheme for employing compressed-sensing reconstruction in coherent multidimensional spectroscopy.

The basic concept is to optimize a reduced sampling matrix for best data recovery at one particular population time using a genetic algorithm and then to apply that matrix for data acquisition at all other population times. In combination with rotating-frame data acquisition, this permits to decrease the measurement time substantially without significant loss in information content of the resulting 2D spectra. For instance, laboratory-frame data acquisition of the data set presented in this chapter requires scanning of more than $6 \cdot 10^6$ parameters, including 27-step phase cycling, 31 population times and 85 time steps for each of the two coherence times (assuming a step size of 1 fs). Rotating-frame acquisition reduces this to 188325 steps as demonstrated in Chap. 4. The approach presented in this chapter is capable of retrieving the same information while scanning only 52245 parameters. This is facilitated by a compact representation of 2D spectra generated by the von Neumann basis that increases the sparsity in the transform domain of the compressed-sensing reconstruction algorithm.

The lower limit to the sampling density is given by the sparsity of the signal. Due to inhomogeneous broadening, liquid-phase 2D spectra measured in the rotating frame are not considered as sparse. In this case, the von Neumann representation of 2D spectra is useful to reduce the number of non-zero coefficients and thus to increase sparsity, which is beneficial for sparse recovery algorithms as shown here. Further applications of the 2DvN representation can be envisioned. For example, designing a pulse train capable of directly measuring the 2DvN coefficients would significantly speed up acquisition times, since only about 5 % of the largest coefficients are sufficient to fully describe the signal. The 2DvN representation introduced here can also be useful for analysis of conventionally recorded 2D spectra by condensing the data to a few relevant coefficients while retaining the full information content.

Optimal sparse sampling can decrease measurement times in population-based 2D spectroscopy by a factor of four, especially when shot-to-shot pulse shaping is available. Thus, the number of collected data points can be reduced while keeping the full duty cycle of data acquisition. The new acquisition approach in

connection with 2D spectroscopy will be especially interesting, for example, for the detailed study of photophysical processes and photochemical reactions, for which a high time resolution and a large range of population times are required. Even larger savings in acquisition time can be anticipated for molecular systems that exhibit long-lived coherences such as in 2D spectra of atomic vapor [58, 108, 220] or molecular beams that feature sparse signals in the frequency and likewise in the von Neumann domain.

6 | Molecular-Beam Coherent 2D Electronic Spectroscopy

While the previous chapters of this work were dealing with 2D electronic spectroscopy of samples in solution, this chapter introduces a new technique to acquire 2D spectra of molecules in the gaseous phase. Whereas this has been done before for samples of atomic vapor detecting optical signals [58, 103, 108, 252, 253], the experiments presented in the following pursue a new approach and aim to observe cations originating from the interaction of the excitation lasers with molecules in a molecular beam. This does not only allow to shed light on photophysical processes of gaseous samples, but also enables direct detection of dissociation products emerging from photo-excitation with a phase-coherent multipulse sequence. Hence, the new approach permits to study, for instance, the evolution of coherences during photochemical reactions, e.g., bond breakage, via the simultaneous acquisition of coherent 2D spectra of all reaction products. Moreover, it provides a new tool for comparison of gas-phase and liquid-phase dynamics.

Molecular beams are a classic tool for time-resolved spectroscopy of atoms and molecules in an isolated environment, decreasing the system–bath interaction to a minimum. This leads to narrow linewidths and facilitates comparison with theoretical calculations. Applications of molecular beams include the gas-phase investigation of transition states in photochemistry [14, 254], vibrational wavepackets [20–22], or excited-state dynamics of biologically relevant molecules [255–257] by using pump–probe techniques with photoelectron or -ion detection. Furthermore, ultracold samples such as helium nanodroplets [258, 259] enable, e.g., the investigation of multiple-quantum coherences [260, 261]. Other approaches [262] employ coincidence detection and velocity-map imaging to retrieve information about reaction kinetics and energy levels involved, permitting, for instance, chiral recognition in the gas phase [263, 264].

Molecular-beam coherent 2D electronic spectroscopy combines 2D spectroscopy

with molecular beams and utilizes cations for probing the final-state population. Using time-of-flight mass spectrometry, a 2D spectrum is obtained simultaneously for the parent molecule and each of its fragments. With the new experimental method, ionization pathways in nitrogen dioxide (NO_2) are investigated and the first ion-selective 2D spectrum of a molecular-beam sample is acquired.

6.1 Properties of Nitrogen Dioxide

Nitrogen dioxide is a compound that is heavily studied in literature, primarily due to its negative impact on human health as a major byproduct of combustion processes in engines and fossil-fueled power plants. Besides this, nitrogen dioxide plays a central role as a catalyst in the Earth's atmosphere, in particular in the depletion of the ozone layer due to the photochemically induced decomposition of NO_2 and subsequent reaction of the NO product with ozone O_3 [265]. The photophysics and photochemistry of NO_2 have been the key aspect of numerous studies in the past that were motivated by the complex absorption features and the variety of photochemical reaction pathways that are possible after photo-excitation. The complex absorption profile in the visible spectral range [Fig. 6.1 (a)] results from vibronic coupling that is caused by mixing of several low-lying excited-state potential-energy surfaces [266]. The first dissociation limit is reached upon photoexcitation with an energy exceeding 3.12 eV (397.4 nm). For higher excitation energies, the absorption profile is dominated by transitions into several Rydberg states. Transitions into Rydberg states are accompanied by a change in molecular geometry, as the O–N–O bond angle increases from 134.25° in the ground state to 180°, which also corresponds to the geometry of the first ionic state. In multiphoton ionization experiments, these Rydberg states can be used as stepping states towards the ionic ground state at an adiabatic ionization energy of 9.586 eV [267]. An extensive review of NO_2 photodynamics can be found in Ref. [266].

NO_2 is in a thermodynamic equilibrium with its dimer NO_2O_4 that shifts to the monomer for increased temperatures. For temperatures above 100 °C, the sample is to more than 95 % composed of NO_2 [270, 271]. A typical mass spectrum of the NO_2 sample with the nozzle heated to 150 °C is shown in Fig. 6.1 (b), displaying the NO_2^+ parent ion and the NO^+ fragment. Peaks of other mass-to-charge ratio are not observed in the experiments conducted in this work. For data analysis in the time-resolved experiments presented in this chapter, the mass peaks are integrated over a window of 20 sampling points corresponding to a mass-to-charge ratio of 0.1 amu/z.

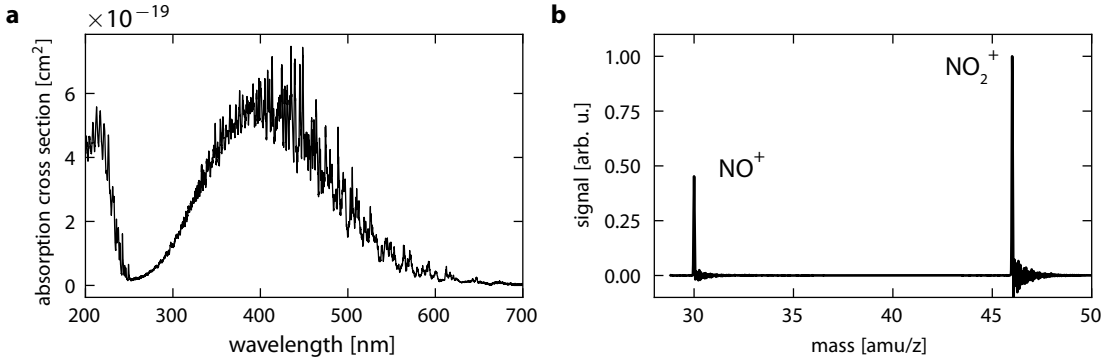

Figure 6.1: Properties of NO_2. (a) Absorption cross section of NO_2 in the UV-visible spectral region at a temperature of 298 K, reproduced from Ref. [268] and accessed via Ref. [269]. (b) Mass spectrum of NO_2 as obtained from ionization with the UV pulse showing the parent ion NO_2^+ and the NO^+ fragment.

NO_2 was chosen as a sample molecule to demonstrate the new technique of molecular-beam 2D spectroscopy, since its photodynamics are well studied in literature using various time-resolved pump–probe techniques. Furthermore, ongoing research on the origin of coherent dynamics observed in NO_2 [270–277] and on the states involved in photoionization [278–280] address questions that could be approached by time-resolved multidimensional spectroscopy. From the experimental side, NO_2 has the benefit that it is commercially available in gas containers that allow to maintain a constant sample supply and to run long-term experiments without the need of sample exchange.

6.2 Experimental Configuration

The ionization of small molecules typically requires energies on the order of 10 eV and therefore the absorption of multiple photons in the visible regime. As the setup presented in this chapter aims to investigate fourth-order processes corresponding to the absorption of two visible photons (equal in energy to maximum 5 eV), a UV pulse is used additionally. It provides the necessary energy to either ionize and interrogate the excited-state population generated by the interaction with the visible pulse, or to prepare the samples in an energetically high-lying state such that the visible pulse can be used for probing. In the experiment (Fig. 6.2), the UV pulse ($\lambda = 267$ nm) is derived from the third harmonic of the Ti:Sa fundamental and the visible pulses ($\lambda = 540$ nm) are generated by a NOPA that is followed by

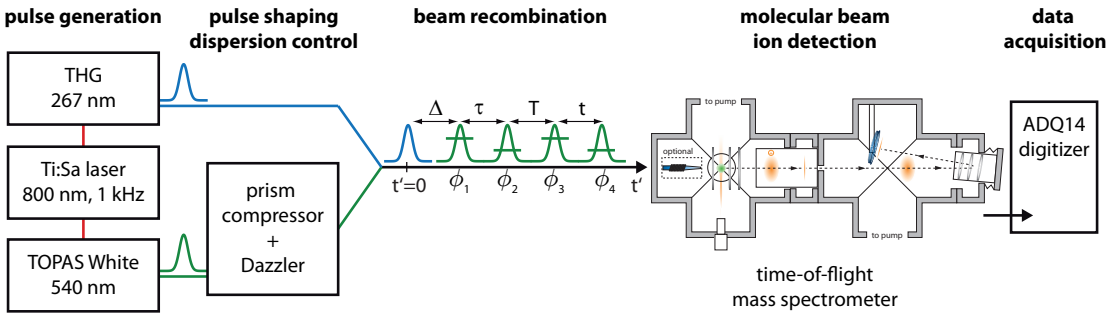

Figure 6.2: Schematic layout of the experimental setup for molecular-beam coherent 2D electronic spectroscopy. The Ti:Sa fundamental beam (Chap. 3.1.1) serves to pump the NOPA (Chap. 3.1.2) and is used to generate the third harmonic (Chap. 3.1.3) in a second branch. The delay Δ between the UV pulse and the visible pulse sequence generated by the Dazzler pulse shaper (Chap. 3.2.1) can be adjusted by a delay stage in the fundamental beam of the UV branch (not shown). The beams are recombined collinearly using a dichroic mirror and focused into the interaction region of the reflectron time-of-flight mass spectrometer (Chap. 3.3.2).

a Dazzler pulse shaper. Both pulses are collinearly recombined using a dichroic mirror and delayed with respect to each other by a computer-controlled delay stage (M-ILS250CCHA , Newport Spectra Physics) in the fundamental beam path of the UV branch. They are focused into the interaction region of a home-built reflectron-type [171] time-of-flight mass spectrometer (TOF-MS) using a $f = 200$ mm lens.

For laser pulse characterization, a planar mirror is placed in front of the vacuum viewport of the mass spectrometer, mapping the focus of both pulses to an accessible region outside the chamber. An identical viewport is inserted in this beam path to ensure the same total amount of glass and characterization is carried out at the external focus position. The visible pulse is compressed to 17 fs by the pulse shaper and characterized via pulse-shaper-assisted collinear frequency-resolved optical gating (cFROG) [130, 159] using a 10 μm BBO crystal (the compressed pulse is shown in Chap. 3.2.3). The UV pulse has a pulse duration of 130 fs as characterized via xFROG [159] in a difference-frequency-generation process with the compressed visible pulse as the reference.

For pump–probe and 2D experiments using both pulses, the intensities at the sample position are adjusted to 1×10^{13} $\frac{\mathrm{W}}{\mathrm{cm}^2}$ for the (single) visible probe pulse and 3×12^{11} $\frac{\mathrm{W}}{\mathrm{cm}^2}$ for the UV pump pulse. For 2D experiments using only the visible pulse sequence, the beam diameter was expanded by a factor of two before the focusing lens. In these experiments, the maximum intensity of the visible pulse was 2×10^{13} $\frac{\mathrm{W}}{\mathrm{cm}^2}$. The NO_2 sample is expanded as an effusive beam into the vacuum chamber, increasing the base pressure in the interaction region to

1×10^{-4} mbar. In order to avoid contributions of N_2O_4, the nozzle is held at a constant temperature of 150 °C by PID-controlled resistive heating of a Constantan wire that is wrapped around it. The ion signal is detected on a shot-to-shot basis with a micro-channel-plate (MCP) detector and recorded with the analog-to-digital converter card (ADQ14) after amplification.

6.3 Pump–Probe Mass Spectrometry of NO_2

Conventional pump–probe experiments scanning the time delay between one UV pulse and one visible pulse are conducted first in order to benchmark the setup with existing literature. The data set acquired in this experiment provides the basis for later comparison with the results using multiple visible pulses and aims to retrace the known ultrafast dynamics of NO_2. The delay Δ between UV pump and visible probe pulse is scanned from -5 ps to -500 fs in 46 steps steps (100 fs), from -500 fs to 750 fs in 126 steps (10 fs), from 750 fs to 5 ps in 43 steps (101.2 fs) and additionally from 5 ps to 100 ps in 41 steps with exponentially increasing step size. Here, $\Delta > 0$ corresponds to the UV pulse acting as pump and the visible pulse as probe pulse. For each time delay the signal is integrated over 2000 laser shots and averaged over 40 complete scans. Pulse polarizations were chosen parallel to each other and are perpendicular to the time-of-flight axis. Since pump and probe beam on their own already generate ions, a chopping sequence is used at each delay position in order to measure the pump-only and the probe-only mass spectrum and thus to extract the pump–probe signal by subtracting both from the mass spectrum when both pulses are present.

Data Analysis

In Fig. 6.3 (a), the measured pump–probe signal for the NO_2^+ parent ion (purple dots) and the NO^+ fragment (orange dots) is shown as a function of the delay Δ between UV and visible pulse. A parallel kinetic rate model [281, 282] is used to fit both traces simultaneously. This results for positive delay times (for which the UV acts as a pump) in a decay with time constants of $\tau_1^+ = (60 \pm 10)$ fs, $\tau_2^+ = (264 \pm 47)$ fs (red line), $\tau_3^+ = (3222 \pm 589)$ fs and a slow decay of several hundred picoseconds for the fragment trace. For negative delay times, a decay with $\tau_1^- = (141 \pm 106)$ fs and a persistent signal for up to -100 ps (long-time data measured in a separate experiment) is observed for the fragment trace. All contributions (gray lines) are convoluted with a Gaussian instrument response function centered at time zero and a FWHM of (100 ± 2) fs as obtained from

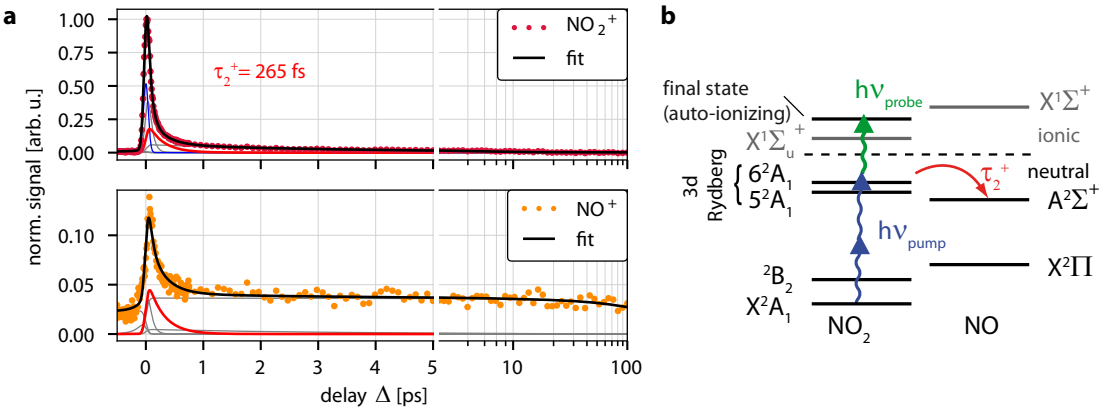

Figure 6.3: Pump–probe mass spectrometry of NO_2 using 267 nm pump and 540 nm probe pulses. (a) NO_2^+ signal (purple dots, upper diagram) and NO^+ signal (orange dots, lower diagram) as a function of pump–probe delay Δ. Positive Δ signifies that the UV pulse arrives first. Note the logarithmic delay axis for $\Delta > 5$ ps. The black lines indicate the fit of a kinetic rate model (see text) to the data, the grey lines show the different contributions to this model. The instrument response function (blue line) is used to account for the ion yield during pulse overlap. The contribution attributed to NO_2 dissociation is highlighted (red line). (b) Energy levels of NO_2 relevant for the dynamics observed at positive delay times. The UV pulse prepares 3d Rydberg states (corresponding to 5^2A_1 and 6^2A_1) by two-photon absorption (blue arrows) which is probed by the visible pulse (green arrow). This leads to dissociation and production of neutral NO fragments (red arrow). The decay of the parent ion signal with the time constant $\tau_2^+ = 265$ fs is attributed to this dissociation process. Reproduced from Ref. [4].

the fit. The instrument response function is added as a separate contribution to account for the ion yield during pulse overlap and only contributes to the parent ion with non-negligible amplitude (blue line).

Discussion

The observed dynamics for negative delay times can be rationalized by considering the complex absorption profile of NO_2^+ between 250 nm and 650 nm [Fig. 6.1 (a)]. A 540 nm pump photon is equivalent to an energy of 2.30 eV and therefore leads to an excitation below the dissociation limit into the mixed $^2A_1/^2B_2$ band. Vredenborg et al. [283] observed a contribution with a decay timescale of less than 200 fs after the absorption of one 400 nm pump photon (3.10 eV) in (NO_2^+, e^-) coincidence experiments, corresponding well to the $\tau_1^- = (141 \pm 106)$ fs decay observed here. They attributed the timescale of this contribution to a spreading of the prepared wavepacket on the excited state which reduces the cation yield of the subsequent

ionization pulse. If no dissociation takes place, the lifetime of the prepared excited states is estimated to be on the order of μs in collision-free environments [266]. This is most likely the reason for the weak persistent offset in the pump–probe signal at negative delay times.

For positive delay times (UV acts as pump) both fragments show a fast initial relaxation with a time constant of $\tau_1^+ = (60 \pm 10)$ fs and a subsequent decay with $\tau_2^+ = (265 \pm 47)$ fs (red line) and $\tau_3^+ = (3222 \pm 589)$ fs. Whereas the parent ion completely decays to zero for $\Delta > 10$ ps, the fragment ion exhibits a remaining signal for larger pump–probe delays with a decay time exceeding the scanning range of the measurement. Previous experiments using 267 nm pump and 400 nm probe pulses identified several excitation pathways using velocity-map imaging [270–273, 283, 284]. One major ionization pathway contributing to the pump–probe signal of the parent ion was identified as the excitation to the 3d Rydberg states of NO_2 at an energy of 9.2 eV by the absorption of 2 (3) 267 nm (400 nm) photons. In C_{2V} symmetry they correlate with the 5^2A_1 and 6^2A_1 states [266] [Fig. 6.3 (b)]. Already in earlier fluorescence depletion experiments these Rydberg states were shown to dissociate on a timescale of less than 500 fs and form excited NO in the $A^2\Sigma^+$ state [285]. In addition, a contribution from long-lived Rydberg states at these energy levels has also been observed [273, 283]. Hence, the observed dynamics of the parent ion, in particular the 265 fs decay, can be attributed to the absorption of two 267 nm pump photons and subsequent dissociation of highly-excited NO_2, as shown in Fig. 6.3 (b). The probe step ionizes the molecule by the absorption of one 540 nm photon, leading to the observed ion signal. Accordingly, the long-lived contribution in the NO^+ signal is assigned to the product of neutral NO_2 dissociation and subsequent ionization by multiple photons of the probe pulse. Moreover, the initial fast relaxation dynamics observed for the parent ion is also present in the fragment trace. This signal cannot originate as a direct product from neutral NO_2 dissociation and must result from the final NO_2 state that is reached from the 3d Rydberg states after absorption of the probe photon.

Recent experiments [279] discussed the role of high-lying Rydberg states in photoionization of NO_2 and highlighted the aspect of (NO^+, O^-) ion pair formation at energies of about 11.5 eV in addition to auto-ionization [278, 280]. This energetic region is accessible by (2+1)-excitation (11.51 eV), which is why the origin of the NO^+ signal at short delay times is ascribed to the ion pair-formation state. Consequently, the parent ion is conjectured to be generated via absorption to these high-lying Rydberg states and subsequent auto-ionization or via direct ionization into the ionic ground state.

Time constant [fs]	Assignment	Literature values
Neg. delay offset	$^2B_2$ Excited-state lifetime	> 10 μs [266, 286]
$\tau_1^- = 141 \pm 106$	$^2B_2$ Wavepacket spreading	< 200 fs [283]
$\tau_1^+ = 60 \pm 10$	3d Rydberg states lifetime	no clear assignment found
$\tau_2^+ = 265 \pm 47$	3d Rydberg states lifetime	< 500 fs [270–274, 283, 285, 287, 288]
$\tau_3^+ = 3222 \pm 589$	Long-lived Rydberg state	[273, 283]
Persistent fragment signal	Dissociation product	

Table 6.1: Summary of observed time constants and their assignment to different processes and comparison with literature. Time constants with a positive (negative) superscript correspond to the UV (visible) pulse acting as the pump. Reproduced from Ref. [4].

Table 6.1 summarizes the observed timescales and assignments of different processes.

6.4 Determination of Signal Nonlinearity

The findings of the work discussed in the previous section are corroborated by measuring the dependence of the NO_2^+ pump–probe signal on pump and probe power at selected delay times. Laser power variation is carried out by rotating a half-wave plate in front of a polarizer, both positioned in the particular beam path. The pump–probe signal is extracted by a chopper sequence as described previously. Power-law fits [black lines, Fig. 6.4 (a)] to the experimental data show that the pump–probe signal at a delay of $\Delta = 250$ fs requires the absorption of two UV photons (blue circles) and one photon of the visible pulse (green circles).

In addition, the power dependence of the NO_2^+ and NO^+ ion yields using the visible pulse only was determined [Fig. 6.4 (b)]. The fits (black lines) demonstrate that it requires four visible photons to generate NO_2^+ ions (blue circles) and five photons for the NO^+ fragment ions (green circles). This is in line with previous observations in literature, where the dominant ionization pathway at wavelengths larger than 500 nm has been attributed to a (1+2+1) resonance-enhanced multiphoton-ionization process [289]. In particular, the NO_2 molecule is resonant at the one photon level, exciting the molecule into the $^2A_1/^2B_2$ manifold. Furthermore, at the level of three photons, the 3s Rydberg states at a total energy of about 7 eV come into resonance and can be used as stepping states towards ionization. The vertical ionization potential of NO_2 (11.23 eV) cannot be overcome by four photons in the spectral region used here. However, at the resonance level of the third photon, the equilibrium geometry of the molecule changes from a bent ground state

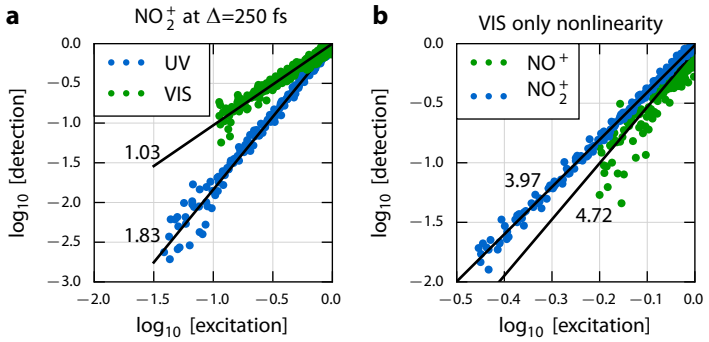

Figure 6.4: Signal nonlinearity. Data have been normalized prior to analysis. (a) NO_2^+ pump–probe signal at a delay time of $\Delta = 250$ fs under variation of the 267 nm pump (blue) and the 540 nm probe (green) intensity. Fits are shown as solid lines with power-law exponents indicated. (b) NO_2^+ (blue) and NO^+ (green) signal using the 540 nm pulse only with corresponding fits (black) and power-law exponents. Reproduced from Ref. [4].

configuration to a linear configuration as detailed in Chap. 6.1. At this geometry the energy of four photons of the laser spectrum ranging from 510 nm to 570 nm is just below the adiabatic ionization potential (9.586 eV) into the ionic ground state.

6.5 2D Spectroscopy of NO_2 Rydberg states

Having investigated the dominating ionization pathways with pump–probe spectroscopy, this section aims to demonstrate the capabilities of combining molecular beams and time-of-flight detection with ultrafast pulse shaping. Splitting the single visible probe pulse into a train of four phase-cycled collinear pulses enables to acquire transient multidimensional spectra [290–292] of the excited 3d Rydberg states for any given delay Δ between the UV pump and the first visible probe pulse. Scanning Δ retrieves transient information about the evolution of coherences during bond breakage after photoexcitation of the 3d Rydberg states. In the experiments presented in this section, the coherence times t and τ are scanned from 0 fs to 200 fs in 10 fs steps in a rotating frame ($\gamma_0 = 0$), while the population time T and the delay Δ between the UV pump pulse and the visible probe pulses are kept constant at $T = 30$ fs and $\Delta = 150$ fs. In total, the multidimensional spectroscopy measurement scheme contains 11907 different pulse shapes, including 27-step phase cycling and 21×21 coherence times, which are scanned on a shot-to-shot basis similar to rapid-scan coherent 2D fluorescence spectroscopy (Chap. 4).

The measurement is repeated 27000 times for averaging.

Different types of nonlinear signals can be selected from the full data set after data acquisition using the phase-cycling scheme (Chap. 2.2.3). In the first paragraph, pump–probe like contributions arising from only two interactions with the four visible pulses are analyzed for comparison with the conventionally obtained transients. In the second paragraph, the photon echo of NO_2 Rydberg states is extracted from the same data set and analyzed with respect to lineshapes arising in 2D spectroscopy of bound-continuum transitions.

6.5.1 Extraction of Pump–Probe Signals via Phase Cycling

Figure 6.5 (a) displays the time-domain signal of the ($\alpha = 0$, $\beta = 0$, $\gamma = 1$, $\delta = -1$) contribution for NO_2^+. The signal arises from two-photon excitation of NO_2 by the UV pump pulse into the 3d Rydberg states as discussed previously and subsequent probing by one photon via one interaction from probe pulse 3 ($\gamma = 1$) and one from probe pulse 4 ($\delta = -1$). The time-domain map exhibits a decay along the τ axis and evolves in a coherence during the time t with a strong signal during pulse overlap ($t \leq 20$ fs). The corresponding Feynman diagram is shown on the left-hand side of Fig. 6.5 (c) (green).

Since the first two probe pulses do not interact in this contribution, the initial population prepared by the UV pump pulse (black double arrows) decays without additional perturbation by these two pulses during the time intervals Δ, τ and T. The third probe pulse (green arrow) generates a coherence $|f\rangle\langle r|$ that evolves during t. Finally, the fourth probe pulse in the sequence prepares the final-state population leading to ionization. A one-dimensional Fourier transformation with respect to t can now be applied to retrieve the absorption spectrum at each τ delay and thus to generate a transient absorption map of the excited 3d Rydberg states, as shown in Fig. 6.5 (b). Additionally, the probe laser spectrum and the τ-integrated absorption spectrum is shown on the right-hand side. The NO_2^+ yield comprises a spectrally broad peak and decays as a function of τ, displaying the decay of the population in the two nearly degenerate 5^2A_1 and 6^2A_1 states and thus the dissociation of NO_2. The two states cannot be directly resolved, in particular since many transitions from these two states into the final-state manifold are possible resulting in a congested absorption profile.

For direct comparison with the conventional pump–probe data set the time-domain data [Fig. 6.5 (a)] is integrated over t. As the absolute signal levels of the conventional pump–probe trace and the integrated pump–probe contribution retrieved via phase cycling differ, the amplitude of the ($\alpha = 0$, $\beta = 0$, $\gamma =$

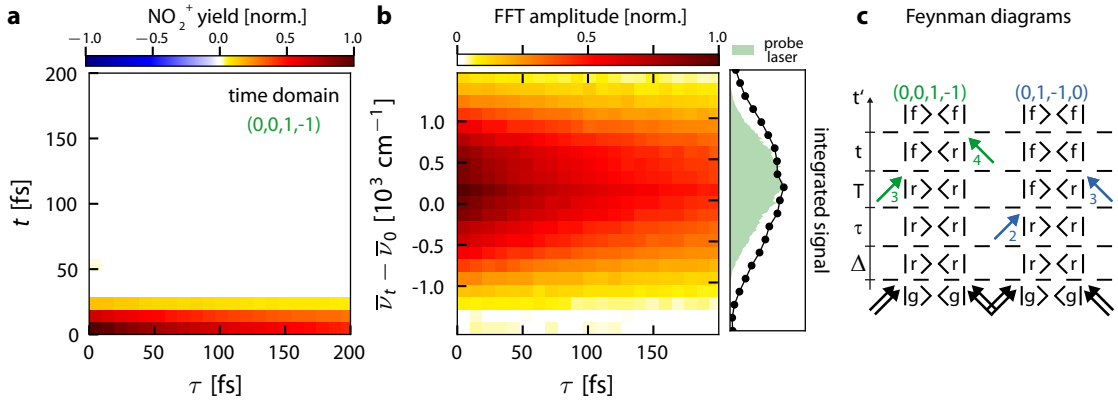

Figure 6.5: Pump–probe contributions obtained from phase cycling. (a) Time-domain data of (0, 0, 1, −1) contribution. The initial population prepared by the UV pump pulse can decay unperturbedly during coherence time τ. The third probe pulse creates a coherence that oscillates as a function of t. (b) Fourier transformation over t generates the transient absorption map of the prepared 3d Rydberg states (left), which can be integrated over the delay time τ (right). (c) Feynman diagrams for (0, 0, 1, −1) contribution (left) and (0, 1, −1, 0) contribution (right) illustrating the time ordering of interactions (colored arrows) for the two pump–probe signals starting from the ground state $|g\rangle$. The Rydberg states $|r\rangle$ are populated by the UV pump pulse (black arrows), the final state $|f\rangle$ by the probe pulses leading to ionization. Reproduced from Ref. [4].

1, $\delta = -1$) pump–probe contribution needs to be scaled to the amplitude of the conventional pump–probe contribution. The scaling factor is determined by minimizing the least square error between the ($\alpha = 0$, $\beta = 0$, $\gamma = 1$, $\delta = -1$) signal and the corresponding values of the fit to the conventional pump–probe trace. The conventional pump–probe signal obtained from scanning a mechanical delay line and the pump–probe signal acquired via phase cycling are compared in Fig. 6.6. Having set the population time $T = 30$ fs in the four-pulse sequence and $\Delta = 150$ fs, the third probe pulse arrives at a total delay of $(\Delta + T) = 180$ fs with respect to the UV pump pulse and is then shifted to larger delays by scanning τ (green arrow). This comparison between the conventionally obtained pump–probe signal (red) and the signal obtained from phase cycling (green) shows very good agreement, confirming the validity of of the phase-cycling approach.

In addition to this, other contributions with two interactions are conceivable. For example, in the ($\alpha = 0$, $\beta = 1$, $\gamma = -1$, $\delta = 0$) contribution, the first interaction is with the second pulse as shown in the Feynman diagram on the right-hand side of Fig. 6.5 (c). In this case, the coherence is prepared before the population time $T = 30$ fs is applied and is converted into a population with the

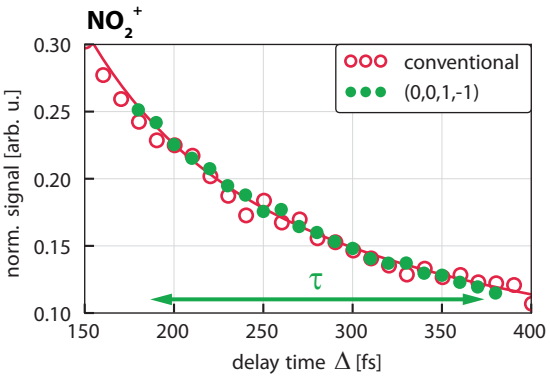

Figure 6.6: Pump–probe contribution obtained from phase cycling. Comparison of conventional pump–probe measurement (red circles: data, red line: fit) with pump–probe contribution (0, 0, 1, −1) (green dots) obtained from phase cycling. The effective scanning range for this contribution is indicated by the green arrow. Reproduced from Ref. [4].

third laser pulse at the constant delay of 30 fs. As can be inferred from the time evolution of the coherence along the t axis in Fig. 6.5 (a), the signal has already decayed to zero at this delay. Thus, a pump–probe signal cannot be retrieved for the given population time of $T = 30$ fs and the selected ($\alpha = 0$, $\beta = 1$, $\gamma = -1$, $\delta = 0$) contribution. It is worth to point out that transient dynamics can generally be recovered from this contribution for other population times shorter than 30 fs, however this was not measured due to the long integration times generally required for these experiments.

6.5.2 Photon Echo of NO_2 Rydberg States

In this paragraph, genuine transient 2D spectroscopy based on all four interactions with the shaped probe laser field is demonstrated. In particular, the rephasing ($\alpha = -1$, $\beta = 1$, $\gamma = 1$, $\delta = -1$) 2D signal is analyzed, for which the sign of the coherence is reversed after the third interaction with the visible probe field (Chap. 2.1.3). Figure 6.7 (a) displays the transient rephasing 2D spectrum of the NO_2^+ parent ion at a population time $T = 30$ fs. The signal originates from four interactions with the pump and four interactions with the probe laser field and is thus much weaker and suffers more strongly from experimental noise compared to the pump–probe contributions [six interactions in total, Fig. 6.5 (c)] and also to conventional 2D spectroscopy relying on third-order signals. Contributions with six or more visible interactions are expected to be even weaker and of no relevance in the case considered here.

Data Analysis

In order to aid identification of essential peak features, a Gaussian filter is applied to the raw rephasing time-domain data with a FWHM of 1.4 time pixels (corre-

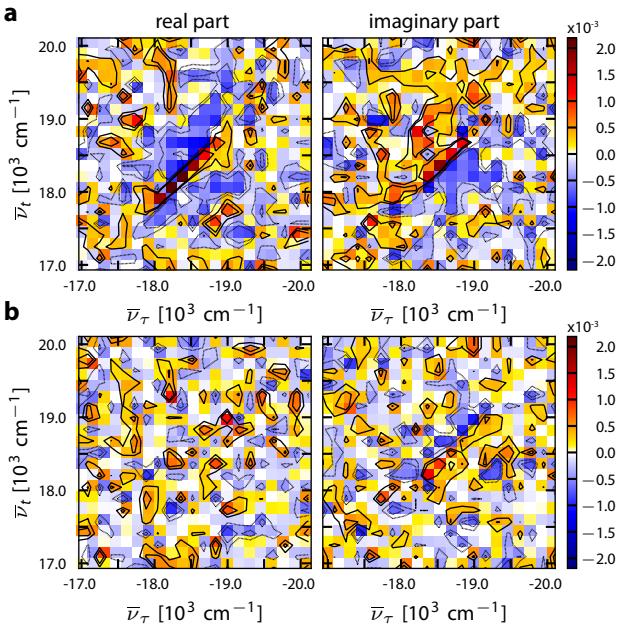

Figure 6.7: Comparison of rephasing NO_2^+ 2D spectrum with 2D spectrum of laser excitation. The excitation 2D spectrum is obtained with a photodiode placed at the laser focus position outside the chamber. Both measurements were conducted consecutively without any change in the setup. (a) NO_2^+ parent ion, featuring a nonlinear signal elongated along the diagonal as discussed in the main text. (b) Photodiode signal, displaying zero signal and thus ruling out the possibility of pulse shaper artifacts contributing to the signal of (a). Adapted and modified from Ref. [4].

sponding to 14 fs), thereby removing high-frequency contributions originating from experimental noise while retaining the essential peak appearance. This yields the rephasing 2D spectrum as shown in Fig. 6.10 (a). Such a procedure is justified in our case as the measurement has been performed in the rotating frame, shifting all frequencies to the origin of frequency space and allowing to remove high frequency components originating from experimental noise. For plotting, the rotating frame center frequency is added to the measured frequencies and the spectra are displayed with laboratory-frame frequency axes.

Furthermore, in Fig. 6.7 (b) the rephasing 2D spectrum is shown as obtained from a photodiode placed in the beam path outside the vacuum chamber by scanning the identical visible pulse sequence after the correction of the pulse-shaper nonlinearities (confer Chap. 3.2.2). It originates from a 2D Fourier transformation of the photodiode time-domain data in Fig. 3.8 (b) of Chap. 3.2.2. The measurement was performed immediately before the actual 2D experiment with no change in experimental settings. No residual rephasing signal can be identified in the photodiode 2D spectrum, meaning that nonlinear contributions to the signal of Fig. 6.7 (a) as introduced, e.g., by pulse shaper artifacts can be ruled out. Moreover, artifacts arising from stray-light contributions can be excluded as well, since the detection is based on non-optical signals. The NO_2^+ 2D spectrum arises solely from the amplitude of the parent ion mass peak and its dependence on the

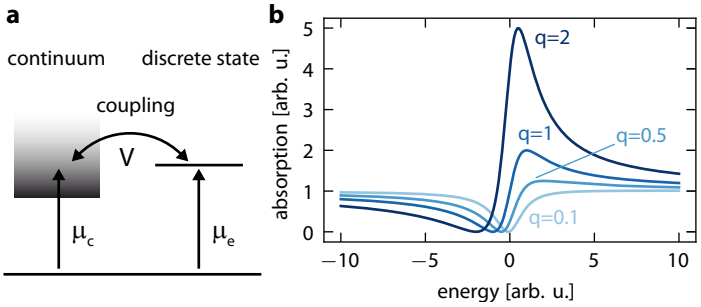

Figure 6.8: Fano model. (a) Schematic of a Fano-type model comprising a ground state and a discrete excited state coupled to a continuum of states. Allowed transitions are indicated by black arrows. (b) Absorption profiles for different values of the Fano-q parameter that is inverse proportional to the coupling strength V.

parameters of the four-pulse sequence (time delays and phases).

Discussion

The real part of the NO_2^+ 2D spectrum shows a signal elongated along the diagonal, with the peak shape being characteristic of a sample with large inhomogeneous broadening. For the given experimental conditions Doppler and pressure broadening are about four orders of magnitude smaller than the spectral resolution (159 cm^{-1}). Thus, the elongated signal shape is attributed to a multitude of unresolved vibronic transitions between the populated 3d Rydberg states and the energetically higher auto-ionizing final states or the ionic continuum.

The two pathways leading to the ionic continuum, direct ionization and absorption into a discrete auto-ionizing state, can interfere giving rise to an asymmetric lineshape of the absorption profile that depends on the coupling strength between the discrete state and the continuum [293] (Fig. 6.8). The coupling is expressed by the Fano-q parameter

$$q = \frac{\mu_e}{n\pi V \mu_c}\,, \tag{6.5.1}$$

where μ_e and μ_c are the transition dipoles to the discrete state and the continuum, respectively. The coupling is denoted by V and the density of continuum states by n. A large q parameter denotes weak coupling to the continuum and a dominating transition to the discrete excited state. In contrast, small q denotes either a strong direct transition from the ground state to the continuum or strong coupling via the discrete excited state. As demonstrated recently, the Fano-q parameter and hereby the absorption lineshape can be controlled and converted back to a Lorentzian absorption profile by an appropriate control laser field [294].

In coherent 2D spectroscopy Fano resonances also lead to distorted peak shapes

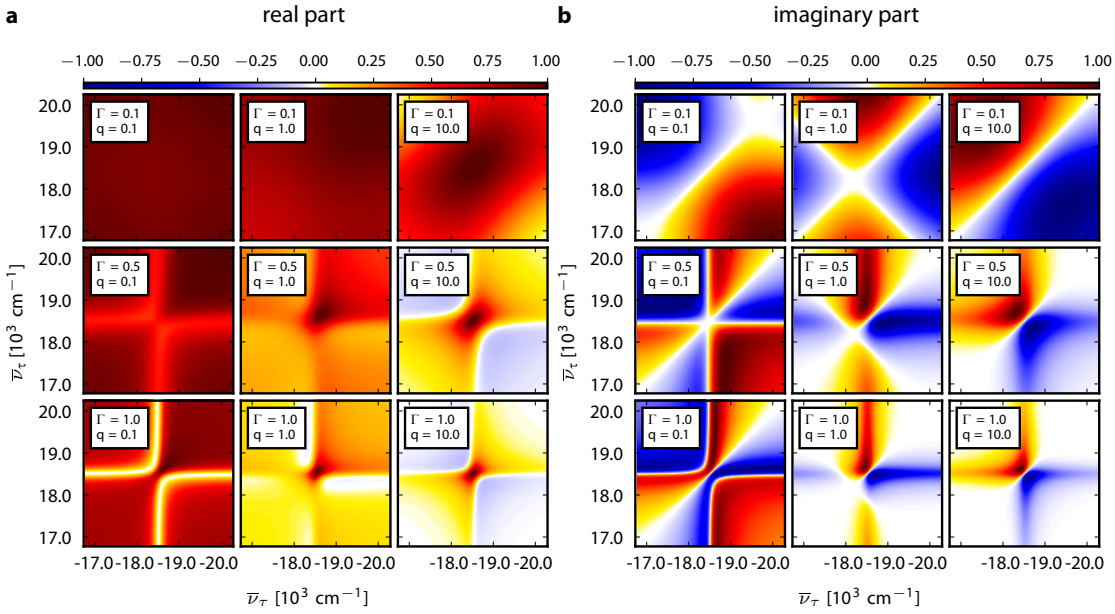

Figure 6.9: Rephasing 2D spectrum of the Fano model. Increasing values of the Fano-q parameter are plotted from left to right. The dissipation parameter Γ increases from top to bottom. In all cases, $\gamma_e = 160$ cm^{-1}. (a) Real part. (b) Imaginary part. Reproduced from Ref. [4].

as analyzed theoretically in a recent work [295] and studied experimentally for molecular layers on plasmonic arrays [71]. For a qualitative comparison with the NO_2^+ 2D spectrum, the model of Ref. [295] was used to calculate the lineshape of the rephasing contribution for different values of the Fano-q parameter. Furthermore, the parameter Γ is varied,

$$\Gamma = \frac{\gamma_e}{\gamma_e + \gamma} \qquad \in [0, 1]\,, \tag{6.5.2}$$

with γ_e denoting the dephasing of the coherences due to coupling to the continuum and γ denoting the pure dephasing due to the environment. Thus, Γ is a measure of the contribution of dissipation to the environment, with $\Gamma = 0$ ($\Gamma = 1$) indicating a relatively strong (weak) coupling to the bath. For a detailed derivation of analytical expressions for the rephasing and nonrephasing response functions the reader is referred to Ref. [295].

Both parameters, Γ and q, significantly influence the real part [Fig. 6.9 (a)] and the imaginary part [Fig. 6.9 (b)] of the rephasing signal in 2D spectroscopy.

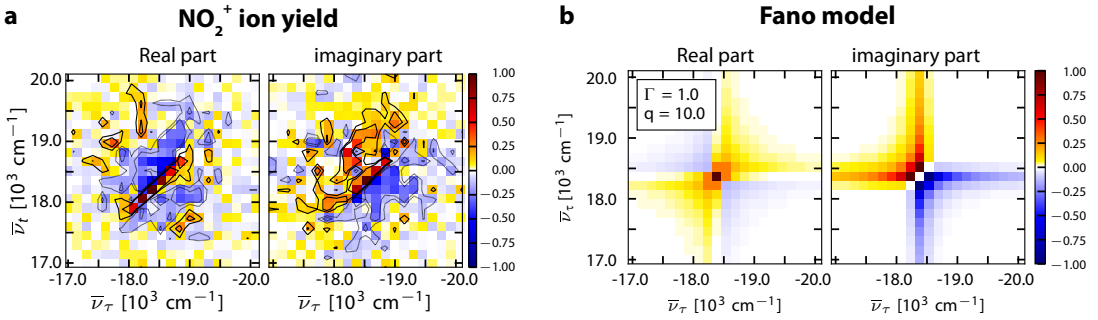

Figure 6.10: Comparison of experimental rephasing 2D spectrum and Fano model. (a) Experimental rephasing 2D spectrum of the NO_2^+ parent ion. (b) Simulated Fano 2D spectrum of best agreement with the experimental data. Here, $\Gamma = 1$ and $q = 10$, indicating a transition to a discrete state and no dissipation to the environment. Reproduced from Ref. [4].

For increasing q (left to right), the coupling to the continuum decreases, changing the asymmetric Fano lineshapes into Lorentzian-like lineshapes of discrete states. Additionally, for increasing Γ (top to bottom), the coupling to the environment is weaker and the linewidth decreases. In the case of strong coupling and thus fast dephasing of the coherences between the discrete auto-ionizing state and the Rydberg states, a spectrally broad peak is expected for the rephasing contribution that exhibits an asymmetric lineshape in the direction of the $\overline{\nu}_t = \overline{\nu}_\tau$ diagonal.

Comparing the different lineshapes of the Fano model with the rephasing NO_2^+ spectrum [Fig. 6.10] one can conclude that the lineshape observed in the experiment [Fig. 6.10 (a)] has most similarity with a Fano model comprising a large q parameter ($q = 10$). The correspondence is most easily established when considering first the imaginary part of the signal. The imaginary part of the measured data [Fig. 6.10 (a), right] has a node on the diagonal and negative (positive) signal below (above), which rules out Fano models with $q \leq 1$ [Fig. 6.9 (b)]. Additionally, the real part is narrow and elongated along the diagonal, favoring Γ close to unity [Fig. 6.10 (a)].

Therefore, the agreement is best with a model describing an isolated sample (as expected for a molecular beam) with weak coupling to the ionic continuum. Thus, a dominating transition from the prepared 3d Rydberg states into a discrete auto-ionizing state is likely the origin of the spectral shape observed in the experiment. While the 2D Fano model in Ref. [295] treats a single auto-ionizing state, multiple auto-ionizing states are expected in the case of NO_2. This case has not yet been elaborated in literature with respect to lineshapes in coherent 2D spectroscopy and remains an interesting direction for future studies of bound-continuum transitions.

For further investigation, an increased spectral resolution is beneficial to study the detailed peak shape and to resolve the transitions into the final states. However, this comparison already demonstrates that molecular-beam coherent 2D electronic spectroscopy can be a valuable tool for the investigation of Fano-type resonances.

6.6 Multiphoton-Ionization 2D Spectroscopy of NO_2

In the course of the experiments described in the previous sections, measurements using only the shaped visible pulse (and no UV pump pulse) were also performed that were motivated by the strong nonlinearity observed for multiphoton ionization with the visible pulse [Fig.6.4 (b)]. For the experiment discussed in this paragraph, the coherence times were scanned from 0 fs to 150 fs in 10 fs steps at a constant population time of $T = 100$ fs. Furthermore, the focus intensity was increased by expanding the beam by a factor of two in front of the focusing lens. In this configuration, the visible four-pulse sequence was intense enough to generate ions.

Due to the high nonlinearity of the ionization process, the applied $1 \times 3 \times 3 \times 3$ phase-cycling scheme is not sufficient to uniquely discriminate between the different ionization pathways. This means that the extracted fourth-order rephasing and nonrephasing contributions are generated from the sum of several indistinguishable higher-order Liouville paths. However, a separation of the different contributions is in principle possible and could provide interesting insight into multiphoton ionization if an adequate phase-cycling scheme is used at the cost of an increased measurement time. Nevertheless, the real and imaginary parts of the rephasing ($\alpha = -1$, $\beta = 1$, $\gamma = 1$, $\delta = -1$) and nonrephasing ($\alpha = 1$, $\beta = -1$, $\gamma = 1$, $\delta = -1$) 2D spectrum can be simultaneously retrieved for the parent ion and for the NO^+ fragment (Fig. 6.11). The 2D spectra of NO_2^+ and NO^+ show considerable differences in both contributions and have opposite signs in the real and imaginary parts. Whereas the real part of the NO_2^+ 2D spectrum has a negative peak in the rephasing contribution and displays positive features along the anti-diagonal, the real part of the NO^+ signal is positive and elongated along the diagonal with only weak features of opposite sign in the spectrum.

The difference in sign and shape is also preserved in the purely absorptive 2D spectra of each ion [Fig. 6.11 (c) and (f)] that are generated by adding the real parts of the rephasing and nonrephasing spectra, with the rephasing spectrum mirrored at the $\overline{\nu}_\tau = 0$ cm^{-1} axis [31]. The absorptive 2D spectrum of NO_2^+ has a more star-like peak shape with a small positive contribution at lower energies. In

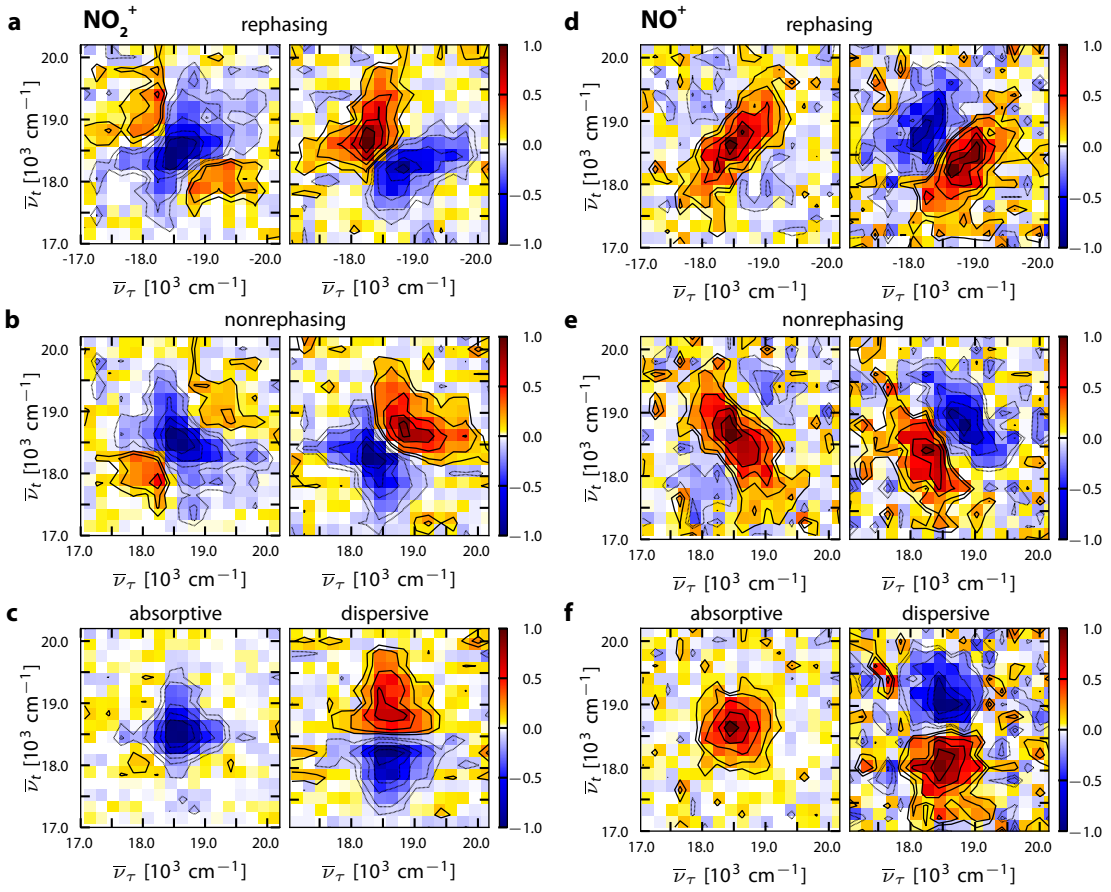

Figure 6.11: 2D spectra of NO_2^+ and NO^+ using only the visible pulses. The real part is shown on the left, the imaginary part on the right-hand side of each figure. (a) Rephasing 2D spectrum for the parent ion. (b) Nonrephasing 2D spectrum for the parent ion. (c) Absorptive and dispersive 2D spectrum for the parent ion. (d) Rephasing 2D spectrum for the NO^+ fragment. (e) Nonrephasing 2D spectrum for the NO^+ fragment. (f) Absorptive and dispersive 2D spectrum for the NO^+ fragment. Adapted and modified from Ref. [4].

contrast, the NO^+ absorptive 2D spectrum is purely positive and has a broader, round shape.

If both ions originated from the same response function ending in a highly-excited final state and leading to ion-pair formation or direct ionization as discussed previously, one would expect identical signs and the same peak shape in both signals because the NO_2^+ and the NO^+ yields would just be measures of the same final-state population. In contrast to that, the observed differences for both ions indicate that the NO_2^+ and NO^+ 2D spectra likely originate from different nonlinear response functions. For example, fragmentation can take place at an

intermediate level by multiphoton excitation of NO_2 within the first two pulses followed by subsequent dissociation during the waiting time $T = 100$ fs and ionization with pulses three and four. This leads to an increased and thus positive NO^+ product signal and a depleted, hence negative, NO_2^+ reactant signal, similar to product absorption and bleach signals in transient absorption.

This example illustrates the simultaneous acquisition of reactant and product 2D spectra in a gas-phase photochemical reaction and reveals their individual nonlinear response functions, which is not feasible using just pump–probe spectroscopy.

6.7 Conclusion

The work presented in this chapter demonstrates the first example of mass-selective molecular-beam coherent 2D electronic spectroscopy in literature. The novel technique was used to study the (multiphoton) ionization of NO_2 and verified by comparing pump–probe like contributions obtained via phase cycling with pump–probe data using a conventional delay line. Lineshape analysis of the NO_2^+ rephasing 2D spectrum and qualitative comparison to a 2D Fano model identified transitions into auto-ionizing states as the major probe step for 3d Rydberg states pumped by two-photon absorption. Moreover, molecular-beam 2D electronic spectroscopy is also applicable for the study of multiphoton ionization processes and may uncover the role of resonant intermediate states if an adequate phase-cycling scheme is applied.

Spreading the information content of time-resolved mass spectrometry over two additional frequency dimensions generally provides means to extract coherent information and to dissect transition states and hidden couplings in gas-phase photophysics and photochemistry. It further enables to follow the evolution of coherences during bond breakage or isomerization and facilitates comparison with complementary liquid-phase 2D spectroscopy and theoretical calculations, rendering it possible to study in detail the role of the environment during primary steps of photochemistry.

7 | Summary

Time-resolved spectroscopy offers a variety of methods for the investigation of ultrafast dynamics in physics, chemistry, and biology. Among those, pump–probe and transient-absorption spectroscopy have been widely used in all states of matter for the study of excited-state dynamics and reaction pathways in photochemistry. In the last decade, coherent multidimensional spectroscopy has emerged as an extension to transient absorption and unravels coherent information that was not accessible before. Starting with experimental realizations that required delicate alignment of many optical components, the use of pulse shapers greatly simplified the setups and accelerated the acquisition, making the technique available to a broader community. In order to increase the range of applications, a uniform approach is desired that allows to investigate samples in different environments with the same method, thereby maintaining comparability of results.

The aim of this work was to realize rapid-scanning multidimensional electronic spectroscopy in a fully collinear geometry utilizing incoherent observables for detection. Using a pulse shaper that is capable of updating the output pulse shape at the repetition rate of the laser enables fast scanning and permits to apply optimized non-uniform sampling procedures that are superior to conventional techniques in terms of acquisition time. Flexibility on the choice of observable is granted by the collinear approach, since the pulse shaper output can be easily routed to different endstations and permits to study samples in various states of matter from condensed phase to the gas phase.

Rapid-scanning multidimensional electronic spectroscopy was successfully implemented for liquid samples and is described in Chap. 4, where the fluorescence of the laser dye cresyl violet dissolved in ethanol was used as an observable of the excited-state population that was generated by the interaction with a sequence of four incident laser pulses. Controlling the phase of the individual laser pulses via the pulse shaper enabled to separate several nonlinear fluorescence contributions during data analysis (phase cycling) and was employed here to extract the ab-

sorptive 2D spectrum of the studied sample. Quantum beatings originating from vibrational coherences were observed in the 2D spectra as a function of the population time T and are in accord with previous findings in literature. Furthermore, the performance of the setup in terms of signal-to-noise ratio was assessed by comparing 2D spectra for various amounts of averaging, revealing that averaging a 2D spectrum over 20 laser shots is in this case sufficient to extract the signal characteristics. Therefore, a 2D spectrum for a given population time can be obtained within 2 minutes of acquisition time.

In Chap. 5, ideas of non-uniform undersampling in nuclear-magnetic resonance (NMR) were adopted and applied to multidimensional electronic spectroscopy with the aim to reduce the data to be acquired while retaining the essential information content of the resulting multidimensional spectrum. More specifically, by using a genetic algorithm an optimal time-domain sampling pattern was found that permits to use only 25 % of the data points from conventional sampling. The new acquisition concept relies on signal reconstruction of optimally sampled data with a compressed-sensing reconstruction algorithm. This approach was demonstrated by recovering the quantum beatings observed in cresyl violet from an undersampled data set. Successful reconstruction is facilitated by a compact time-frequency representation of 2D spectra based on a 2D extension of the von Neumann basis (2DvN). It was shown that the essential information of a 2D spectrum is concentrated in only 5 % of 2DvN basis coefficients, whereas it takes about 30 % of Fourier coefficients to fully represent the signal. Moreover, the 2DvN representation appeared to be suitable for efficient denoising of conventional 2D spectra by condensing the data to a few relevant coefficients, thereby removing noise otherwise added by the discarded data points. In future applications, a pulse train capable of directly measuring the most relevant 2DvN coefficients would significantly speed up acquisition times, permitting new types of 2D spectroscopy experiments that follow reaction dynamics proceeding on a timescale of a few seconds.

As the main result of this work, molecular-beam coherent 2D electronic spectroscopy was realized in Chap. 6 in order to acquire 2D spectra of molecules in the gaseous phase. The new technique combines for the first time pulse-shaper assisted rapid scanning with cation detection in a time-of-flight mass spectrometer. This enables not only to exploit the advantages of narrow linewidths in isolated samples but also permits direct and simultaneous detection of reaction products emerging from photo-excitation with a phase-coherent multipulse sequence. This new variant of 2D spectroscopy was applied in order to study ionization pathways of highly-excited nitrogen dioxide (NO_2) by analyzing the lineshape of the observed 2D spectrum and revealed transitions into auto-ionizing states as the major contri-

bution to the observed ion signal. Furthermore, 2D spectroscopy of multiphoton ionization exposed distinct differences in the 2D spectra of the parent ion and its fragment and may in principle uncover the role of resonant intermediate states with a modified phase-cycling scheme. Ongoing work on the mass spectrometer includes the implementation of a cold seeded gas jet obtained from a supersonic expansion that will yield improved signals by increasing the sample density in the interaction region. Furthermore, the cold beam will extend the range of possible molecules that can be investigated in the gaseous phase with 2D spectroscopy in future experiments.

The work presented in this thesis advances 2D electronic spectroscopy by putting experimental approaches to investigate samples in different states of matter on common ground. Moreover, molecular-beam coherent 2D spectroscopy has been established in this work, using cations for the first time as an observable in 2D spectroscopy. With the introduction of optimized sampling first steps have been taken to conduct multidimensional spectroscopy experiments using methods of modern signal processing that will help to shorten acquisition times while keeping the same information content. Together, the new developments enable direct comparison of observed photodynamics in different environments and will help to unravel the role of quantum-mechanical coherence in photoinduced processes.

Bibliography

[1] S. Draeger, S. Roeding, and T. Brixner, "Rapid-scan coherent 2D fluorescence spectroscopy", Opt. Express **25**, 3259–3267 (2017).

[2] S. Roeding, N. Klimovich, and T. Brixner, "Optimizing sparse sampling for 2D electronic spectroscopy", J. Chem. Phys. **146**, 084201 (2017).

[3] S. Roeding and T. Brixner, "Multidimensional electronic spectroscopy in molecular beams with mass-resolved ion detection", in "International Conference on Ultrafast Phenomena XX," (Optical Society of America, 2016), p. UM3A.2.

[4] S. Roeding and T. Brixner, "Molecular-beam coherent 2D electronic spectroscopy reveals photoionization pathways", Submitted for publication. (2017).

[5] A. Steinbacher, S. Roeding, T. Brixner, and P. Nuernberger, "Ultrafast photofragment ion spectroscopy of the Wolff rearrangement in 5-diazo Meldrum's acid", Phys. Chem. Chem. Phys. **16**, 7290–7298 (2014).

[6] A. Steinbacher, S. Roeding, T. Brixner, and P. Nuernberger, "The ultrafast Wolff rearrangement in the gas phase", in "Ultrafast Phenomena XIX," , K. Yamanouchi, S. Cundiff, R. d. Vivie-Riedle, M. Kuwata-Gonokami, and L. DiMauro, eds. (Springer International Publishing, 2015), no. 162 in Springer Proceedings in Physics, pp. 180–183.

[7] L. J. Rothschild and R. L. Mancinelli, "Life in extreme environments", Nature **409**, 1092–1101 (2001).

[8] R. Croce and H. van Amerongen, "Natural strategies for photosynthetic light harvesting", Nature Chemical Biology **10**, 492–501 (2014).

[9] W. H. Wollaston, "A method of examining refractive and dispersive powers, by prismatic reflection", Phil. Trans. R. Soc. Lond. **92**, 365–380 (1802).

[10] J. Fraunhofer, "Bestimmung des Brechungs- und Farbenzerstreuungs-Vermögens verschiedener Glasarten, in Bezug auf die Vervollkommnung achromatischer Fernröhre", Denkschr. Akad. Wiss. München **5**, 193–226 (1817).

[11] G. Kirchhoff, "Ueber die Fraunhofer'schen Linien", Ann. Phys. **185**, 148–150 (1860).

[12] M. Eigen, "Methods for investigation of ionic reactions in aqueous solutions with half-times as short as 10^{-9} sec. Application to neutralization and hydrolysis reactions", Discuss. Faraday Soc. **17**, 194–205 (1954).

[13] R. G. W. Norrish and G. Porter, "Chemical reactions produced by very high light intensities", Nature **164**, 658 (1949).

[14] A. H. Zewail, "Femtochemistry: Atomic-scale dynamics of the chemical bond", J. Phys. Chem. A **104**, 5660–5694 (2000).

[15] J. L. Martin and M. H. Vos, "Femtosecond biology", Annu. Rev. Biophys. **21**, 199–222 (1992).

[16] W. Zinth and J. Wachtveitl, "The first picoseconds in bacterial photosynthesis—ultrafast electron transfer for the efficient conversion of light energy", ChemPhysChem **6**, 871–880 (2005).

[17] R. Schoenlein, L. Peteanu, R. A. Mathies, and C. V. Shank, "The first step in vision: Femtosecond isomerization of rhodopsin", Science **254**, 412–415 (1991).

[18] F. Schotte, M. Lim, T. A. Jackson, A. V. Smirnov, J. Soman, J. S. Olson, G. N. Phillips, M. Wulff, and P. A. Anfinrud, "Watching a protein as it functions with 150-ps time-resolved X-ray crystallography", Science **300**, 1944–1947 (2003).

[19] M. Hentschel, R. Kienberger, C. Spielmann, G. A. Reider, N. Milosevic, T. Brabec, P. Corkum, U. Heinzmann, M. Drescher, and F. Krausz, "Attosecond metrology", Nature **414**, 509–513 (2001).

[20] M. Dantus, M. H. M. Janssen, and A. H. Zewail, "Femtosecond probing of molecular dynamics by mass-spectrometry in a molecular beam", Chem. Phys. Lett. **181**, 281–287 (1991).

[21] T. Baumert, M. Grosser, R. Thalweiser, and G. Gerber, "Femtosecond time-resolved molecular multiphoton ionization: The Na_2 system", Phys. Rev. Lett. **67**, 3753–3756 (1991).

[22] A. Assion, M. Geisler, J. Helbing, V. Seyfried, and T. Baumert, "Femtosecond pump-probe photoelectron spectroscopy: Mapping of vibrational wave-packet motion", Phys. Rev. A **54**, R4605–R4608 (1996).

[23] G. S. Engel, T. R. Calhoun, E. L. Read, T.-K. Ahn, T. Mančal, Y.-C. Cheng, R. E. Blankenship, and G. R. Fleming, "Evidence for wavelike energy transfer through quantum coherence in photosynthetic systems", Nature **446**, 782–786 (2007).

[24] J.M. Anna, Gregory D. Scholes, and R. van Grondelle, "A little coherence in photosynthetic light harvesting", Bioscience **64** (2014).

[25] S. M. Falke, C. A. Rozzi, D. Brida, M. Maiuri, M. Amato, E. Sommer, A. D. Sio, A. Rubio, G. Cerullo, E. Molinari, and C. Lienau, "Coherent ultrafast charge transfer in an organic photovoltaic blend", Science **344**, 1001–1005 (2014).

[26] G. D. Scholes, G. R. Fleming, L. X. Chen, A. Aspuru-Guzik, A. Buchleitner, D. F. Coker, G. S. Engel, R. van Grondelle, A. Ishizaki, D. M. Jonas, J. S. Lundeen, J. K. McCusker, S. Mukamel, J. P. Ogilvie, A. Olaya-Castro, M. A. Ratner, F. C. Spano, K. B. Whaley, and X. Zhu, "Using coherence to enhance function in chemical and biophysical systems", Nature **543**, 647–656 (2017).

[27] A. De Sio and C. Lienau, "Vibronic coupling in organic semiconductors for photovoltaics", Phys. Chem. Chem. Phys. **19**, 18813–18830 (2017).

[28] S. T. Cundiff and S. Mukamel, "Optical multidimensional coherent spectroscopy", Phys. Today **66**, 44–49 (2013).

[29] S. Mukamel, *Principles of nonlinear optical spectroscopy* (Oxford University Press, New York, 1995), 1st ed.

[30] M. Cho, *Two-dimensional optical spectroscopy* (CRC Press, Boca Raton, FL, 2009).

[31] P. Hamm and M. Zanni, *Concepts and methods of 2D infrared spectroscopy* (Cambridge University Press, New York, 2011), 1st ed.

[32] D. M. Jonas, "Two-dimensional femtosecond spectroscopy", Annu. Rev. Phys. Chem. **54**, 425–463 (2003).

[33] R. M. Hochstrasser, "Two-dimensional spectroscopy at infrared and optical frequencies", PNAS **104**, 14190–14196 (2007).

[34] M. Cho, "Coherent two-dimensional optical spectroscopy", Chem. Rev. **108**, 1331–1418 (2008).

[35] J. P. Ogilvie and K. J. Kubarych, "Multidimensional electronic and vibrational spectroscopy: An ultrafast probe of molecular relaxation and reaction dynamics", in "Advances In Atomic, Molecular, and Optical Physics," , vol. 57 (Academic Press, 2009), pp. 249–321.

[36] A. M. Brańczyk, D. B. Turner, and G. D. Scholes, "Crossing disciplines - A view on two-dimensional optical spectroscopy", Ann. Phys. **526**, 31–49 (2014).

[37] F. D. Fuller and J. P. Ogilvie, "Experimental implementations of two-dimensional Fourier transform electronic spectroscopy", Annu. Rev. Phys. Chem. **66**, 667–690 (2015).

[38] C. Cohen-Tannoudji, B. Diu, and F. Laloe, *Quantum mechanics, volume 2* (Wiley-VCH, New York; Paris, 1991), 1st ed.

[39] J. J. Sakurai, *Modern quantum mechanics* (Addison Wesley, 1993), rev. ed.

[40] B. H. Bransden and C. J. Joachain, *Physics of atoms and molecules* (Pearson Education, 2003).

[41] J. D. Jackson, *Classical electrodynamics* (Wiley & Sons, 1999), 3rd ed.

[42] H. Haken and H. C. Wolf, *Molekülphysik und Quantenchemie: Einführung in die experimentellen und theoretischen Grundlagen* (Springer-Verlag, Berlin, 2006), 5th ed.

[43] P. W. Atkins and R. S. Friedman, *Molecular quantum mechanics* (Oxford University Press, Oxford ; New York, 2010), 5th ed.

[44] H. Stapelfeldt and T. Seideman, "Colloquium: Aligning molecules with strong laser pulses", Rev. Mod. Phys. **75**, 543–557 (2003).

[45] L. Holmegaard, J. L. Hansen, L. Kalhøj, S. Louise Kragh, H. Stapelfeldt, F. Filsinger, J. Küpper, G. Meijer, D. Dimitrovski, M. Abu-samha, C. P. J. Martiny, and L. Bojer Madsen, "Photoelectron angular distributions from strong-field ionization of oriented molecules", Nat. Phys. **6**, 428–432 (2010).

[46] T. Brixner, G. Krampert, T. Pfeifer, R. Selle, G. Gerber, M. Wollenhaupt, O. Graefe, C. Horn, D. Liese, and T. Baumert, "Quantum control by ultrafast polarization shaping", Phys. Rev. Lett. **92**, 208301 (2004).

[47] G. A. Lott, A. Perdomo-Ortiz, J. K. Utterback, J. R. Widom, A. Aspuru-Guzik, and A. H. Marcus, "Conformation of self-assembled porphyrin dimers in liposome vesicles by phase-modulation 2D fluorescence spectroscopy", PNAS **108**, 16521–16526 (2011).

[48] A. Perdomo-Ortiz, J. R. Widom, G. A. Lott, A. Aspuru-Guzik, and A. H. Marcus, "Conformation and electronic population transfer in membrane-supported self-assembled porphyrin dimers by 2D fluorescence spectroscopy", J. Phys. Chem. B **116**, 10757–10770 (2012).

[49] K. J. Karki, J. R. Widom, J. Seibt, I. Moody, M. C. Lonergan, T. Pullerits, and A. H. Marcus, "Coherent two-dimensional photocurrent spectroscopy in a PbS quantum dot photocell", Nat. Commun. **5**, 5869 (2014).

[50] S. Mukamel and M. Richter, "Multidimensional phase-sensitive single-molecule spectroscopy with time-and-frequency-gated fluorescence detection", Phys. Rev. A **83**, 013815 (2011).

[51] W. P. Aue, E. Bartholdi, and R. R. Ernst, "Two-dimensional spectroscopy. Application to nuclear magnetic resonance", J. Chem. Phys. **64**, 2229–2246 (1976).

[52] D. Keusters, H.-S. Tan, and W. S. Warren, "Role of pulse phase and direction in two-dimensional optical spectroscopy", J. Phys. Chem. A **103**, 10369–10380 (1999).

[53] J. D. Hybl, A. Albrecht Ferro, and D. M. Jonas, "Two-dimensional Fourier transform electronic spectroscopy", J. Chem. Phys. **115**, 6606 (2001).

[54] M. E. Siemens, G. Moody, H. Li, A. D. Bristow, and S. T. Cundiff, "Resonance lineshapes in two-dimensional Fourier transform spectroscopy", Opt. Express **18**, 17699–17708 (2010).

[55] A. Tokmakoff, "Two-dimensional line shapes derived from coherent third-order nonlinear spectroscopy", J. Phys. Chem. A **104**, 4247–4255 (2000).

[56] J. D. Hybl, Y. Christophe, and D. M. Jonas, "Peak shapes in femtosecond 2D correlation spectroscopy", Chem. Phys. **266**, 295–309 (2001).

[57] M. Khalil, N. Demirdöven, and A. Tokmakoff, "Obtaining absorptive line shapes in two-dimensional infrared vibrational correlation spectra", Phys. Rev. Lett. **90** (2003).

[58] P. Tian, D. Keusters, Y. Suzaki, and W. S. Warren, "Femtosecond phase-coherent two-dimensional spectroscopy", Science **300**, 1553–1555 (2003).

[59] H.-S. Tan, "Theory and phase-cycling scheme selection principles of collinear phase coherent multi-dimensional optical spectroscopy", J. Chem. Phys. **129**, 124501 (2008).

[60] T. Brixner, J. Stenger, H. M. Vaswani, M. Cho, R. E. Blankenship, and G. R. Fleming, "Two-dimensional spectroscopy of electronic couplings in photosynthesis", Nature **434**, 625–628 (2005).

[61] A. F. Fidler, V. P. Singh, P. D. Long, P. D. Dahlberg, and G. S. Engel, "Dynamic localization of electronic excitation in photosynthetic complexes revealed with chiral two-dimensional spectroscopy", Nat. Commun. **5** (2014).

[62] F. Fassioli, R. Dinshaw, P. C. Arpin, and G. D. Scholes, "Photosynthetic light harvesting: excitons and coherence", J. R. Soc. Interface **11**, 20130901 (2014).

[63] J. Dostál, J. Pšenčík, and D. Zigmantas, "In situ mapping of the energy flow through the entire photosynthetic apparatus", Nat. Chem. **8**, 705–710 (2016).

[64] K. W. Stone, K. Gundogdu, D. B. Turner, X. Li, S. T. Cundiff, and K. A. Nelson, "Two-quantum 2D FT electronic spectroscopy of biexcitons in GaAs quantum wells", Science **324**, 1169–1173 (2009).

[65] G. Nardin, T. M. Autry, K. L. Silverman, and S. T. Cundiff, "Multidimensional coherent photocurrent spectroscopy of a semiconductor nanostructure", Opt. Express **21**, 28617–28627 (2013).

[66] R. D. Mehlenbacher, T. J. McDonough, M. Grechko, M.-Y. Wu, M. S. Arnold, and M. T. Zanni, "Energy transfer pathways in semiconducting carbon nanotubes revealed using two-dimensional white-light spectroscopy", Nat. Commun. **6**, 6732 (2015).

[67] E. Vella, H. Li, P. Grégoire, S. M. Tuladhar, M. S. Vezie, S. Few, C. M. Bazán, J. Nelson, C. Silva-Acuña, and E. R. Bittner, "Ultrafast decoherence dynamics govern photocarrier generation efficiencies in polymer solar cells", Sci. Rep. **6**, 29437 (2016).

[68] G. Moody and S. T. Cundiff, "Advances in multi-dimensional coherent spectroscopy of semiconductor nanostructures", Adv. Phys. X **2**, 641–674 (2017).

[69] M. Aeschlimann, T. Brixner, A. Fischer, C. Kramer, P. Melchior, W. Pfeiffer, C. Schneider, C. Strüber, P. Tuchscherer, and D. V. Voronine, "Coherent two-dimensional nanoscopy", Science **333**, 1723–1726 (2011).

[70] M. Aeschlimann, T. Brixner, D. Differt, U. Heinzmann, M. Hensen, C. Kramer, F. Lükermann, P. Melchior, W. Pfeiffer, M. Piecuch, C. Schneider, H. Stiebig, C. Strüber, and P. Thielen, "Perfect absorption in nanotextured thin films via Anderson-localized photon modes", Nat. Photonics **9**, 663–668 (2015).

[71] A. Gandman, R. Mackin, B. Cohn, I. V. Rubtsov, and L. Chuntonov, "Two-dimensional Fano lineshapes in ultrafast vibrational spectroscopy of thin molecular layers on plasmonic arrays", J. Phys. Chem. Lett. **8**, 3341–3346 (2017).

[72] J. R. Widom, W. Lee, A. Perdomo-Ortiz, D. Rappoport, T. F. Molinski, A. Aspuru-Guzik, and A. H. Marcus, "Temperature-dependent conformations of a membrane supported zinc porphyrin tweezer by 2D fluorescence spectroscopy", J. Phys. Chem. A (2013).

[73] T. Unger, F. Panzer, C. Consani, F. Koch, T. Brixner, H. Bässler, and A. Köhler, "Ultrafast energy transfer between disordered and highly planarized chains of poly[2-methoxy-5-(2-ethylhexyloxy)-1,4-phenylenevinylene] (MEH-PPV)", ACS Macro Lett. **4**, 412–416 (2015).

[74] S. Ruetzel, M. Diekmann, P. Nuernberger, C. Walter, B. Engels, and T. Brixner, "Multidimensional spectroscopy of photoreactivity", PNAS **111**, 4764–4769 (2014).

[75] P. Nuernberger, S. Ruetzel, and T. Brixner, "Multidimensional electronic spectroscopy of photochemical reactions", Angew. Chem. Int. Ed. **54**, 11368–11386 (2015).

[76] W. P. Aue, E. Bartholdi, and R. R. Ernst, "Two-dimensional spectroscopy. Application to nuclear magnetic resonance", J. Chem. Phys. **64**, 2229–2246 (1976).

[77] P. Hamm, M. Lim, and R. M. Hochstrasser, "Structure of the amide I band of peptides measured by femtosecond nonlinear-infrared spectroscopy", J. Phys. Chem. B **102**, 6123–6138 (1998).

[78] M. C. Asplund, M. T. Zanni, and R. M. Hochstrasser, "Two-dimensional infrared spectroscopy of peptides by phase-controlled femtosecond vibrational photon echoes", PNAS **97**, 8219–8224 (2000).

[79] S. Woutersen and P. Hamm, "Structure determination of trialanine in water using polarization sensitive two-dimensional vibrational spectroscopy", J. Phys. Chem. B **104**, 11316–11320 (2000).

[80] O. Golonzka, M. Khalil, N. Demirdöven, and A. Tokmakoff, "Vibrational anharmonicities revealed by coherent two-dimensional infrared spectroscopy", Phys. Rev. Lett. **86**, 2154–2157 (2001).

[81] J. D. Hybl, A. W. Albrecht, S. M. Gallagher Faeder, and D. M. Jonas, "Two-dimensional electronic spectroscopy", Chem. Phys. Lett. **297**, 307–313 (1998).

[82] T. Brixner, T. Mančal, I. V. Stiopkin, and G. R. Fleming, "Phase-stabilized two-dimensional electronic spectroscopy", J. Chem. Phys. **121**, 4221–4236 (2004).

[83] M. L. Cowan, J. P. Ogilvie, and R. J. D. Miller, "Two-dimensional spectroscopy using diffractive optics based phased-locked photon echoes", Chem. Phys. Lett. **386**, 184–189 (2004).

[84] T. Brixner, I. V. Stiopkin, and G. R. Fleming, "Tunable two-dimensional femtosecond spectroscopy", Opt. Lett. **29**, 884–886 (2004).

[85] U. Selig, F. Langhojer, F. Dimler, T. Löhrig, C. Schwarz, B. Gieseking, and T. Brixner, "Inherently phase-stable coherent two-dimensional spectroscopy using only conventional optics", Opt. Lett. **33**, 2851–2853 (2008).

[86] J. A. Myers, K. L. Lewis, P. F. Tekavec, and J. P. Ogilvie, "Two-color two-dimensional Fourier transform electronic spectroscopy with a pulse-shaper", Opt. Express **16**, 17420–17428 (2008).

[87] D. Zimdars, R. S. Francis, C. Ferrante, and M. D. Fayer, "Electronic dephasing in nonpolar room temperature liquids: UV photon echo pulse duration dependent measurements", J. Chem. Phys. **106**, 7498 (1997).

[88] A. Ajdarzadeh Oskouei, O. Bräm, A. Cannizzo, F. van Mourik, A. Tortschanoff, and M. Chergui, "Photon echo peak shift experiments in the UV: p-terphenyl in different solvents", J. Mol. Liq. **141**, 118–123 (2008).

[89] C.-H. Tseng, S. Matsika, and T. C. Weinacht, "Two-dimensional ultrafast Fourier transform spectroscopy in the deep ultraviolet", Opt. Express **17**, 18788–18793 (2009).

[90] U. Selig, C.-F. Schleussner, M. Foerster, F. Langhojer, P. Nuernberger, and T. Brixner, "Coherent two-dimensional ultraviolet spectroscopy in fully non-collinear geometry", Opt. Lett. **35**, 4178–4180 (2010).

[91] B. A. West and A. M. Moran, "Two-dimensional electronic spectroscopy in the ultraviolet wavelength range", J. Phys. Chem. Lett. **3**, 2575–2581 (2012).

[92] W. Kuehn, K. Reimann, M. Woerner, T. Elsaesser, and R. Hey, "Two-dimensional terahertz correlation spectra of electronic excitations in semiconductor quantum wells", J. Phys. Chem. B **115**, 5448–5455 (2011).

[93] M. Woerner, W. Kuehn, P. Bowlan, K. Reimann, and T. Elsaesser, "Ultrafast two-dimensional terahertz spectroscopy of elementary excitations in solids", New J. Phys. **15**, 025039 (2013).

[94] J. Lu, Y. Zhang, H. Y. Hwang, B. K. Ofori-Okai, S. Fleischer, and K. A. Nelson, "Nonlinear two-dimensional terahertz photon echo and rotational spectroscopy in the gas phase", PNAS **113**, 11800–11805 (2016).

[95] S. Rahav and S. Mukamel, "Multidimensional attosecond photoelectron spectroscopy with shaped pulses and quantum optical fields", Phys. Rev. A **81**, 063810 (2010).

[96] S. Mukamel, D. Healion, Y. Zhang, and J. D. Biggs, "Multidimensional attosecond resonant X-ray spectroscopy of molecules: Lessons from the optical regime", Annu. Rev. Phys. Chem. **64**, 101–127 (2013).

[97] K. Bennett, Y. Zhang, M. Kowalewski, W. Hua, and S. Mukamel, "Multidimensional resonant nonlinear spectroscopy with coherent broadband x-ray pulses", Phys. Scr. **2016**, 014002 (2016).

[98] J.-C. Diels and W. Rudolph, *Ultrashort laser pulse phenomena: Fundamentals, techniques, and applications on a femtosecond time scale* (Academic Press Inc, 1996), 2nd ed.

[99] R. W. Boyd, *Nonlinear optics* (Academic Press, Burlington, 2008), 3rd ed.

[100] L. Lepetit, G. Chériaux, and M. Joffre, "Linear techniques of phase measurement by femtosecond spectral interferometry for applications in spectroscopy", J. Opt. Soc. Am. B **12**, 2467–2474 (1995).

[101] R. M. Hochstrasser, "Two-dimensional IR-spectroscopy: polarization anisotropy effects", Chem. Phys. **266**, 273–284 (2001). 00161.

[102] E. L. Read, G. S. Engel, T. R. Calhoun, T. Mancal, T. K. Ahn, R. E. Blankenship, and G. R. Fleming, "Cross-peak-specific two-dimensional electronic spectroscopy", PNAS **104**, 14203–14208 (2007).

[103] E. M. Grumstrup, S.-H. Shim, M. A. Montgomery, N. H. Damrauer, and M. T. Zanni, "Facile collection of two-dimensional electronic spectra using femtosecond pulse-shaping technology", Opt. Express **15**, 16681–16689 (2007).

[104] S.-H. Shim and M. T. Zanni, "How to turn your pump–probe instrument into a multidimensional spectrometer: 2D IR and VIS spectroscopies via pulse shaping", Phys. Chem. Chem. Phys. **11**, 748–761 (2009).

[105] P. F. Tekavec, J. A. Myers, K. L. M. Lewis, and J. P. Ogilvie, "Two-dimensional electronic spectroscopy with a continuum probe", Opt. Lett. **34**, 1390–1392 (2009).

[106] L. P. DeFlores, R. A. Nicodemus, and A. Tokmakoff, "Two-dimensional Fourier transform spectroscopy in the pump-probe geometry", Opt. Lett. **32**, 2966–2968 (2007).

[107] D. Brida, C. Manzoni, and G. Cerullo, "Phase-locked pulses for two-dimensional spectroscopy by a birefringent delay line", Opt. Lett. **37**, 3027 (2012).

[108] P. F. Tekavec, G. A. Lott, and A. H. Marcus, "Fluorescence-detected two-dimensional electronic coherence spectroscopy by acousto-optic phase modulation", J. Chem. Phys. **127**, 214307 (2007).

[109] J. R. Widom, N. P. Johnson, P. H. v. Hippel, and A. H. Marcus, "Solution conformation of 2-aminopurine dinucleotide determined by ultraviolet two-dimensional fluorescence spectroscopy", New J. Phys. **15**, 025028 (2013).

[110] D. Brinks, F. D. Stefani, F. Kulzer, R. Hildner, T. H. Taminiau, Y. Avlasevich, K. Mullen, and N. F. van Hulst, "Visualizing and controlling vibrational wave packets of single molecules", Nature **465**, 905–908 (2010).

[111] D. Brinks, R. Hildner, E. M. H. P. v. Dijk, F. D. Stefani, J. B. Nieder, J. Hernando, and N. F. v. Hulst, "Ultrafast dynamics of single molecules", Chem. Soc. Rev. **43**, 2476–2491 (2014).

[112] A. M. Weiner, "Ultrafast optical pulse shaping: A tutorial review", Opt. Commun. **284**, 3669–3692 (2011).

[113] G. Nardin, T. M. Autry, G. Moody, R. Singh, H. Li, and S. T. Cundiff, "Multi-dimensional coherent optical spectroscopy of semiconductor nanostructures: Collinear and non-collinear approaches", J. Appl. Phys. **117**, 112804 (2015).

[114] M. Plewicki, F. Weise, S. M. Weber, and A. Lindinger, "Phase, amplitude, and polarization shaping with a pulse shaper in a Mach-Zehnder interferometer", Appl. Opt. **45**, 8354–8359 (2006).

[115] M. Ninck, A. Galler, T. Feurer, and T. Brixner, "Programmable common-path vector field synthesizer for femtosecond pulses", Opt. Lett. **32**, 3379–3381 (2007).

[116] O. Masihzadeh, P. Schlup, and R. A. Bartels, "Complete polarization state control of ultrafast laser pulses with a single linear spatial light modulator", Opt. Express **15**, 18025–18032 (2007).

[117] D. Kupka, P. Schlup, and R. A. Bartels, "Simplified ultrafast pulse shaper for tailored polarization states using a birefringent prism", Rev. Sci. Instrum. **80**, 053110 (2009).

[118] M. Sato, T. Suzuki, and K. Misawa, "Interferometric polarization pulse shaper stabilized by an external laser diode for arbitrary vector field shaping", Rev. Sci. Instrum. **80**, 123107 (2009).

[119] C. Schwarz, O. Hüter, and T. Brixner, "Full vector-field control of ultrashort laser pulses utilizing a single dual-layer spatial light modulator in a common-path setup", J. Opt. Soc. Am. B **32**, 933–945 (2015).

[120] S. Yan and H.-S. Tan, "Phase cycling schemes for two-dimensional optical spectroscopy with a pump–probe beam geometry", Chem. Phys. **360**, 110–115 (2009).

[121] Z. Zhang, K. L. Wells, E. W. J. Hyland, and H.-S. Tan, "Phase-cycling schemes for pump–probe beam geometry two-dimensional electronic spectroscopy", Chem. Phys. Lett. **550**, 156–161 (2012).

[122] F. Verluise, V. Laude, Z. Cheng, C. Spielmann, and P. Tournois, "Amplitude and phase control of ultrashort pulses by use of an acousto-optic programmable dispersive filter: Pulse compression and shaping", Opt. Lett. **25**, 575–577 (2000).

[123] E. Riedle, M. Beutter, S. Lochbrunner, J. Piel, S. Schenkl, S. Sporlein, and W. Zinth, "Generation of 10 to 50 fs pulses tunable through all of the visible and the NIR", Appl. Phys. B **71**, 457–465 (2000).

[124] G. Cerullo and S. De Silvestri, "Ultrafast optical parametric amplifiers", Rev. Sci. Instrum. **74**, 1–18 (2003).

[125] L. Conversion, "Topas Series Traveling-wave Optical Parametric Amplifiers, User's Manual", (2009).

[126] A. M. Weiner, "Femtosecond optical pulse shaping and processing", Prog. Quantum Electron. **19**, 161–237 (1995).

[127] A. M. Weiner, "Femtosecond pulse shaping using spatial light modulators", Rev. Sci. Instrum. **71**, 1929–1960 (2000).

[128] D. Goswami, "Optical pulse shaping approaches to coherent control", Phys. Rep. **374**, 385–481 (2003).

[129] A. Monmayrant, S. Weber, and B. Chatel, "A newcomer's guide to ultrashort pulse shaping and characterization", J. Phys. B: At. Mol. Opt. Phys. **43**, 103001 (2010).

[130] A. Galler and T. Feurer, "Pulse shaper assisted short laser pulse characterization", Appl. Phys. B **90**, 427–430 (2008).

[131] D. J. Tannor and S. A. Rice, "Control of selectivity of chemical reaction via control of wave packet evolution", J. Chem. Phys. **83**, 5013–5018 (1985).

[132] H. Rabitz, R. de Vivie-Riedle, M. Motzkus, and K. Kompa, "Whither the future of controlling quantum phenomena?" Science **288**, 824–828 (2000).

[133] T. Brixner and G. Gerber, "Quantum control of gas-phase and liquid-phase femtochemistry", ChemPhysChem **4**, 418–438 (2003).

[134] M. Wollenhaupt and T. Baumert, "Ultrafast laser control of electron dynamics in atoms, molecules and solids", Faraday Discuss. **153**, 9–26 (2011).

[135] M. Shapiro and P. Brumer, *Quantum control of molecular processes* (John Wiley & Sons, 2012), 1st ed.

[136] F. Verluise, V. Laude, J.-P. Huignard, P. Tournois, and A. Migus, "Arbitrary dispersion control of ultrashort optical pulses with acoustic waves", J. Opt. Soc. Am. B **17**, 138–145 (2000).

[137] P. Tournois, "Acousto-optic programmable dispersive filter for adaptive compensation of group delay time dispersion in laser systems", Opt. Commun. **140**, 245–249 (1997).

[138] N. Krebs, R. A. Probst, and E. Riedle, "Sub-20 fs pulses shaped directly in the UV by an acousto-optic programmable dispersive filter", Opt. Express **18**, 6164–6171 (2010).

[139] D. J. McCabe, D. R. Austin, A. Tajalli, S. Weber, I. A. Walmsley, and B. Chatel, "Space-time coupling of shaped ultrafast ultraviolet pulses from an acousto-optic programmable dispersive filter", J. Opt. Soc. Am. B **28**, 58–64 (2011).

[140] Fastlite, "Dazzler System Operating Manual", Tech. rep., Fastlite (2005).

[141] O. Schubert, M. Eisele, V. Crozatier, N. Forget, D. Kaplan, and R. Huber, "Rapid-scan acousto-optical delay line with 34 kHz scan rate and 15 as precision", Opt. Lett. **38**, 2907–2910 (2013).

[142] B. Urbanek, M. Möller, M. Eisele, S. Baierl, D. Kaplan, C. Lange, and R. Huber, "Femtosecond terahertz time-domain spectroscopy at 36 kHz scan rate using an acousto-optic delay", Appl. Phys. Lett. **108**, 121101 (2016).

[143] X. Audier, N. Balla, and H. Rigneault, "Pump-probe micro-spectroscopy by means of an ultra-fast acousto-optics delay line", Opt. Lett., **42**, 294–297 (2017).

[144] P. Tyagi, J. I. Saari, B. Walsh, A. Kabir, V. Crozatier, N. Forget, and P. Kambhampati, "Two-color two-dimensional electronic spectroscopy using dual acousto-optic pulse shapers for complete amplitude, phase, and polarization control of femtosecond laser pulses", J. Phys. Chem. A **117**, 6264–6269 (2013).

[145] H. Seiler, B. Walsh, S. Palato, A. Thai, V. Crozatier, N. Forget, and P. Kambhampati, "Kilohertz generation of high contrast polarization states for visible femtosecond pulses via phase-locked acousto-optic pulse shapers", J. Appl. Phys. **118**, 103110 (2015).

[146] S. Akturk, X. Gu, M. Kimmel, and R. Trebino, "Extremely simple single-prism ultrashort- pulse compressor", Opt. Express **14**, 10101–10108 (2006).

[147] B. Schmidt, M. Hacker, G. Stobrawa, and T. Feurer, "LAB2-A virtual femtosecond laser lab", Tech. rep.

[148] National Instruments, "LabView 2014 Development System", (2014).

[149] M. Nisoli, S. De Silvestri, and O. Svelto, "Generation of high energy 10 fs pulses by a new pulse compression technique", Appl. Phys. Lett. **68**, 2793 (1996).

[150] M. Nisoli, S. De Silvestri, O. Svelto, R. Szipöcs, K. Ferencz, C. Spielmann, S. Sartania, and F. Krausz, "Compression of high-energy laser pulses below 5 fs", Opt. Lett. **22**, 522 (1997).

[151] X. Ma, J. Dostál, and T. Brixner, "Broadband 7-fs diffractive-optic-based 2D electronic spectroscopy using hollow-core fiber compression", Opt. Express **24**, 20781–20791 (2016).

[152] H. Seiler, S. Palato, B. E. Schmidt, and P. Kambhampati, "Simple fiber-based solution for coherent multidimensional spectroscopy in the visible regime", Opt. Lett. **42**, 643–646 (2017).

[153] I. P. Mercer, T. Witting, T. Driver, R. J. Cogdell, J. P. Marangos, and J. W. G. Tisch, "Angle-resolved coherent wave mixing using a 4 fs ultra-broad bandwidth laser", Opt. Lett. **42**, 859–862 (2017).

[154] M. Son, S. Mosquera-Vázquez, and G. S. Schlau-Cohen, "Ultrabroadband 2D electronic spectroscopy with high-speed, shot-to-shot detection", Opt. Express **25**, 18950–18962 (2017).

[155] E. A. Gibson, D. M. Gaudiosi, H. C. Kapteyn, R. Jimenez, S. Kane, R. Huff, C. Durfee, and J. Squier, "Efficient reflection grisms for pulse compression and dispersion compensation of femtosecond pulses", Opt. Lett. **31**, 3363–3365 (2006).

[156] L. Kuznetsova, F. Wise, S. Kane, and J. Squier, "Chirped-pulse amplification near the gain-narrowing limit of Yb-doped fiber using a reflection grism compressor", Appl. Phys. B **88**, 515–518 (2007).

[157] N. Forget, V. Crozatier, and P. Tournois, "Transmission Bragg-grating grisms for pulse compression", Appl. Phys. B **109**, 121–125 (2012).

[158] R. Trebino and D. J. Kane, "Using phase retrieval to measure the intensity and phase of ultrashort pulses: Frequency-resolved optical gating", J. Opt. Soc. Am. A **10**, 1101–1111 (1993).

[159] R. Trebino, *Frequency-resolved optical gating: The measurement of ultrashort laser pulses* (Springer, New York, 2002).

[160] F. Träger, *Springer handbook of lasers and optics*, Springer handbooks (Springer, New York, NY, 2007).

[161] I. Amat-Roldán, I. Cormack, P. Loza-Alvarez, E. Gualda, and D. Artigas, "Ultrashort pulse characterisation with SHG collinear-FROG", Opt. Express **12**, 1169–1178 (2004).

[162] G. Stibenz and G. Steinmeyer, "Interferometric frequency-resolved optical gating", Opt. Express **13**, 2617–2626 (2005).

[163] D. E. Wilcox, F. D. Fuller, and J. P. Ogilvie, "Fast second-harmonic generation frequency-resolved optical gating using only a pulse shaper", Opt. Lett. **38**, 2980 (2013).

[164] K. W. DeLong and R. Trebino, "Improved ultrashort pulse-retrieval algorithm for frequency-resolved optical gating", J. Opt. Soc. Am. A **11**, 2429–2437 (1994).

[165] K. W. DeLong, D. N. Fittinghoff, R. Trebino, B. Kohler, and K. Wilson, "Pulse retrieval in frequency-resolved optical gating based on the method of generalized projections", Opt. Lett. **19**, 2152–2154 (1994).

[166] C. E. Shannon, "Communication in the presence of noise", Proc. IEEE **37**, 10–21 (1949).

[167] A. W. Albrecht, J. D. Hybl, S. M. G. Faeder, and D. M. Jonas, "Experimental distinction between phase shifts and time delays: Implications for femtosecond spectroscopy and coherent control of chemical reactions", J. Chem. Phys. **111**, 10934–10956 (1999).

[168] D. Polli, L. Lüer, and G. Cerullo, "High-time-resolution pump-probe system with broadband detection for the study of time-domain vibrational dynamics", Rev. Sci. Instrum. **78**, 103108 (2007).

[169] F. Kanal, S. Keiber, R. Eck, and T. Brixner, "100-kHz shot-to-shot broadband data acquisition for high-repetition-rate pump–probe spectroscopy", Opt. Express **22**, 16965–16975 (2014).

[170] N. M. Kearns, R. D. Mehlenbacher, A. C. Jones, and M. T. Zanni, "Broadband 2D electronic spectrometer using white light and pulse shaping: noise and signal evaluation at 1 and 100 kHz", Opt. Express **25**, 7869–7883 (2017).

[171] B. Mamyrin, V. Karataev, D. Shmikk, and V. Zagulin, "The mass-reflectron, a new nonmagnetic time-of-flight mass spectrometer with high resolution", Zh. Eksp. Teor. Fiz. **64**, 82–89 (1973).

[172] W. C. Wiley and I. H. McLaren, "Time-of-flight mass spectrometer with improved resolution", Rev. Sci. Instrum. **26**, 1150–1157 (1955).

[173] U. Boesl, R. Weinkauf, and E. Schlag, "Reflectron time-of-flight mass spectrometry and laser excitation for the analysis of neutrals, ionized molecules and secondary fragments", Int. J. Mass Spectrom. **112**, 121–166 (1992).

[174] S. Roeding, "Ultrafast photofragment ion spectroscopy of 5-diazo Meldrum's acid", Master Thesis, Würzburg (2013).

[175] B. Kiefer, "Femtochemie: Beobachtung und Steuerung molekularer Dynamik", Dissertation, Würzburg, Fakultät für Physik und Astronomie (2000).

[176] J. L. Wiza, "Microchannel plate detectors", Nucl. Instrum. Methods **162**, 587–601 (1979).

[177] E. Harel, A. F. Fidler, and G. S. Engel, "Real-time mapping of electronic structure with single-shot two-dimensional electronic spectroscopy", PNAS **107**, 16444–16447 (2010).

[178] E. Harel, A. F. Fidler, and G. S. Engel, "Single-shot gradient-assisted photon echo electronic spectroscopy", J. Phys. Chem. A **115**, 3787–3796 (2011).

[179] B. Spokoyny, C. J. Koh, and E. Harel, "Stable and high-power few cycle supercontinuum for 2D ultrabroadband electronic spectroscopy", Opt. Lett. **40**, 1014–1017 (2015).

[180] M. K. Yetzbacher, N. Belabas, K. A. Kitney, and D. M. Jonas, "Propagation, beam geometry, and detection distortions of peak shapes in two-dimensional Fourier transform spectra", J. Chem. Phys. **126**, 044511 (2007).

[181] B. Cho, M. K. Yetzbacher, K. A. Kitney, E. R. Smith, and D. M. Jonas, "Propagation and beam geometry effects on two-dimensional Fourier transform spectra of multilevel systems", J. Phys. Chem. A **113**, 13287–13299 (2009).

[182] H. Li, A. P. Spencer, A. Kortyna, G. Moody, D. M. Jonas, and S. T. Cundiff, "Pulse propagation effects in optical 2D Fourier-transform spectroscopy: Experiment", J. Phys. Chem. A **117**, 6279–6287 (2013).

[183] A. P. Spencer, H. Li, S. T. Cundiff, and D. M. Jonas, "Pulse propagation effects in optical 2D Fourier-transform spectroscopy: Theory", J. Phys. Chem. A **119**, 3936–3960 (2015).

[184] I. A. Heisler, R. Moca, F. V. A. Camargo, and S. R. Meech, "Two-dimensional electronic spectroscopy based on conventional optics and fast dual chopper data acquisition", Rev. Sci. Instrum. **85**, 063103 (2014).

[185] W. Wagner, C. Li, J. Semmlow, and W. Warren, "Rapid phase-cycled two-dimensional optical spectroscopy in fluorescence and transmission mode", Opt. Express **13**, 3697–3706 (2005).

[186] L. A. Bizimana, J. Brazard, W. P. Carbery, T. Gellen, and D. B. Turner, "Resolving molecular vibronic structure using high-sensitivity two-dimensional electronic spectroscopy", J. Chem. Phys. **143**, 164203 (2015).

[187] D. B. Turner, K. E. Wilk, P. M. G. Curmi, and G. D. Scholes, "Comparison of electronic and vibrational coherence measured by two-dimensional electronic spectroscopy", J. Phys. Chem. Lett. **2**, 1904–1911 (2011).

[188] T. Fuji, T. Saito, and T. Kobayashi, "Dynamical observation of Duschinsky rotation by sub-5-fs real-time spectroscopy", Chem. Phys. Lett. **332**, 324–330 (2000).

[189] E. Vogel, A. Gbureck, and W. Kiefer, "Vibrational spectroscopic studies on the dyes cresyl violet and coumarin 152", J. Mol. Struct. **550–551**, 177–190 (2000).

[190] P. Hamm, "Three-dimensional-IR spectroscopy: Beyond the two-point frequency fluctuation correlation function", J. Chem. Phys. **124**, 124506 (2006).

[191] S. Garrett-Roe and P. Hamm, "Purely absorptive three-dimensional infrared spectroscopy", J. Chem. Phys. **130**, 164510 (2009).

[192] A. F. Fidler, E. Harel, and G. S. Engel, "Dissecting hidden couplings using fifth-order three-dimensional electronic spectroscopy", J. Phys. Chem. Lett. **1**, 2876–2880 (2010).

[193] Z. Zhang, K. L. Wells, and H.-S. Tan, "Purely absorptive fifth-order three-dimensional electronic spectroscopy", Opt. Lett. **37**, 5058–5060 (2012).

[194] Z. Zhang, K. L. Wells, M. T. Seidel, and H.-S. Tan, "Fifth-order three-dimensional electronic spectroscopy using a pump–probe configuration", J. Phys. Chem. B **117**, 15369–15385 (2013).

[195] H. Li, A. D. Bristow, M. E. Siemens, G. Moody, and S. T. Cundiff, "Unraveling quantum pathways using optical 3D Fourier-transform spectroscopy", Nat. Commun. **4**, 1390 (2013).

[196] D. B. Turner, K. W. Stone, K. Gundogdu, and K. A. Nelson, "Three-dimensional electronic spectroscopy of excitons in GaAs quantum wells", J. Chem. Phys. **131**, 144510 (2009).

[197] D. Hayes and G. S. Engel, "Extracting the excitonic Hamiltonian of the Fenna-Matthews-Olson complex using three-dimensional third-order electronic spectroscopy", Biophys. J. **100**, 2043–2052 (2011).

[198] V. Butkus, D. Zigmantas, L. Valkunas, and D. Abramavicius, "Vibrational vs. electronic coherences in 2D spectrum of molecular systems", Chem. Phys. Lett. **545**, 40–43 (2012).

[199] S. S. Senlik, V. R. Policht, and J. P. Ogilvie, "Two-color nonlinear spectroscopy for the rapid acquisition of coherent dynamics", J. Phys. Chem. Lett. **6**, 2413–2420 (2015).

[200] J. R. Taylor, *An introduction to error analysis* (Univ. Science Books, Sausalito, Calif., 1997).

[201] M. Kasha, "Characterization of electronic transitions in complex molecules", Discuss. Faraday Soc. **9**, 14 (1950).

[202] S. Mukamel, R. Oszwałdowski, and L. Yang, "A coherent nonlinear optical signal induced by electron correlations", J. Chem. Phys. **127**, 221105 (2007).

[203] J. Kim, V. M. Huxter, C. Curutchet, and G. D. Scholes, "Measurement of electron-electron interactions and correlations using two-dimensional electronic double-quantum coherence spectroscopy", J. Phys. Chem. A **113**, 12122–12133 (2009).

[204] S. Mukamel, D. Abramavicius, L. Yang, W. Zhuang, I. V. Schweigert, and D. V. Voronine, "Coherent multidimensional optical probes for electron correlations and exciton dynamics: From NMR to X-rays", Acc. Chem. Res. **42**, 553–562 (2009).

[205] A. Nemeth, F. Milota, T. Mančal, T. Pullerits, J. Sperling, J. Hauer, H. F. Kauffmann, and N. Christensson, "Double-quantum two-dimensional electronic spectroscopy of a three-level system: Experiments and simulations", J. Chem. Phys. **133**, 094505 (2010).

[206] K. W. Stone, D. B. Turner, K. Gundogdu, S. T. Cundiff, and K. A. Nelson, "Exciton-exciton correlations revealed by two-quantum, two-dimensional Fourier transform optical spectroscopy", Acc. Chem. Res. **42**, 1452–1461 (2009).

[207] N. Christensson, F. Milota, A. Nemeth, I. Pugliesi, E. Riedle, J. Sperling, T. Pullerits, H. F. Kauffmann, and J. Hauer, "Electronic double-quantum coherences and their impact on ultrafast spectroscopy: The example of β-Carotene", J. Phys. Chem. Lett. **1**, 3366–3370 (2010).

[208] M. Billeter and V. Orekhov, *Data sampling in multidimensional NMR*, no. 316 in Topics in Current Chemistry (Springer Berlin Heidelberg, 2011).

[209] M. Mobli and J. C. Hoch, "Nonuniform sampling and non-Fourier signal processing methods in multidimensional NMR", Prog. Nucl. Magn. Reson. Spectrosc. **83**, 21–41 (2014).

[210] E. Candès, J. Romberg, and T. Tao, "Robust uncertainty principles: exact signal reconstruction from highly incomplete frequency information", IEEE Trans. Inf. Theory **52**, 489–509 (2006).

[211] D. Donoho, "Compressed sensing", IEEE Trans. Inf. Theory **52**, 1289–1306 (2006).

[212] M. F. Duarte, M. A. Davenport, D. Takbar, J. N. Laska, T. Sun, K. F. Kelly, and R. G. Baraniuk, "Single-pixel imaging via compressive sampling", IEEE Signal Process Mag. **25**, 83–91 (2008).

[213] A. P. Spencer, B. Spokoyny, S. Ray, F. Sarvari, and E. Harel, "Mapping multidimensional electronic structure and ultrafast dynamics with single-element detection and compressive sensing", Nat. Commun. **7**, 10434 (2016).

[214] L. Gao, J. Liang, C. Li, and L. V. Wang, "Single-shot compressed ultrafast photography at one hundred billion frames per second", Nature **516**, 74–77 (2014).

[215] J. Liang, C. Ma, L. Zhu, Y. Chen, L. Gao, and L. V. Wang, "Single-shot real-time video recording of a photonic Mach cone induced by a scattered light pulse", Sci. Adv. **3**, e1601814 (2017).

[216] M. Lustig, D. Donoho, and J. M. Pauly, "Sparse MRI: The application of compressed sensing for rapid MR imaging", Magn. Reson. Med. **58**, 1182–1195 (2007).

[217] D. J. Holland, M. J. Bostock, L. F. Gladden, and D. Nietlispach, "Fast multidimensional NMR spectroscopy using compressed sensing", Angew. Chem. **123**, 6678–6681 (2011).

[218] Y. Shrot and L. Frydman, "Compressed sensing and the reconstruction of ultrafast 2D NMR data: Principles and biomolecular applications", J. Magn. Reson. **209**, 352–358 (2011). 00025.

[219] D. J. Holland and L. F. Gladden, "Less is more: how compressed sensing is transforming metrology in chemistry", Angew. Chem. Int. Ed. **53**, 13330–13340 (2014).

[220] J. N. Sanders, S. K. Saikin, S. Mostame, X. Andrade, J. R. Widom, A. H. Marcus, and A. Aspuru-Guzik, "Compressed sensing for multidimensional spectroscopy experiments", J. Phys. Chem. Lett. **3**, 2697–2702 (2012).

[221] J. Almeida, J. Prior, and M. B. Plenio, "Computation of two-dimensional spectra assisted by compressed sampling", J. Phys. Chem. Lett. **3**, 2692–2696 (2012).

[222] J. A. Dunbar, D. G. Osborne, J. M. Anna, and K. J. Kubarych, "Accelerated 2D-IR using compressed sensing", J. Phys. Chem. Lett. **4**, 2489–2492 (2013).

[223] S. G. Hyberts, K. Takeuchi, and G. Wagner, "Poisson-gap sampling and forward maximum entropy reconstruction for enhancing the resolution and sensitivity of protein NMR data", J. Am. Chem. Soc. **132**, 2145–2147 (2010).

[224] M. Mobli, M. W. Maciejewski, A. D. Schuyler, A. S. Stern, and J. C. Hoch, "Sparse sampling methods in multidimensional NMR", Phys. Chem. Chem. Phys. **14**, 10835 (2012).

[225] S. G. Hyberts, H. Arthanari, S. A. Robson, and G. Wagner, "Perspectives in magnetic resonance: NMR in the post-FFT era", J. Magn. Reson. **241**, 60–73 (2014).

[226] E. Candès and M. Wakin, "An introduction to compressive sampling", IEEE Signal Process Mag. **25**, 21–30 (2008).

[227] E. D. Nelson and M. L. Fredman, "Hadamard spectroscopy", J. Opt. Soc. Am., JOSA **60**, 1664–1669 (1970).

[228] D. K. Graff, "Fourier and Hadamard: Transforms in spectroscopy", J. Chem. Educ. **72**, 304 (1995).

[229] S. A. Dyer, "Hadamard transform spectrometry", Chemom. Intell. Lab. Syst. **12**, 101–115 (1991).

[230] D. Gabor, "Theory of communication", J. IEEE **93**, 429–457 (1946).

[231] D. J. Tannor, N. Takemoto, and A. Shimshovitz, "Phase space approach to solving the Schrödinger equation: thinking inside the box", in "Advances in Chemical Physics," , S. A. Rice and A. R. Dinner, eds. (John Wiley & Sons, Inc., 2014), pp. 1–34.

[232] S. Foucart and H. Rauhut, *A mathematical introduction to compressive sensing* (Springer New York, 2013).

[233] *MATLAB Release 8.5.0. (R2015a)* (The MathWorks Inc., Natick, Mass., 2015).

[234] J. Bioucas-Dias and M. Figueiredo, "A new TwIST: two-step iterative shrinkage/thresholding algorithms for image restoration", IEEE Trans. Image Process. **16**, 2992–3004 (2007).

[235] J. Romberg, "Imaging via compressive sampling", IEEE Signal Process Mag. **25**, 14–20 (2008).

[236] J. v. Neumann, "Die Eindeutigkeit der Schrödingerschen Operatoren", Math. Ann. **104**, 570–578 (1931).

[237] M. J. Davis and E. J. Heller, "Semiclassical Gaussian basis set method for molecular vibrational wave functions", J. Chem. Phys. **71**, 3383–3395 (1979).

[238] A. Shimshovitz, Z. Bačić, and D. J. Tannor, "The von Neumann basis in non-Cartesian coordinates: Application to floppy triatomic molecules", J. Chem. Phys. **141**, 234106 (2014).

[239] A. Shimshovitz and D. J. Tannor, "Phase-space approach to solving the time-independent Schrödinger equation", Phys. Rev. Lett. **109**, 070402 (2012).

[240] N. Takemoto, A. Shimshovitz, and D. J. Tannor, "Communication: Phase space approach to laser-driven electronic wavepacket propagation", J. Chem. Phys. **137**, 011102 (2012).

[241] T. Halverson and B. Poirier, "Calculation of exact vibrational spectra for P_2O and CH_2NH using a phase space wavelet basis", J. Chem. Phys. **140**, 204112 (2014).

[242] J. Brown and T. Carrington Jr., "Using an iterative eigensolver to compute vibrational energies with phase-spaced localized basis functions", J. Chem. Phys. **143**, 044104 (2015).

[243] S. Machnes, E. Assémat, H. R. Larsson, and D. J. Tannor, "Quantum dynamics in phase space using projected von Neumann bases", J. Phys. Chem. A **120**, 3296–3308 (2016).

[244] S. Fechner, F. Dimler, T. Brixner, G. Gerber, and D. J. Tannor, "The von Neumann picture: A new representation for ultrashort laser pulses", Opt. Express **15**, 15387–15401 (2007).

[245] A. Rodenberg, S. Fechner, F. Dimler, D. J. Tannor, and T. Brixner, "Experimental implementation of ultrashort laser pulses in the von Neumann picture", Appl. Phys. B **93**, 763–772 (2008).

[246] F. Dimler, S. Fechner, A. Rodenberg, T. Brixner, and D. J. Tannor, "Accurate and efficient implementation of the von Neumann representation for laser pulses with discrete and finite spectra", New J. Phys. **11**, 105052 (2009).

[247] S. Rützel, A. Krischke, and T. Brixner, "The von Neumann representation as a joint time–frequency parameterization for polarization-shaped femtosecond laser pulses", Appl. Phys. B **107**, 1–9 (2012).

[248] S. Ruetzel, C. Stolzenberger, S. Fechner, F. Dimler, T. Brixner, and D. J. Tannor, "Molecular quantum control landscapes in von Neumann time-frequency phase space", J. Chem. Phys. **133**, 164510 (2010).

[249] S. Ruetzel, C. Stolzenberger, F. Dimler, D. J. Tannor, and T. Brixner, "Adaptive coherent control using the von Neumann basis", Phys. Chem. Chem. Phys. **13**, 8627–8636 (2011).

[250] A. Shimshovitz and D. J. Tannor, "Periodic Gabor functions with biorthogonal exchange: A highly accurate and efficient method for signal compression", arXiv:1207.0632 [math] (2012). ArXiv: 1207.0632.

[251] S. Ruetzel, "Pulse-sequence approaches for multidimensional electronic spectroscopy of ultrafast photochemistry", Dissertation, Würzburg (2014).

[252] X. Dai, A. D. Bristow, D. Karaiskaj, and S. T. Cundiff, "Two-dimensional Fourier-transform spectroscopy of potassium vapor", Phys. Rev. A **82**, 052503 (2010).

[253] J. Lu, X. Li, H. Y. Hwang, B. K. Ofori-Okai, T. Kurihara, T. Suemoto, and K. A. Nelson, "Coherent two-dimensional terahertz magnetic resonance spectroscopy of collective spin waves", Phys. Rev. Lett. **118**, 207204 (2017).

[254] M. Dantus, M. J. Rosker, and A. H. Zewail, "Real-time femtosecond probing of ''transition states'' in chemical reactions", J. Chem. Phys. **87**, 2395–2397 (1987).

[255] C. E. Crespo-Hernández, B. Cohen, P. M. Hare, and B. Kohler, "Ultrafast excited-state dynamics in nucleic acids", Chem. Rev. **104**, 1977–2020 (2004).

[256] M. Kotur, T. Weinacht, C. Zhou, and S. Matsika, "Following ultrafast radiationless relaxation dynamics with strong field dissociative ionization: A comparison between Adenine, Uracil, and Cytosine", IEEE J. Sel. Top. Quantum Electron. **18**, 187 –194 (2012).

[257] V. G. Stavros and J. R. R. Verlet, "Gas-phase femtosecond particle spectroscopy: A bottom-up approach to nucleotide dynamics", Annu. Rev. Phys. Chem. **67**, 211–232 (2016).

[258] J. P. Toennies and A. F. Vilesov, "Superfluid helium droplets: A uniquely cold nanomatrix for molecules and molecular complexes", Angew. Chem. Int. Ed. **43**, 2622–2648 (2004).

[259] F. Stienkemeier and K. K. Lehmann, "Spectroscopy and dynamics in helium nanodroplets", J. Phys. B: At. Mol. Opt. Phys. **39**, R127 (2006).

[260] L. Bruder, M. Mudrich, and F. Stienkemeier, "Phase-modulated electronic wave packet interferometry reveals high resolution spectra of free Rb atoms and Rb*He molecules", Phys. Chem. Chem. Phys. **17**, 23877–23885 (2015).

[261] L. Bruder, M. Binz, and F. Stienkemeier, "Efficient isolation of multiphoton processes and detection of collective resonances in dilute samples", Phys. Rev. A **92**, 053412 (2015).

[262] I. V. Hertel and W. Radloff, "Ultrafast dynamics in isolated molecules and molecular clusters", Rep. Prog. Phys. **69**, 1897 (2006).

[263] C. Lux, M. Wollenhaupt, T. Bolze, Q. Liang, J. Köhler, C. Sarpe, and T. Baumert, "Circular dichroism in the photoelectron angular distributions of Camphor and Fenchone from multiphoton ionization with femtosecond laser pulses", Angew. Chem. Int. Ed. **51**, 5001–5005 (2012).

[264] M. H. M. Janssen and I. Powis, "Detecting chirality in molecules by imaging photoelectron circular dichroism", Phys. Chem. Chem. Phys. **16**, 856–871 (2014).

[265] R. C. Cohen and J. G. Murphy, "Photochemistry of NO_2 in Earth's stratosphere: Constraints from observations", Chem. Rev. **103**, 4985–4998 (2003).

[266] I. Wilkinson and B. J. Whitaker, "Some remarks on the photodynamics of NO_2", Annu. Rep. Prog. Chem., Sect. C: Phys. Chem. **106**, 274–304 (2010).

[267] K. S. Haber, J. W. Zwanziger, F. X. Campos, R. T. Wiedmann, and E. R. Grant, "Direct determination of the adiabatic ionization potential of NO_2 by multiresonant optical absorption", Chem. Phys. Lett. **144**, 58–64 (1988).

[268] W. Schneider, G. K. Moortgat, G. S. Tyndall, and J. P. Burrows, "Absorption cross-sections of NO_2 in the UV and visible region (200 – 700 nm) at 298 K", J. Photochem. Photobiol., A **40**, 195–217 (1987).

[269] H. Keller-Rudek, G. K. Moortgat, R. Sander, and R. Sörensen, "The MPI-Mainz UV/VIS spectral atlas of gaseous molecules of atmospheric interest", Earth Syst. Sci. Data **5**, 365–373 (2013).

[270] A. T. J. B. Eppink, B. J. Whitaker, E. Gloaguen, B. Soep, A. M. Coroiu, and D. H. Parker, "Dissociative multiphoton ionization of NO_2 studied by time-resolved imaging", J. Chem. Phys. **121**, 7776–7783 (2004).

[271] N. T. Form, B. J. Whitaker, L. Poisson, and B. Soep, "Time-resolved photoion and photoelectron imaging of NO_2", Phys. Chem. Chem. Phys. **8**, 2925–2932 (2006).

[272] D. Irimia, I. D. Petsalakis, G. Theodorakopoulos, and M. H. M. Janssen, "Coherent oscillatory femtosecond dynamics in multichannel photodynamics of NO_2 studied by spatially masked electron imaging", J. Phys. Chem. A **114**, 3157–3166 (2010).

[273] R. Cireasa, J.-B. Hamard, C. Maury, and V. Blanchet, "Imaging fast relaxation dynamics of NO_2", Phys. Scr. **80**, 048106 (2009).

[274] J. B. Hamard, R. Cireasa, B. Chatel, V. Blanchet, and B. J. Whitaker, "Quantum interference in NO_2", J. Phys. Chem. A **114**, 3167–3175 (2010).

[275] Y. Arasaki, K. Takatsuka, K. Wang, and V. McKoy, "Time-resolved photoelectron spectroscopy of wavepackets through a conical intersection in NO_2", J. Chem. Phys. **132**, 124307 (2010).

[276] H. J. Wörner, J. B. Bertrand, B. Fabre, J. Higuet, H. Ruf, A. Dubrouil, S. Patchkovskii, M. Spanner, Y. Mairesse, V. Blanchet, E. Mével, E. Constant, P. B. Corkum, and D. M. Villeneuve, "Conical intersection dynamics in NO_2 probed by homodyne high-harmonic spectroscopy", Science **334**, 208–212 (2011).

[277] H. Ruf, C. Handschin, A. Ferré, N. Thiré, J. B. Bertrand, L. Bonnet, R. Cireasa, E. Constant, P. B. Corkum, D. Descamps, B. Fabre, P. Larregaray, E. Mével, S. Petit, B. Pons, D. Staedter, H. J. Wörner, D. M. Villeneuve, Y. Mairesse, P. Halvick, and V. Blanchet, "High-harmonic transient grating spectroscopy of NO_2 electronic relaxation", J. Chem. Phys. **137**, 224303 (2012).

[278] C. Elkharrat, Y. J. Picard, P. Billaud, C. Cornaggia, D. Garzella, M. Perdrix, J. C. Houver, R. R. Lucchese, and D. Dowek, "Ion pair formation in multiphoton excitation of NO_2 using linearly and circularly polarized femtosecond light pulses: kinetic energy distribution and fragment recoil anisotropy." J. Phys. Chem. A **114**, 9902–9918 (2010).

[279] S. M. Poullain, K. Veyrinas, P. Billaud, M. Lebech, Y. J. Picard, R. R. Lucchese, and D. Dowek, "The role of Rydberg states in photoionization of NO_2 and (NO^+, O^-) ion pair formation induced by one VUV photon", J. Chem. Phys. **139**, 044311 (2013).

[280] S. M. Poullain, C. Elkharrat, W. B. Li, K. Veyrinas, J. C. Houver, C. Cornaggia, T. N. Rescigno, R. R. Lucchese, and D Dowek, "Recoil frame photoemission in multiphoton ionization of small polyatomic molecules: photodynamics of NO_2 probed by 400 nm fs pulses", J. Phys. B: At. Mol. Opt. Phys. **47**, 124024 (2014).

[281] A. H. Zewail and S. Pedersen, "Femtosecond real time probing of reactions XXII: kinetic description of probe absorption, fluorescence depletion and mass spectrometry", Mol. Phys. **89**, 1455–1502 (1996).

[282] I. H. M. van Stokkum, D. S. Larsen, and R. van Grondelle, "Global and target analysis of time-resolved spectra", Biochim. Biophys. Acta, Bioenerg. **1657**, 82–104 (2004).

[283] A. Vredenborg, W. G. Roeterdink, and M. H. M. Janssen, "Femtosecond time-resolved photoelectron-photoion coincidence imaging of multiphoton multichannel photodynamics in NO_2", J. Chem. Phys. **128**, 204311 (2008).

[284] J. A. Davies, J. E. LeClaire, R. E. Continetti, and C. C. Hayden, "Femtosecond time-resolved photoelectron–photoion coincidence imaging studies of dissociation dynamics", J. Chem. Phys. **111**, 1–4 (1999).

[285] R. B. López-Martens, T. W. Schmidt, and G. Roberts, "Femtosecond fluorescence depletion spectroscopy of NO_2 multiphoton dissociation dynamics", J. Chem. Phys. **111**, 7183–7186 (1999).

[286] F. Santoro and C. Petrongolo, "Nonadiabatic radiative lifetimes and fluorescence spectra of NO_2", J. Chem. Phys. **111**, 9651–9657 (1999).

[287] T. W. Schmidt, R. B. López-Martens, and G. Roberts, "Intense-field modulation of NO_2 multiphoton dissociation dynamics", J. Chem. Phys. **121**, 4133–4142 (2004).

[288] B. Liu, J. Zhu, B. Wang, Y. Wang, and L. Wang, "Time-resolved dynamics of NO_2 in its conical intersection region", J. Phys. Chem. A **113**, 13839–13844 (2009).

[289] R. J. S. Morrison, B. H. Rockney, and E. R. Grant, "Multiphoton ionization of NO_2: Spectroscopy and dynamics", J. Chem. Phys. **75**, 2643–2651 (1981).

[290] J. Bredenbeck, J. Helbing, K. Nienhaus, G. U. Nienhaus, and P. Hamm, "Protein ligand migration mapped by nonequilibrium 2D-IR exchange spectroscopy", PNAS **104**, 14243–14248 (2007).

[291] C. R. Baiz, M. J. Nee, R. McCanne, and K. J. Kubarych, "Ultrafast nonequilibrium Fourier-transform two-dimensional infrared spectroscopy", Opt. Lett. **33**, 2533–2535 (2008).

[292] S. Ruetzel, M. Kullmann, J. Buback, P. Nuernberger, and T. Brixner, "Tracing the steps of photoinduced chemical reactions in organic molecules by coherent two-dimensional electronic spectroscopy using triggered exchange", Phys. Rev. Lett. **110**, 148305 (2013).

[293] U. Fano, "Effects of configuration interaction on intensities and phase shifts", Phys. Rev. **124**, 1866–1878 (1961).

[294] C. Ott, A. Kaldun, P. Raith, K. Meyer, M. Laux, J. Evers, C. H. Keitel, C. H. Greene, and T. Pfeifer, "Lorentz meets Fano in spectral line shapes: A universal phase and its laser control", Science **340**, 716–720 (2013).

[295] D. Finkelstein-Shapiro, F. Poulsen, T. Pullerits, and T. Hansen, "Coherent two-dimensional spectroscopy of a Fano model", Phys. Rev. B **94**, 205137 (2016).

Acknowledgements

Finally, I would like to thank those who contributed to the work presented in this thesis by excellent guidance and teaching, joint teamwork, fruitful discussions, and encouragement inside and outside the laboratory. In particular, I would like to express my deep gratitude to

- **Prof. Dr. Tobias Brixner**, for his enthusiasm and encouragement to pursue ideas and experiments off the beaten track, for steady advice and his confidence in my abilities to realize a major part of the ERC-funded *MULTISCOPE* project, for providing excellent laboratory equipment to actually do this, and for giving me the opportunity to visit many international conferences and summer schools.

- **Prof. Dr. Ingo Fischer** and **Prof. Dr. Jens Pflaum** for their highly appreciated support and valuable input as members of the advisory committee on my path to graduation in the Graduate School of Science and Technology.

- the Graduate School of Science and Technology with the administrative head **Dr. Stephan Schröder-Köhne** for providing an excellent administrative environment with the possibility to attend various training courses that are directly or indirectly related to the actual research work.

- **Prof. Dr. Patrick Nürnberger** and **Dr. Andreas Steinbacher** for their support during the very early stages of the project when the mass spectrometer had to be brought back to life and the specifications of the pulse shaper had to be discussed with Fastlite.

- **Simon Draeger**, who started the fluorescence project with me for his Master's thesis and continued our work as a PhD student, and **Nikita Klimovich**, who came to our institute for a 6-month internship and helped significantly to advance the optimized-sampling project, for their contributions in the aforementioned projects all the way to publication.

- the *IPTC Running Enthusiasts* **Dr. Stefan Rützel**, **Dr. Andreas Steinbacher**, **Dr. Johannes Knorr**, **Dr. Federico Koch** and **Sebastian Götz** for convincing me that running can be fun, and more importantly, for all the other leisure activities and discussions that were even more pleasant when **Dr. Christian Kramer** was present.

- **Dr. Stefan Rützel**, **Dr. Christian Kramer**, **Dr. Jakub Dostál**, and **Sebastian Götz** for carefully proof-reading parts of this thesis.

- our secretaries **Andrea Gehring**, **Anna Rosenfeldt** and **Sandra Stoudek** for taking over all the administrative workload while maintaining a pleasant and warmhearted mindset.

- our technical staff **Belinda Böhm**, **Sabine Fuchs**, and also **Sabine Stahl** for their assistance in various stages of the projects.

- the members of the mechanics workshop (**Wolfgang Liebler**, **Ralf Kohrmann**,**Katharina Schreckling**) and of the electronics workshop (**Reiner Eck**, **Jürgen Zimmermann**) for their contributions to solve technical challenges. I would like to thank especially **Peter Lang** for maintaining an almost daily exchange of nitrogen gas bottles over several weeks in the laboratory.

- **Marko Flock** and **Hubert Gerwe**, who joined me working on the gas-phase project during their Bachelor's thesis, for their endurance and patience when things in the lab did not work as smoothly as expected.

- **Dr. Christoph Schwarz** and **Bernhard Huber** for the administration of our workstations, **Dr. Stefan Rützel** and **Simon Draeger** for managing the snack and coffee supply and **Dr. Philipp Rudolf** as well as **Sebastian Schott** for keeping our literature database in shape.

- all current and past members of our research group who contributed with critical questions, stimulating discussions and good ideas to the success of this work. Science often played the major, but not the only role in this great atmosphere.

- all my friends outside university for giving me the distraction that helped me to approach scientific questions with a clear mind.

- my parents **Emil** and **Ingrid**, and my siblings **Thomas** with his family and **Annika** for providing a place to retreat and to gain courage for new challenges.

- **Verena**, for your support during the difficult periods of this work, for your patience when work-related issues seemed to be dominating, for your smile when the world was upside down and for your invaluable love.

Affidavit

I hereby confirm that my thesis entitled

Coherent Multidimensional Spectroscopy in Molecular Beams and Liquids Using Incoherent Observables

is the result of my own work. I did not receive any help or support from commercial consultants. All sources and / or materials applied are listed and specified in the thesis.

Furthermore, I confirm that this thesis has not yet been submitted as part of another examination process neither in identical nor in similar form.

Würzburg, September 19, 2017

Sebastian Röding

Eidesstattliche Erklärung

Hiermit erkläre ich an Eides statt, die Dissertation mit dem Titel

Kohärente Multidimensionale Spektroskopie in Molekularstrahlen und Flüssigkeiten durch inkohärente Observablen

eigenständig, d.h. insbesondere selbständig und ohne Hilfe eines kommerziellen Promotionsberaters, angefertigt und keine anderen als die von mir angegebenen Quellen und Hilfsmittel verwendet zu haben.

Ich erkläre außerdem, dass die Dissertation weder in gleicher noch in ähnlicher Form bereits in einem anderen Prüfungsverfahren vorgelegen hat.

Würzburg, 19. September 2017

Sebastian Röding